ABSTRACT

UTILITY OF REMOTE SENSING DATA IN RETRIEVAL OF WATER QUALITY CONSTITUENTS CONCENTRATIONS IN COASTAL WATER OF NEW JERSEY

by
Ting Yu

Three important optical properties used for monitoring coastal water quality are the concentrations of chlorophyll (CHL), color dissolved organic matter (CDOM) and total suspended materials (TSM). Ocean color remote sensing, a technique to collect color data by detection of upward radiance from a distance (Bukata et al.,1995), provides a synoptic view for determining these concentrations from upwelling radiances. In the open ocean (Case-I), it is not difficult to derive empirical algorithms relating the received radiances to surface concentrations of water quality parameters. In coastal waters (Case-II), there are serious unresolved problems in extracting chlorophyll concentration because of high concentration of suspended particles (Gordon and Morel, 1983).

There are three basic approaches to estimate optical water quality parameters from remotely sensed spectral data based on the definitions given by Morel & Gordon (1980): (1) an empirical method, in which statistical relationships between the upward radiance at the sea surface and the quantity of interest are taken into account; (2) a semi-empirical method, in which the spectral characteristics of the parameters of interest are known and some modeling of the physics is introduced; and (3) an analytical method, in which radiative transfer models are used to extract the inherent optical properties (IOPs) and a suite of analysis methods can be used to optimally retrieve the water constituents from the remotely sensed upwelling radiance or irradiance reflectance signal.

The focus of this research is the modification and application of analytical and statistical algorithms to characterize the physically based surface spectral reflectance for the waters of the Hudson/Raritan Estuary and to retrieve the water constituent concentrations from the NASA Airborne Visible/Infrared Imaging Spectrometer (AVIRIS) and LIght Detection And Ranging (LIDAR) signals. The approaches used here are based on the unique capabilities of AVIRIS and LIDAR data which can potentially provide a better understanding of how sunlight interacts with estuarine/inland water, especially when complemented with in situ measurements for analysis of water quality parameters and eutrophication processes.

The results of analysis in forms of thematic maps are then input into geographic information system (GIS) of the study site for use by water resource managers and planners for better monitoring and management of water quality condition.

UTILITY OF REMOTE SENSING DATA IN RETRIEVAL OF WATER QUALITY CONSTITUENTS CONCENTRATIONS IN COASTAL WATER OF NEW JERSEY

by
Ting Yu

A Dissertation
Submitted to the Faculty of
New Jersey Institute of Technology
in Partial Fulfillment of the Requirements for the Degree of
Doctor of Philosophy in Civil Engineering

Department of Civil and Environmental Engineering

May 2005

APPROVAL PAGE

UTILITY OF REMOTE SENSING DATA IN RETRIEVAL OF WATER QUALITY CONSTITUENTS CONCENTRATIONS IN COASTAL WATER OF NEW JERSEY

Ting Yu

Dr. Sima Bagheri, Dissertation Advisor — Date
Professor of Civil and Environmental Engineering, NJIT

Dr. Hsin-Neng Hsieh, Committee Member — Date
Professor of Civil and Environmental Engineering, NJIT

Dr. Lisa Axe, Committee Member — Date
Associate Professor of Civil and Environmental Engineering, NJIT

Dr. Taha F. Marhaba, Committee Member — Date
Associate Professor of Civil and Environmental Engineering, NJIT

Dr. Eliza Z. H. Michalopoulou, Committee Member — Date
Associate Professor of Mathematical Sciences and Electrical and Computer Engineering, NJIT

BIOGRAPHICAL SKETCH

Author: Ting Yu

Degree: Doctor of Philosophy

Date: May 2005

Undergraduate and Graduate Education:

- Doctor of Philosophy in Civil Engineering,
  New Jersey Institute of Technology, Newark, NJ, 2005

- Master of Science in Civil Engineering,
  Tsinghua University, Beijing, P. R. China, 2000

- Bachelor of Science in Civil Engineering,
  Tsinghua University, Beijing, P. R. China, 1995

Major: Civil Engineering

Publications, Presentations and Awards:

Bagheri, S., Peters, S. and Yu, T.,
"Retrieval of Water Quality Constituents Concentrations from AVIRIS data in Hudson/Raritan Estuary"
Intl Jour. Remote Sensing. Paper # RES 105-620 (in print), 2005.

Bagheri, S., Peters, S. and Yu, T.,
"Retrieval of Marine Water Constituents Using Atmospherically Corrected AVIRIS Hyperspectral Data"
NASA/AVIRIS Workshop, NASA/JPL, Pasadena, CA. 3/30-4/2, 2004.

Bagheri, S. and Yu, T.,
"Utility of MIM in application of Remote Sensing for Case 2 Waters"
NASA/AVIRIS Workshop, NASA/JPL, Pasadena, CA. 3/30-4/2, 2004.

Bagheri, S. and Yu, T.,
" GIS in Land Suitability Analysis"
ESRI International User Conference – Image Submission, 2004.

Ting Yu

First Place in the Graduate Division, American Water Works Association NJIT Poster Session, 2003.

Bagheri, S., Stamnes , K. and Yu, T.,

"Forward and Inverse Modeling in Case 2 Waters for Use with Remote Sensing Data"

NASA/AVIRIS Workshop, NASA/JPL, Pasadena, CA. 2/25-2/28, 2003.

Ting Yu

First Place in the Graduate Division, American Water Works Association NJIT Poster Session, 2002.

Bagheri, S and Yu, T.,

"Utility of Remote Sensing in Assessing Algal Related Water Quality in the Hudson/Raritan Estuary"

EPA Sixth Marine and Estuarine Shallow Water Conference, Atlantic City, NJ, 3/18- 3/22, 2002.

Bagheri, S., Stamnes, K., Wei Li, W., Yu, T., and Shigan J.,

"Validation of Water Quality Parameters Retrieved from Inverse Modeling"

AVIRIS Geoscience Workshop. NASA/JPL, Pasadena, CA. 3/5-3/8, 2002.

This dissertation is dedicated to
my parents, my wife and my brother.
Their constant love and caring are every reason
for where I am and what I am.
My gratitude and my love to them are beyond words.

ACKNOWLEDGMENT

I would like to express my deepest appreciation to my advisor, Dr. Sima Bagheri, for her support, patience, and encouragement throughout my graduate studies. It is not often that one finds an advisor who always finds the time for listening to the little problems and roadblocks that unavoidably crop up in the course of performing research. Her technical and editorial advice was essential to the completion of this dissertation and has taught me innumerable lessons and insights on the workings of academic research in general. Without her guidance, supervision and her motivation, this research could never have been completed.

Special thanks are given to Dr. Hsin-Neng Hsieh, Dr. Lisa Axe, Dr. Taha Marhaba and Dr. Eliza Michalopoulou for actively participating in my committee.

Financial support has been provided by National Science Foundation (Grant # BES 9806982) and the Department of Civil and Environmental Engineering, New Jersey Institute of Technology.

TABLE OF CONTENTS

TABLE OF CONTENTS
(Continued)

TABLE OF CONTENTS
(Continued)

Chapter **Page**

LIST OF TABLES

LIST OF FIGURES

LIST OF FIGURES

CHAPTER 1

INTRODUCTION

The color of natural water is determined by the light scattered out of the water and light reflected at the water surface. Light originating from below the water surface shows characteristic influences of the diverse colors of components in the water. Parameters related to water color and recorded by ocean color sensors are used to study environmental processes like the primary production of biomass and the distribution of suspended matter.

Measurements of the spectral distribution of light intensity can be obtained by optical remote sensing, a technique to collect color data by detection of upward radiance at a distance. Remotely sensed data can provide greater economy in many types of hydrologic surveys than using conventional methods. This is possible since certain biological and geochemical constituents of surface/nearsurface water produce changes in reflectance that can be measured by the remote sensing sensors (Bagheri et al., 2005). Three important optical properties used for monitoring water quality are the concentrations of chlorophyll_a (CHL_a), color dissolved organic matter (CDOM) and total suspended material (TSM). In coastal water, the major constituents are the CHL_a, CDOM, TSM and the water itself causing absorption and scattering of light. The intensity of reflected light increases with the amount of scattering and decreases by absorption. Remote sensing of coastal waters has developed since the early seventies from an empirically based method producing qualitative water quality maps to more quantitative methods such as semi-analytical and analytical methods, which produce thematic maps

of spatial and temporal distribution patterns of parameters of water quality based on the image interpretation and calibration.

With respect to remote sensing, two main types of seawater have been defined (Morel and Prieur, 1977; Gordon and Morel, 1983). Case I waters are characterized by a strong correlation between scattering and absorbing substance concentrations and the chlorophyll_a concentration. Open ocean surface water is typical Case I water. Case I waters can be characterized by a single parameter - chlorophyll concentration. Case II waters are characterized by a lack of any correlation between scattering and absorbing substance concentrations and chlorophyll_*a* concentration as an indication of phytoplankton. Coastal waters are often referred to as Case II water, where the marine phytoplankton is not the dominant, optically active water substance. Particulate matter and colored dissolved organic matter (CDOM), which do not always co-vary with chlorophyll, also affect case II water optical properties. Case II water can be referred to as multiparameter water. It must be acknowledged that this classification concept is somewhat idealized because, in reality, all waters belong to an intermediate case (Gordon et al., 1975).

For analysis and interpretation of the ocean color, whether observed from just beneath the sea surface or at satellite altitudes, Morel and Gordon (1980) describe three approaches: (i) an empirical method, relying completely on statistical relationships between the upward radiance at the sea surface and the quantity of interest; (ii) a semi-analytical method, in which the spectral characteristics of the parameters of interest are known and some modeling of the physics is introduced; and (iii) an analytical method, in which radiative transfer models are used to extract the inherent optical properties (IOPs)

and a suite of analysis methods can be used to optimally retrieve the water constituents from the remotely sensed upwelling radiance or irradiance reflectance signal.

In the open ocean (Case I), it is not difficult to derive empirical algorithms relating the received radiances to surface concentration of water quality parameter CHL_a. In Case II waters, however, this is much more difficult due to the presence of high concentrations of suspended sediments and dissolved organic material, which interfere with the spectral signal from chlorophyll_a. In this research, the analytical approach is selected as the principal method because of the availability of atmospherically corrected AVIRIS data developed as a part of the NSF supported project (BES-9806982).

The focus of this research is the modification and application of analytical algorithms to characterize the physically based surface spectral reflectance for the waters of the Hudson/Raritan Estuary and to retrieve the water constituent concentrations from the NASA Airborne Visible/Infrared Imaging Spectrometer (AVIRIS) and LIght Detection And Ranging (LIDAR) signals. The approaches used here are based on the capabilities of AVIRIS and LIDAR data which can potentially provide a better understanding of how sunlight interacts with estuarine/inland water, especially when complemented with in situ measurements for analysis of water quality parameters and eutrophication processes (Bagheri et al., 1999 and Bagheri et al., 2001).

This research is aimed to provide quantitative data in support of use of remote sensing and GIS technologies as an operational monitoring tool for better management of water quality conditions of Hudson/Raritan Estuary.

CHAPTER 2

CONCEPTS AND THEORY

2.1 Inherent Optical Properties (IOPs)

Apparent optical properties are those characteristics of the water body that are dependent on the ambient light; therefore, the measurements can not be taken in the laboratory, only in situ. By contrast, Inherent Optical Properties (IOP) are independent of the illumination, and they do not depend on the angular radiance distribution of the incident light field (Preisendorfer, 1976). The two basic inherent optical properties are:

1. Absorption coefficient a
2. Scattering function $\beta(\theta, \phi)$

In general optical properties depend on the wavelength of the incident radiation, but the wavelength dependency is omitted in the notation unless it contributes to the clarity of the formulas.

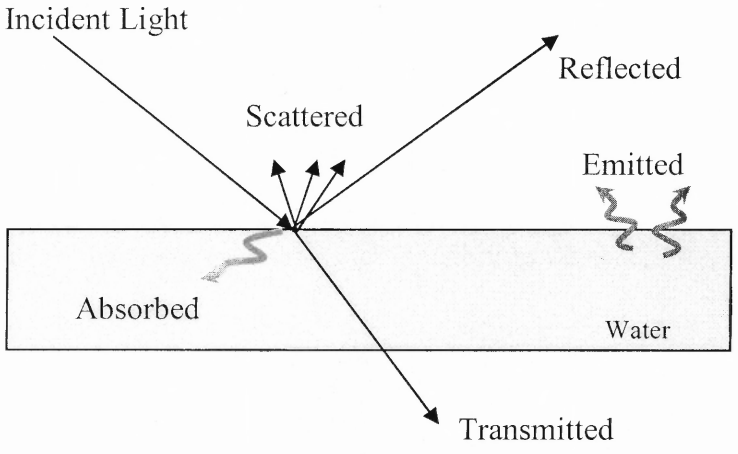

Figure 2.1 Basic interactions between electromagnetic energy and an earth surface feature

2.1.1 Absorption Coefficient (*a*)

Absorption is the ability of matter to absorb light energy impinging on it. This light energy is converted into heat, or in the case of plant matter, it is converted into photosynthetic energy or secondary energy processes such as fluorescence emission. The net light lost from an incident beam of light is referred to by the absorption coefficient or absorbance.

The definition of the absorption coefficient (*a*) is the fraction of the incident flux absorbed divided by the thickness of an infinitesimally thin layer of medium (Krijgsman, 1994).

The amount of light absorbed by materials in the water depends on the materials themselves and the wavelength of light incident upon them. By varying the wavelength of light, one can deduce information relating to specific material in the water. This is a basic principle behind spectrophotometry. Figure 2.2 shows the absorption spectra of two different phytoplankton species commonly found in Hudson/Raritan Estuary.

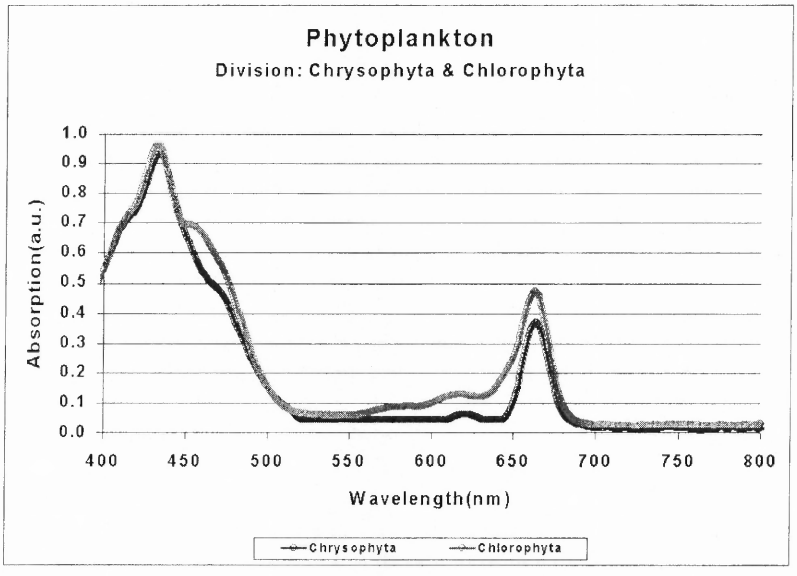

Figure 2.2 Absorption spectra of two phytoplankton species (Chrysophyta and Chlorophyta) commonly found in Hudson/Raritan Estuary
(Bagheri, 1996)

Various laboratory techniques are reported in the literature to measure absorption spectra of suspensions of particulate matter (Krijgsman, 1994). The methods differ with respect to the illumination of the sample, sample preparation, detection optics, the amount of scattering included, and the calibration factor between the optical and geometric path length.

In Case II water, total absorption a includes the absorption of seawater a_w, and the absorption of all constituents a_t. Herein, assume that the absorption is caused by three absorbing constituents: phytoplankton a_{ph}, CDOM a_{CDOM}, and TSM a_{TSM}:

$$a = a_w + a_{ph} + a_{CDOM} + a_{TSM} \tag{2.1}$$

2.1.2 Scattering Coefficient (*b*)

The volume scattering function $\beta(\theta, \phi)$ describes the angular distribution of the light scattered out of the direction of an incident ray, with θ the angle of light scattered away from this direction and ϕ the azimuth angle. The volume scattering function becomes independent of the azimuth angle ϕ for spherical particles without internal structure and for randomly oriented particles of arbitrary shape; therefore, scattering function $\beta(\theta)$ can be substituted for $\beta(\theta, \phi)$ (Krijgsman, 1994).

Scattering coefficient (b) is defined as fraction of the incident flux scattered divided by the thickness of an infinitesimally thin layer of medium (Krijgsman, 1994).

$$b = 2\pi \int_0^{\pi} \beta(\theta) \sin(\theta) d\theta \tag{2.2}$$

Forward scattering coefficient b_f is the integral of the volume scattering function $\beta(\theta)$ over the hemisphere preceding the incident flux (defined by the angular ranges $0 \leq \theta \leq \pi$).

$$b_f = 2\pi \int_0^{\pi/2} \beta(\theta) \sin(\theta) d\theta \tag{2.3}$$

Similarly, backscattering coefficient b_b is the integral of the volume scattering function $\beta(\theta)$ over the hemisphere trailing the incident flux (defined by the angular ranges $\pi/2 \leq \theta \leq \pi$).

$$b_b = 2\pi \int_{\frac{\pi}{2}}^{\pi} \beta(\theta) \sin(\theta) d\theta \tag{2.4}$$

The total backscatter coefficient b_b is the scalar sum of the backscatter of seawater b_{bw} and all constituents b_{bt} (Krijgsman, 1994). That is,

$$b_b = b_{bw} + b_{bt} \tag{2.5}$$

The backscattering coefficient of all constituents in seawater b_{bt} is difficult to measure. Petzold's results in San Diego Harbor (1977) are in common use to model scattering characteristics of turbid surface water. Because the relationship, $b_{bt} = 0.019\ b_t$, was developed over a broad wavelength band and the presence of a wide variety of particle types and sizes in any given sample, the relationship may represent a wavelength-independent average backscattering ratio. The b_{bt}/ b_t ratio of 0.019 is of the same order of magnitude as that derived experimentally by Sydor and Arnone (0.013) and from measurements by Morel (1988) as the value of 0.021.

2.1.3 Beam Attenuation Coefficient (c)

Attenuation is the total light lost from a beam of light propagating through water. These losses are due to scattering from suspended materials and the molecular scattering of the water itself, and to particulate and dissolved materials and the water itself absorbing the light. The amount of attenuation is primarily dependent upon the wavelength of the propagated light, the concentration of suspended materials and the concentration and composition of both particulate and dissolved absorbing materials. The decrease in light energy from a collimated beam that is passing through a water sample at a specific wavelength is the beam attenuation coefficient (Krijgsman, 1994).

By the definition of beam attenuation coefficient, the relationship between beam attenuation coefficient c and other IOPs is:

$$c = a + b \tag{2.6}$$

2.2 Specific Inherent Optical Properties (SIOPs)

Specific Inherent Optical Properties (SIOPs) are the inherent optical properties of a water column that can be attributed to the individual scattering and absorption centers comprising the water column. Correspondingly, there are specific absorption coefficient a^*, specific scattering coefficient b^*, and specific backscattering coefficient $b_b{}^*$.

The combined processes of absorption and scattering control the manner in which impinging radiation propagates through a natural water body. The nature and magnitude of these absorption and scattering processes are controlled by the bulk optical properties

of the aquatic medium. The bulk optical properties are, in turn, direct consequences of the amounts of scattering and absorption that may be attributable to each optically significant organic and inorganic component comprising the natural water body. These absorption and scattering which are referred to as specific absorption and specific scattering coefficients, therefore, provide the direct linkages between the optical properties of a natural water body and its composition (Bukata et al., 1995).

Specific absorption coefficient a^* is the absorption a at wavelength λ that may be attributed to a unit concentration of aquatic component i, C_i.

$$a_i^* = \frac{a}{C_i} \tag{2.7}$$

Similarly, the specific scattering b^* and backscattering coefficient $b_b{}^*$ are the scattering b and backscattering b_b at wavelength λ that may be attributed to a unit concentration of aquatic component i, C_i.

Specific scattering coefficient:

$$b_i^* = \frac{b}{C_i} \tag{2.8}$$

Specific backscattering coefficient:

$$b_{bi}^* = \frac{b_b}{C_i} \tag{2.9}$$

Based on the relationship between IOPs and SIOPs (Equations 2.7 ~ 2.9), the constituent concentrations may be obtained from their specific absorptions upon retrieval of the IOPs. Those two matrix inversion models described in this thesis will also apply the above relationship to retrieve the constituent concentrations.

2.3 Apparent Optical Properties (AOPs)

Apparent optical property is an optical property of a water body that is dependent upon the spatial distribution of the incident radiation. Apparent optical properties depend on both the inherent optical properties and the characteristics of the light field (Preisendorfer, 1976).

The two basic apparent optical properties are:

1. Irradiance $E(\lambda)$
2. Volume reflectance R(λ,z)

2.3.1 Irradiance $E(\lambda)$

Irradiance is the radiant flux per unit area at a point within a radiative field or at a point on an extended surface (Krijgsman, 1994). As apparent optical properties, irradiance can be used to estimate the inherent optical properties of water. It includes upwelling and downwelling irradiance, E_u and E_d.

The upward irradiance $E_u(z)$ is the integral overall upward directions of the radiance distribution measured with a flat cosine detector looking downward, and the absolute value of the cosine of the zenith angle were used to obtain positive values.

$$E_u(z) = \int_{\phi=0}^{2\pi} \int_{\theta=\pi/2}^{\pi} L(z,\theta,\phi) \mid \cos\theta \mid \sin\theta d\theta d\phi \tag{2.10}$$

where, θ is the zenith angle and ϕ is the azimuth angle.

The downward irradiance $E_d(z)$ is the integral over all downward directions of the radiance distribution measured with a flat cosine detector looking upward.

$$E_d(z) = \int_{\phi=0}^{2\pi} \int_{\theta=0}^{\pi/2} L(z,\theta,\phi)\cos\theta \sin\theta d\theta d\phi \tag{2.11}$$

2.3.2 Reflectance *R(z)*

The reflectance *R(z)* is defined as the ratio of the measured upwelling irradiance to the downwelling at a given wavelength (Krijgsman, 1994). For the special case of underwater reflectance, this reflectance is termed the subsurface irradiance reflectance or the volume reflectance.

$$R(0-) = \frac{E_u}{E_d} \tag{2.12}$$

CHAPTER 3

LITERATURE REVIEW

3.1 Application of Remote Sensing in Ocean Color Study

The goal of measuring ocean color is to estimate the concentrations of certain water constituents such as phytoplankton biomass, dissolved organic and inorganic matter and suspended particles.

Since the launch of Landsat in 1972, the images have been used to detect the chlorophyll and suspended solid concentrations of seawater. Sensors used onboard the Landsat series of satellites were the Multispectral Scanner (MSS) and the Thematic Mapper (TM). Each of these sensors collected data over a swath width of 185 km, with a full scene being defined as 185 km x 185 km. Alfoldi and Munday (1978) applied Landsat MSS and TM in discriminating suspended solids. Khorram and Cheshire (1983) used Landsat MSS digital data combined with surface measurements of water quality parameters to map conditions in the Neuse River Estuary, North Carolina. Kozasa (1984) studied the distribution of chlorophyll in the East China Sea using Landsat images. Almanza et al. (1985) evaluated the seasonal differences of chlorophyll concentration in Mono Lake, California based on Landsat images. Aranuvachapun and Walling (1988) examined Landsat MSS radiance data for estimating suspended solids concentrations in the Lower Yellow River, China. Lyon et al. (1988) processed multitemporal Landsat data to determine water quality parameters in Sandusky Bay, Lake Erie. Doerffer et al. (1989) analyzed Landsat TM data with respect to its capability for mapping the complex structure and dynamics of suspended-matter distribution in the coastal area of the German Bight. Jensen et al. (1989) attempted to model salinity and suspended solids distributions

in Laguna de Terminus, Mexico, using Landsat TM data. Ritchie et al. (1990) compared six concurrent Landsat MSS and TM scenes to relate Landsat digital data to suspended solids, chlorophyll and temperature in the surface water of Moon Lake, Mississippi. Schiebe et al. (1992) evaluated several possible models linking Landsat MSS data and measurements of suspended solids in Lake Chicot, Arkansas.

The data collected with Coastal Zone Color Scanner (CZCS) during 1978-1986 demonstrated the value of space observations of water-leaving radiance. For measurements of phytoplankton pigment chlorophyll concentrations, the green/blue radiance (G/B ratio) was normally used (Clark, 1981, Gordon et al., 1980). In general the G/B ratio technique works best in oligotrophic waters such as the open ocean, where the chlorophyll concentration is low and the upwelling blue radiance is high (Gower and Borstad, 1981). In estuarine (Case II) waters, however, greater chlorophyll absorption, CDOM absorption and organic detritus absorption result in very low blue reflectance and therefore the G/B ratio becomes increasingly insensitive at higher pigment concentrations. Estimated errors based on the use of CZCS data are reported to be up to 50% in chlorophyll concentration (Gordon et al., 1983). This problem is compounded by the insensitivity of the sensor to dissolved organic matter.

The Advanced Very High Resolution Radiometer (AVHRR) on the NOAA polar-orbiting meteorological satellites has provided almost daily imagery at a 1km pixel size for over 25 years. While the visible bands on the instrument were designed for cloud and land studies, they have shown value in the study of turbid coastal water (Stumpf and Pennock, 1989; 1991; Stumpf et al., 1993; Gower, 1994; Walker et al., 1994; Walker,

1996). To date, AVHRR offers the instrument for documenting changes in water clarity occurring within large estuaries.

During 1990's, data from other earth observing satellite-based sensors has aided researchers in the study of ocean productivity, color, and pollution conditions. These include the Sea viewing Wide Field of view Sensor (SeaWiFs) and the Moderate-resolution Imaging Spectroradiometer (MODIS). SeaWIFS, the ocean color satellite, images the oceans at 1 km resolution in six visible spectral bands compared to the four bands of CZCS. SeaWIFS is an improvement over CZCS in sensor noise and calibration. The six narrow visible bands center at 412 nm, 443 nm, 490 nm, 510 nm, 555 nm (for water leaving radiance measurements) and 670 nm (for aerosol radiance measurement). For ocean study, algorithms have been developed for data processing such as SeaWiFS Ocean Color 2 band algorithm (OC2) and Ocean Color 4 band algorithm (OC4) (O'Reilly, 2000; Gohin et al., 2002). Also empirical and neural network algorithms were developed for estimation and validation of Chl-a from SeaWiFS data (O'Reilly, 1998; Habbane et al., 1998; Keiner and Brown, 1999; Kahru and Mitchell, 1999). SeaWiFS Data Analysis System (SeaDAS) software was developed specifically for SeaWiFS data processing (Baith et al., 2000).

MODIS is the key instrument aboard the satellites Terra (EOS AM-1), launched on 18 December 1999 and Aqua (EOS PM-1), launched on 4 May 2002. MODIS views almost the entire surface of the Earth every day, acquiring data in 36 spectral bands over a 2330 km swath. MODIS is ideal for monitoring large-scale changes in the biosphere providing new insights into the global carbon cycle investigations. Some algorithms have

been developed to retrieve CHL-a concentrations using MODIS data (Clark, 1999; Carder et al., 2003; Gross et al., 2004.).

Although satellite remote sensing is a proven technique for monitoring and analyzing water bodies, most available satellite sensors with suitable resolutions were designed for land applications or large scale ocean study (Case 1 water) (Hilton 1984; Han et al., 1994; Dekker and Peters, 1993). Therefore, the number of spectral channels, their distribution, and the range of brightness have not been optimized for water resource monitoring. As a result, the application of Landsat, SeaWIFs and MODIS images to studies of Case II water systems have been limited mainly by the low spatial resolution and poor spectral band location with respect to the features of most interest in the reflectance spectrum.

In recent years, imaging spectrometers have become available which have higher spatial and spectral resolutions. Imaging spectrometers, or hyperspectral sensors, are instruments that acquire multispectral images in many, very narrow, contiguous spectral bands throughout the visible, near-IR, and mid-IR portions of the spectrum. These systems typically collect 200 or more channels of data, which enables the construction of an effectively continuous reflectance spectrum for every pixel in the scene. The intent of these systems is to permit discrimination among earth surface features that have diagnostic absorption and reflection characteristics over narrow wavelength intervals that are "lost" within the relatively coarse bandwidths of the various channels of a conventional multispectral scanner (EARSEL, 1991). Initial imaging spectrometry research was conducted with data acquired by the Airborne Imaging Spectrometer (AIS) in 1985. This system collected 128 channels of data, which were approximately 10nm

wide in contiguous between 1200nm and 2400nm. Literature review indicates the successful use of the airborne imaging spectrometers such as Compact Airborne Spectrographic Imager (CASI), CCD Airborne Experimental Scanner for Applications in Remote Sensing (CAESAR) and Geophysical and Environmental Research Imaging Spectrometer (GERIS) with high spectral resolution in environmental applications (EARSEL, 1991).

A second-generation airborne imaging spectrometer is the Airborne Visible-Infrared Imaging Spectrometer (AVIRIS). This system typically collects data in 224 channels, at 9.6nm interval, in contiguous bands between 400nm and 2450nm.

Latest reports on the use of AVIRIS data over water have been very encouraging. Carder et al. (1993) have used AVIRIS data in the study of dissolved and particulate matter in Tampa Bay, Florida. In another water application, Hamilton et al. (1993) used AVIRIS data to study chlorophyll concentration and bathymetry in Lake Tahoe. Dekker and Hoogenboom (1996) presented results of their modeling efforts on simulated AVIRIS data in which the specific inherent optical properties (SIOPs) were related to the subsurface reflectance, R(0-), over eutrophic lake waters. In more recent water applications of the AVIRIS, Gastil and Melack (1998), and Bagheri et al. (1999, 2000, 2001, 2002, 2003) demonstrated an improved retrieval of chlorophyll concentrations using atmospherically corrected multitemporal AVIRIS data in inland lake and nearshore environment respectively. Table 3.1 compares AVIRIS with other sensors.

Table 3.1 Technical Differences Between Landsat MSS, TM, AVHRR, SeaWIFs, MODIS and AVIRIS

Sensors / Items	Landsat MSS	Landsat TM	AVHRR	SeaWIFs	MODIS	AVIRIS
Platform	Satellite	Satellite	Satellite	Satellite	Satellite	Aircraft
Swath Width (km)	185	185	2400	1502	2330	11
Application Scale	Large Scale	Large Scale	Large Scale	Large Scale	Large Scale	Small Scale
Number of Bands	4	7	5	8	36	224
Wavelength Range(nm)	500 ~ 1100 (continuous)	450 ~ 12500 (discrete)	580~ 12500 (discrete)	412 ~ 865 (discrete)	405 ~ 14385 (discrete)	400 ~ 2500 (continuous)
Band Interval (nm)	≥ 100	≥ 60	≥ 100	≥ 20	≥ 10	≈ 10
Resolution (m)	≥ 80	≥ 30	1000	1000	≥ 250	= 20

(Source: http://www.nasa.gov)

Airborne ocean color measurement can be separated into two distinct subdivisions (passive and active) defined by the two individual methods of detection and measurement. Passive ocean color measurement is the original, traditional method whereby incident solar radiation is diffusely backscattered into a spectroradiometer (Hoge et al, 1981). CASI, CAESAR, GERIS and AVIRIS mentioned above all belong to passive airborne measurement. Active ocean color measurement is defined herein as the received fluorescence or other backscatter resulting from the stimulation of the water column with man-made electromagnetic radiation such as from laser (Hoge et al., 1986). The most common active ocean color measurement system is the fluorescence LIDAR.

Fluorescence refers to the characteristic of various materials to absorb energy of one wavelength and then reemit energy, generally at a longer wavelength, shortly after excitation by the original energy source (Bristow et al., 1981). Fluorescence signal from the crop of phytoplankton was first identified by Morel and Prieur (1977) from subsurface measurements of spectral diffuse reflectance and by Neville and Gower (1977) from measurements of nadir radiance above the sea surface. Gordon (1979) and Kattawar and Vastano (1982) presented a mathematical description of the relationship between this natural or solar-induced fluorescence, the concentration of CHL_a, and the ambient light intensity which excites the fluorescence. Based on those studies, Fluorescence Line Imager (FLI) was developed in the 1970's and designed to have sufficient sensitivity and spectral resolution to measure chlorophyll pigments by making use of their characteristic fluorescence (Gower and Borstad, 1981; Hollinger et al., 1987). Unfortunately the system was poorly calibrated and was sensitive to internal scattering. More recently, Kishino et al. (1984a, b), Topliss (1985), Topliss and Platt (1986), Dirks and Spitzer (1987), and Preisendorfer and Mobley (1988) have further investigated factors affecting natural fluorescence in the field.

Based on the FLI method, the Airborne Oceanographic Lidar (AOL) Fluorosensor was built by the AVCO Everette Corporation under a joint program sponsored by NASA, NAVOCEANO, and NOAA in the 1977. The purpose of the joint interagency program was to allow investigation of the potential for an airborne laser sensor in the areas of altimetry, hydrography, and fluorosensing. During the past 17 year period, the instrument has undergone considerable modifications including several major redesigns. The instrument modifications and the results of investigations with the AOL for various

marine and terrestrial applications have been reported in numerous papers presented in refereed journals (Hoge et al, 1980; Hoge and Swift, 1983; Krabill et al, 1984; Hoge et al., 1986; Wadhams et al., 1992).

The NASA AOL Fluorosensor is a laser fluorospectrometer (and associated instruments) which is carried onboard a NASA P-3B or NASA C-130 aircraft. The AOLFL measures a variety of reflected and induced light properties, from which a number of oceanographic surface water properties can be derived. It was designed to have sufficient sensitivity and spectral resolution to measure chlorophyll pigments by making use of their characteristic fluorescence (Hoge, 1986; Chekalyuk et al., 2000; Wright et al., 2001). The AOL fluorosensor uses a pulse of laser light fired from the aircraft down into the ocean. The laser light hits the single celled plants in the ocean. The chlorophyll inside the plants absorbs the laser light, and fluoresces, giving off red light, in much the same way as certain paints glow under a "black light". A telescope onboard the aircraft collects the light from the plants, and electronic equipment converts the signal into numbers a computer can record. Literature search indicates successful applications of AOL Fluorosensor and retrieval of IOPs on the shelf, the slope, Gulf Stream and in the Sargasso Sea (Hoge and Lyon, 1996; Hoge and Lyon, 1999; http://aol.wff.nasa.gov, 2004).

It should be noted that rather large variations in the penetration depth of the laser beam may exist over short horizontal distances, particularly in the near-shore portion (Hoge et al., 1983). If left uncorrected, this spatial variability in water column optical attenuation would manifest itself as variability in the pigment fluorescence signal caused by the laser beam not fully accessing the constituent fluorophores. Since the Raman

scatter is due only to the water molecules, the relative penetration depth may be defined by the strength of this spectral line. Thus, the apparent variation of pigment fluorescence caused by water column optical attenuation can be corrected by normalization using the water Raman backscatter signal (Hoge and Swift, 1981; Hoge and Swift, 1983; Bristow et al., 1981). The use of this technique assumes that the fluorophores are uniformly distributed in the water column volume being sensed. The water Raman normalization procedure has been found to produce an essentially linear response to chlorophyll concentrations (Bristow et al., 1981). The water Raman normalization technique has become an accepted method for removing the variability of water column optical attenuation effects.

Bristow et al. (1981), Hoge and Swift (1983), Poole and Esaias(1982) and Exton et al. (1983) found a nearly linear relationship between normalized laser-induced fluorescence and in situ chlorophyll concentration in laboratory tests using both natural and artificial mixtures:

$$C = k \cdot \frac{f}{r} \tag{3.1}$$

Where,

C---chlorophyll concentration

k---coefficient of the linear relationship between normalized laser-induced fluorescence and chlorophyll concentration

$\frac{f}{r}$---normalized fluorescence signal by water Raman signal

In this study, a combination of data from dedicated flights acquired by hyperspectral (AVIRIS) and AOL were used in order to take advantage of those wavelengths necessary for detailed analysis of the Hudson/Raritan estuarine (Case II) waters.The unique capability of AVIRIS and LIDAR data potentially can provide better understanding of how both sunlight and laser light interact with estuarine/inland water, especially when complemented with in situ measurements for analysis of water quality parameters and eutrophication processes. The AVIRIS uses the absorption-based principles, and AOL uses fluorescence-based principles. The fluorescence-based algorithm is not likely to be influenced by CDOM absorption since the CDOM absorption in the red part of the spectrum is negligible. The main differences between the two techniques are outlined in Table 3.2 (IOCCG,1999). Note that both techniques require calibration against in-situ measurements.

Table 3.2 Technical Differences Between Absorption-based and Fluorescence-based Signals of Chlorophyll_a

Absorption-based signal	Fluorescence-based signal
Non-linear function of chl-a	Often linear function of chl-a
Algorithm sensitivity greatest at low chl-a concentration	Algorithm most effective at high chl-a concentration
Algorithm vulnerable to CDOM absorption	Algorithm little influenced by CDOM absorption
"Penetration depth" high in the blue-green part of the spectrum	"Penetration depth" low in the red part of the spectrum
Atmospheric correction very critical	Atmospheric correction less critical
Potentially, information on CDOM and suspended sediments retrieved as a by-product	Distinct signal, unconnected to other substances of interest

(Source: IOCCG,1999)

3.2 Review of Bio-optical Models

To develop analytical algorithms for Case II waters, an optical model needs to link the water quality parameters (WQPs) to the Inherent Optical Properties (IOP), linking these in turn to the subsurface irradiance reflectance R(0-) (Bagheri, 2004).

3.2.1 Gordon's 1975 Optical Water Quality Model

To construct a bio-optical model which relates the constituent concentrations to the subsurface irradiance reflectance, R(0-), several workers have investigated the relationship between R(0-) and the IOPs for ocean and inland water systems (Gordon et al., 1975; Whitlock et al., 1981; Kirk, 1991; Krijgsman, 1994). Dekker et al. (1997) found that the following model originally developed by Gordon (1975) was appropriate for Case II waters:

$$R(0_-) = r \cdot \left(\frac{b_b}{a + b_b}\right) \tag{3.2}$$

where:

a—total absorption coefficient

b_b—backscattering coefficient

r—a factor based on the geometry of incoming light and volume scattering in water

The IOP a and b_b were assumed to be linear functions of the constituent concentrations. This allowed the SIOP to be introduced that link the concentrations of all optically active components to the sub-surface irradiance reflectance. The IOP per unit concentration, e.g. the specific inherent absorption by phytoplankton, a^*_{ph}, was the absorption caused by 1mg m^{-3} CHL (Equation 2.7). Using Beer's law (Equation 2.1), the

total absorption coefficient a can be written as sum of the absorption by phytoplankton, TSM, CDOM, and water. It should be noted that specific absorption for CDOM could not be calculated because no concentrations of DOC or POC were measured during field data analysis. Therefore, the CDOM absorption measured at 440 nm was taken as measure of concentration. The values for absorption coefficient (a_w) and the scattering coefficient (b_w) of pure water were taken from Bukata (1974) The backscattering (b_b) is used here which is based on the conversion of the scattering coefficient to the backscattering coefficient. The volume scattering function of Petzhold (Kirk, 1994) is assumed to be valid, therefore b_b was obtained as $0.019b$. For pure water, this ratio is 0.5 but for seston measurements depends on the composition of the water (Morel and Prieur, 1977).

$$a = a_w + a^*_{TSM} \cdot TSM + a^*_{ph} \cdot CHL + a^*_{CDOM} \cdot CDOM_{440} \tag{3.3}$$

$$b_b = 0.5 \cdot b_w + b^*_{bTSM} \cdot TSM \tag{3.4}$$

Where:

a_w — absorption of pure water

b_w — scattering of pure water

a^*_{ph} — specific absorption of the phytoplankton

$b_b{}^*_{TSM}$ — specific backscatter of TSM

a^*_{TSM} — specific absorption of TSM

a^*_{CDOM} — specific absorption of CDOM

0.5 — backscatter to scatter ratio of pure water

Equation 3.2, $R(0\_) = r \cdot (\frac{b_b}{a + b_b})$, has been widely used for retrieval of water quality parameters concentrations. For example, Hoogenboom (1998) and Hakvoort

(2000) used it to develop the matrix inversion models which are described in matrix inversion models (MIM) section of the thesis.

3.2.2 Gordon's 1988 Optical Water Quality Model

Gordon and Clark (1981) defined the normalized water-leaving radiance L_w as:

$$L_w(\lambda) = F_0 t(\theta_0)\cos(\theta_0) M \, R/Q \tag{3.5}$$

where F_0 is the extraterrestrial solar irradiance, θ_0 is the solar zenith angle, $t(\theta_0)$ is the diffuse transmittance of the atmosphere, and R is the irradiance reflectance just beneath the sea surface. $R = E_u / E_d$, where E_u and E_d are the upwelling and downwelling irradiances, respectively, just beneath the surface. Q is the ratio of the upwelling radiance to the upwelling irradiance toward zenith. Q equals π for a totally diffuse radiance distribution and, although it has received little experimental attention, appears to be between 4 and 5 and somewhat dependent on wavelength for radiance distributions observed in nature (Austin, 1979). M is defined by $M = \frac{(1-\rho)(1-\bar{\rho})}{m^2 Q(1-rR)}$, where ρ is the Fresnel reflectance of the sea surface for normal incidence, $\bar{\rho}$ is the Fresnel reflection albedo of the sea surface for irradiance from the sea and sky, m is the index of refraction of seawater, and r is the water-air reflectance for totally diffuse irradiance. For the (1-rR) term, $r \sim 0.48$ and accounts for the effect of internal reflectance of the upwelling radiance field by the sea surface. Nearly independent of wind speed, the value of ρ is taken to be 0.021 over the visible spectrum (Hoge, et al., 1996). Gordon et al.,(1988) further indicate that $\bar{\rho}$ depends in a complicated manner on the solar zenith angle through the

dependence of the relative amounts of direct sunlight and diffuse skylight incident on the sea surface. Finally, Gordon et al. (1988) suggest that for $0 \leq \theta_0 \leq 60^0$, the term $(1-\bar{\rho})$ would be expected to vary between 0.934 and 0.979. For those conditions, M was chosen to be a constant ~ 0.55. For the research herein the solar zenith angle θ_0 was held fixed at zero degrees and the effect of atmosphere assumed to be absent due to low flying altitude of the AOL, Thus, $t(\theta_0)\cos(\theta_0)=1$.

Equation (3.5) shows that L_w is related to the optical properties of the water through R and Q in the combination R/Q, which depends on the specific details of the scattering phase function in the backward direction.

Gordon et al. (1988) have determined that R/Q can be directly related to the total absorption a and the total backscatter b_b by

$$R/Q = (l_1 X + l_2 X^2) \tag{3.6}$$

where $l_1 = 0.0949$ and $l_2 = 0.0794$ (Hoge et al., 1996) were calibrated as constants parameters and $X = (\frac{b_b}{a+b_b})$.

Gordon et al. (1988) also concluded that the error in (3.5) is significantly less than 10% for a wide range of realistic scattering phase functions.

Compared with Gordon's 1975 model (3.2), this model is more precise, however, more parameters need to be calibrated. Hoge and Lyon (1996) employed this model in their matrix inversion model which was used in this research.

3.3 Retrieval of Water Quality Parameters Using Bio-Optical Models

In order to analyze and interpret the color of coastal waters, Dekker and Hoogenboom (1996) redefined the definitions originally determined by Morel and Gordon concerning three possible approaches to estimate water quality parameters from remotely sensed data (Figure 3.1). Three approaches used in water quality modeling are: the empirical method, semi-analytical method and analytical method.

3.3.1 The Empirical Method

In the empirical approach, statistical relationships are sought between measured spectral values ("remote sensing image" section in Figure 3.1) and measured water parameters.

A typical example of the empirical approach is the CZCS basic algorithm (Gordon et al., 1983):

$$\log C_1 = 0.053 - 1.71 \log r(1,3) \qquad (3.7)$$

if $C_1 < 1.5$ or $C_1 > 1.5$ but $C_2 < 1.5$

$$\log C_2 = 0.522 - 2.44 \log r(2,3)$$

if $C_1 > 1.5$ and $C_2 > 1.5$

were C_1 or C_2 is the total pigment concentration, i.e., the sum of the concentrations of CHL_*a* and phaeopigments, and $r(1,3) = L_w(443)/L_w(550)$, $r(2,3) = L_w(520)/L_w(550)$ are ratios of water-leaving radiances in CZCS spectral bands. Pigment retrievals from CZCS data in Case I waters have achieved reasonable results. However, the retrieval of pigment concentration may be less than 50% accurate for Case II waters (Carder et al., 1991).

The SeaWiFS basic chlorophyll_*a* algorithm is another example of an empirical approach. It is expressed as a cubic polynomial (O'Reilly et al., 1998):

$$\log_{10}(CHL - C_0) = A_0 + A_1 \cdot r + A_2 \cdot r^2 + A_3 \cdot r^3 \tag{3.8}$$

where C_0 and A_i, i=0, 1, 2, 3 are empirical coefficients, and r=log[R_{rs}(488)/R_{rs}(555)]. R_{rs} is remote-sensing reflectance, the ratio of water-leaving radiance to downwelling irradiance just above the sea surface.

For different water bodies, those calibrated coefficients were different. The coefficients for the SeaWiFS chlorophyll *a* algorithm are: C_0 =-0.0929 mg/m^3, A_0 =0.2974, A_1 =-2.2429, A_2=0.8358, A_3 =-0.0077 (Maritorena, 1998).

The new coefficients from Liew et al. (2001) are: C_0 = -0.0414 mg/m^3, A_0 = 0.4708, A_1 = -3.8469, A_2=4.5338, A_3 =-2.4434.

However, the limitation of such empirical algorithms is that spurious results may occer, because causal relationships between the parameters are not necessarily implied. In such cases, so-called semi-analytical and analytical algorithms are promising (Dekker and Hoogenboom, 1996).

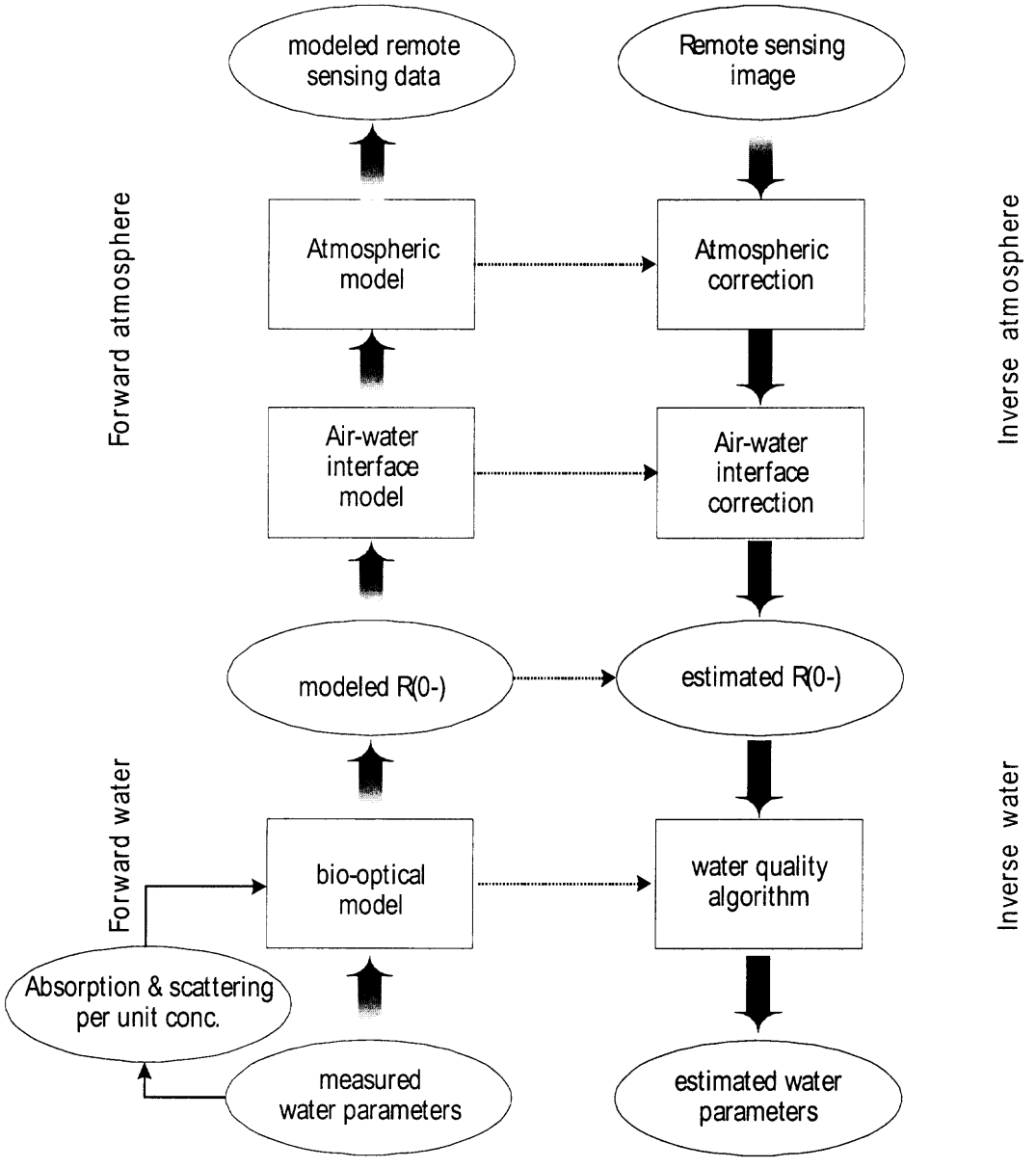

Figure 3.1 The forward and inverse model for remote sensing of water quality (Dekker et al., 1996)

3.3.2 The Semi-Analytical Method

This approach may be used when the spectral characteristics of the parameters of interest are known. In figure 3.1 this relates to the "forward water" section, but only the sections "measured water parameters" and "measured R(0-)" are used for the statistical analysis

by focusing on well-chosen spectral areas and appropriate wavebands or combinations of wavebands, which are used as correlates. Quantitatively, the coefficients from any such relationship only apply to the data from which they were derived. Each application must therefore be individually calibrated.

For the semi-analytical, Morel (1988) and Gordon (1988) were the first to introduce these methods. They created objective functions which are square of the difference between the measured and the modeled reflectance and minimized the objective functions to obtain the solutions as the spectral reflectance under the situations with different water constituent concentrations.

$$F(C_j) = \sum_j [R_{i,measured} - R_i(C_j)]^2 \Big/ \sigma_j^2 \tag{3.9}$$

where $F(C_j)$ is the objective function, which defines how well data fit the hypothesis and expresses the quantity to be minimized, $R_i=R(\lambda_i)$ is the modeled spectral reflectance, C_j is the water constituent concentrations, and $\sigma_i=\sigma(\lambda_i)$ is the spectral weighting function.

There have been many applications of the semi-analytical algorithms to the retrieval of the water optical properties and constituent concentrations since 1985 (Burenkov et al., 1985; Sugihara et al., 1985; Carder et al., 1991; Lee et al., 1994; Doerffer and Fischer, 1994; Roesler and Perry, 1995; Vasilkov, 1997; Garver and Siegel, 1997). Minimization of the nonlinear function (equation 3.9) was used in Burenkov *et al.* (1985), Lee *et al.* (1994), Doerffer and Fischer (1994), Roesler and Perry (1995), and Garver and Siegel (1997). Since the minimization of the nonlinear function of several variables (Equation 3.9) may be computationally expensive, it cannot be used for operational purposes.

3.3.3 The Analytical Method (the "inverse atmosphere" and "inverse water" sections in Figure 3.1)

In an analytical model, the apparent optical properties (AOP) and inherent optical properties (IOP) are used to model the reflectance and vice versa. Apparent optical properties include irradiance and reflectance, and the two basic inherent optical properties are absorption coefficient and volume scattering coefficient. The water constituents are expressed in their specific (per unit measure) absorption and backscatter coefficients. Subsequently a suite of analysis methods have been used to optimally retrieve the water constituents from the remotely sensed upwelling radiance or radiance reflectance signal.

In Case II water, the variation in water composition and thus in water color is wider than in Case I waters. From measurements in 125 Case II waters, it has been found that the concentration of the sum of pheaophytin and chlorophyll-a (CHL) ranges from 1 to 900 mg m^{-3}, TSM dry weight 1 to 100 g m^{-3} and CDOM (color dissolved organic matter) with an absorption coefficient g_{440} from 0 to 60 m^{-1} at 440nm (Rijkeboer et al., 1998). The presence of several non–correlated constituents makes Case II waters optically more complex than most Case I waters. The color of Case I waters quantified by the spectral subsurface irradiance reflectance, R(0-), is predominantly a function of absorption and scattering by algal pigments and water itself. In Case II waters, backscattering from particles is the dominant scattering factor. In those waters the combined effects of particulate backscattering and high absorption introduce complex interacting relations between the water constituents and subsurface irradiance reflectance. Therefore, retrieval of constituents concentrations from the reflectance requires an analytical approach (Doerffer, 1989). In the analytical approach, the retrieval is based on

a bio-optical model which describes the relation between the reflectance and the concentrations of the constituents.

To develop a purely analytical method, all optical properties in the water and reflectance must be known, since the water color is an apparent optical property of water. Water reflectance (R), the irradiance ratio of upwelling to downwelling, is another apparent optical property, which depends not only on seawater constituents but also on the ambient light environment (sky light, cloud, sea surface roughness, sea bottom conditions, etc.). However, the reflectance will be changed primarily with variations in water constituents. Hence, the ocean reflectance contains all the essential information concerning the qualitative and quantitative properties of seawater constituents (Gordon, 1975).

During the last ten years, progress has been made in the analytical inversion of relatively simple bio-optical models that simulate the underwater light field. Analytical inversion of these models leads to algorithms to retrieve concentrations of optically active constituents from remotely observed water spectra. Three analytical inversion methods have been developed, each with its own strengths and weaknesses.

(1) Matrix Inversion Method (MIM)

The linear matrix inversion developed by Hoge and Lyon (1996) retrieves the IOPs (from which the constituent concentrations are obtained). The model (Equation 3.10) describes the generation of upwelled water-leaving spectral radiance caused by backscatter and absorption of incident downwelling solar irradiance.

$$\begin{bmatrix} 1 & 1 & \nu(\lambda_1) \\ D_{21} & e^{[-S(\lambda_2-\lambda_1)]} & (\lambda_1/\lambda_2)^n \nu(\lambda_2) \\ D_{31} & e^{[-S(\lambda_3-\lambda_1)]} & (\lambda_1/\lambda_3)^n \nu(\lambda_3) \end{bmatrix} \cdot \begin{bmatrix} a_{ph}(\lambda_1) \\ a_d(\lambda_1) \\ b_{bt}(\lambda_1) \end{bmatrix} = \begin{bmatrix} h(\lambda_1) \\ h(\lambda_2) \\ h(\lambda_3) \end{bmatrix} \tag{3.10}$$

The MIM can estimate the concentrations of the constituents consistently for a wide range of inland water types. In principle, this method is capable of using all spectral information provided by different instruments, including imaging spectrometry data. The MIM is predominantly sensitive to the mean "hull" of the spectrum. For different water bodies, it is necessary to calibrate the different wavelengths - λ, spectral slopes - s, total constituent backscattering spectral exponent – n, and phytoplankton Gaussian model spectral width – g.

An alternate form of MIM was obtained by taking the correlation between TSM and CHL into account (Hoggenboom et al., 1998). Accordingly, the total TSM (TSM_{tot} = TSM_{ph} + TSM_{ss}) values include the part of the dry weight determined by the biomass of phytoplankton as correlated to CHL concentration. An average value of 0.07 (TSM_{ph}=0.07 CHL) was used here based on Buiteveld (1990).

$$CHL = \frac{A_{22}y_1 - A_{12}y_2}{A_{11}A_{22} - A_{12}A_{21}} \text{ and} \tag{3.11}$$

$$DW_{tr} = \frac{-A_{21}y_1 + A_{11}y_2}{A_{11}A_{22} - A_{12}A_{21}}$$

where,

$$A_{m1} = a^*_{ph}(\lambda_m) + 0.07a^*_{dw}(\lambda_m) + 0.07b^*_{bTSM}(\lambda_m)(1 - \frac{f}{R(\lambda_m)})$$

$$A_{m2} = a^*_{TSM}(\lambda_m) + b^*_{bTSM}(\lambda_m)(1 - \frac{f}{R(\lambda_m)})$$

$$y_m = -a_w(\lambda_m) - a^*_{CDOM}(\lambda_m)CDOM_{440} - b_{TSM}(\lambda_m)(1 - \frac{f}{R(\lambda_m)})$$

a_w----------absorption of pure water

b_{bw}----------backscatter of pure water

a^*_{ph}-----specific absorption of the phytoplankton

$b_b{}^*_{TSM}$-----specific backscatter of TSM

a^*_{TSM}-------specific absorption of TSM

R----------subsurface irradiance reflectance

a^*_{CDOM}-----specific absorption of CDOM

CDOM---average CDOM concentration

CHL----average CHL concentration

f -------a multiplication factor that depends on the apparent optical properties of the light field (Aas, 1987; Stavn et al., 1989; Kirk, 1994; Weidemann et al., 1995). An average factor of 0.34 is used by Dekker (1993) for a range of 0.12 to 0.56 values. In this research, a range of 0.28 to 0.34 for f has been used.

In the matrix inversion model introduced by Hakvoort, the retrieval of CDOM concentration was included (Hakvoort et al., 2000).

$$A_{n\times 3} \cdot x_{3\times 1} = y_{n\times 1} \tag{3.12}$$

where,

$$A = \left[\left[\frac{R(0\_)\cdot a^*_{CHL}}{f}\right]_{\lambda=1\cdots n} \quad \left[\frac{R(0\_)\cdot\left[a^*_{TSM} + b^*_{b,TSM}\right]}{f} - b^*_{b,TSM}\right]_{\lambda=1\cdots n} \quad \left[\frac{R(0\_)\cdot a^*_{CDOML}}{f}\right]_{\lambda=1\cdots n} \right]$$

$$y = \left[\left[\frac{R(0\_)\cdot\left[a_w + b_{bw}\right]}{f} - b_{bw}\right]_{\lambda=1\cdots n} \right]$$

$$x = \begin{bmatrix} CHL \\ TSM \\ CDOM \end{bmatrix}$$

The modified versions of the models as applied to data collected from Hudson/Raritan Estuary will be described in detail in the subsequent chapters.

(2) Ratio Matrix Inversion (RMI)

In the last decade, ratio-based algorithms have proven to be very successful for the determination of pigment concentrations (Dekker, 1993; Gons, 1999).

The following algorithms for estimating chlorophyll_a (CHL) were developed using the RMI method:

$$CHL = -59.0 + 78.9 \cdot \frac{R(706)}{R(676)} \tag{3.13}$$

$$CHL = 31.6 \cdot \left(\frac{R(706)}{R(676)} \right)^{1.99} \tag{3.14}$$

$$CHL = -96.5 + 20.3 \frac{R(444) - R(752)}{R(512) - R(752)} + 34.1 \frac{R(492) - R(752)}{R(512) - R(752)} + 50.2 \frac{R(556) - R(752)}{R(512) - R(752)} \tag{3.15}$$

$$CHL = 4.2 - 13.3 \frac{R(560) - R(755)}{R(520) - R(755)} + 86.6 \frac{R(620) - R(755)}{R(520) - R(755)} + 50.2 \frac{R(556) - R(755)}{R(512) - R(755)} \tag{3.16}$$

Equations (3.13) and (3.14) were by Dekker et al. (1993, 1997) based on CASI and PR650 sensors respectively. Equations (3.15) and (3.16) were used for SeaWiFS and MEdium Resolution Imaging Spectrometer (MERIS) by Althuis et al. (1996)

Peters et al. (2001) developed a new analytical method which combines the advantages of ratio algorithms (i.e., stability, robustness, etc) with the advantages of inversion using all spectral bands.

$$R = \frac{R(0-)^1}{R(0-)^2} = \frac{b_b{}^1 \cdot (a^2 + b^2)}{b_b{}^2 \cdot (a^1 + b^1)} \Rightarrow \tag{3.17}$$

$$(R \cdot C_6 \cdot a^*_{CHL}{}^1 - C_5 \cdot a^*_{CHL}{}^2) \cdot CHL + (R \cdot C_6 \cdot a^*_{TSM}{}^1 - C_5 \cdot a^*_{TSM}{}^2 + R \cdot C_2 - C_2) \cdot TSM$$
$$+ (R \cdot C_6 \cdot a^*_{CDOM}{}^1 - C_5 \cdot a^*_{CDOM}{}^2) \cdot CDOM = (C_1 - R \cdot C_1) + R \cdot C_6 \cdot a^{*1}_W + C_5 \cdot a^{*2}_W$$

with the following elaboration:

$$C_1 = 0.5 \cdot b^{*1}_w \cdot b^*_{TSM}{}^2 + 0.5 \cdot b^{*2}_w \cdot b^*_{TSM}{}^1 \qquad C_4 = \frac{0.5 \cdot b^{*2}_w}{B}$$

$$C_2 = B \cdot b^*_{TSM}{}^1 \cdot b^*_{TSM}{}^2 \qquad C_5 = \frac{C_3}{TSM} + b^*_{TSM}{}^1$$

$$C_3 = \frac{0.5 \cdot b^{*1}_w}{B} \qquad C_6 = \frac{C_4}{TSM} + b^*_{TSM}{}^2$$

B------ Backscatter to scatter ratio

Due to the non-linearity in Equation (3.15) caused by the occurrence of TSM in C_5 and C_6, the solution needs some assumptions: C_3/TSM and C_4/TSM can be neglected at higher TSM concentrations. The method requires R(0-) to be available for at least three spectral bands, a known SIOP, and a reasonable estimate of B. Thus, for any number of relevant band ratios a system of linear equations can be built that can be solved for the water quality parameters.

However, in many inland waters the reflectance and thus the ratio of two bands, is significantly influenced by TSM and CDOM (Dekker, 1993; Gitelson et al., 1993). As a result, the ratio algorithm may give ambiguous estimates of the concentrations of CHL depending on the water composition.

(3) One-band Algorithm for TSM Retrieval

One of the more successful applications in marine remote sensing is the automated operational processing of satellite images obtained by the SeaWiFS and other satellites to obtain TSM maps (Van der Woerd et al., 2000; Pasterkamp et al., 1999). SeaWiFS was designed for the analysis of clear oceanic waters and features with only six usable spectral bands for parameter retrieval. In this model, fixed values for CDOM and TCHL were adopted:

$$TSM = \frac{-(a_w + a^*_{TCHL} TCHL + a^*_{CDOM} CDOM)\frac{R}{f} + b_{bw}(1-\frac{R}{f})}{a^*_{TSM}\frac{R}{f} - b^*_{bTSM}(1-\frac{R}{f})} \tag{3.18}$$

Peters et al. (2001) performed several testing of this algorithm on independent datasets of spectra and concentrations of the Dutch North Sea, collected during the year 2001 spring bloom of algae. He found the algorithm seems to underestimate TSM at low concentrations (less than 20 mg/l) and to overestimate at higher concentrations (>20mg/l). This may be due to the fact that the Specific Inherent Optical Properties (SIOPs) for both ranges of concentrations differ from the data set on which the algorithm was calibrated. The underestimation at low concentration ranges is in accordance with the findings of Van der Woered et al., 2000, who found the same phenomenon when comparing the algorithm results (applied to SeaWiFS) with long-term field observations.

Given the strengths and weaknesses of the methods described, the modified matrix inversion models originally developed by Hoge and Lyon (1996) and Hoogenboom et al. (1998), were used as the principal models to retrieve concentrations of water quality parameters from the AVIRIS and LIDAR data acquired over the NJ/NY estuary in 2001 and calibrated with in-situ measurements. The adjustments made on the

model parameters included are phytoplankton Gaussian model spectral width - g, spectral slopes - s, total constituent backscattering spectral exponent – n and the selected wavelengths – λ (Hoge, et al., 1996; Hoogenboom et al., 1998).

CHAPTER 4

CHARACTERISTICS OF THE STUDY AREA

The study area is the Hudson/Raritan Estuary of New York – New Jersey located south of the Verrazano Narrows and bordered by western Long Island, Staten Island and New Jersey (Figure 4.1).

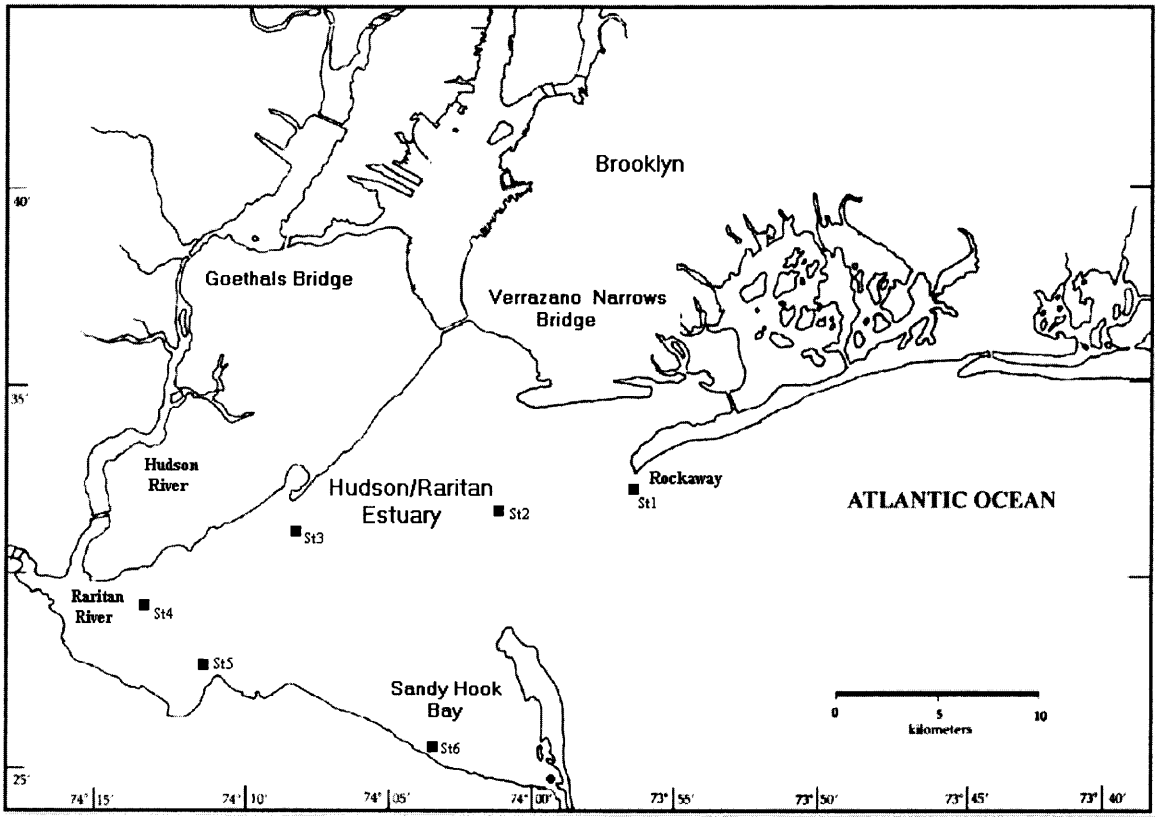

Figure 4.1 Map of study area with the locations of the sample points surveyed in 2001

The Hudson/Raritan Estuary is a complex ecosystem that is important to the New York metropolitan area and is considered "the most intensively developed and industrialized estuary on the U.S. east coast" (Pearce, 1988). The major freshwater discharges are the Hudson, Raritan, Passaic and Hackensack Rivers. Hudson/Raritan estuarine waters are degraded by municipal and industrial wastewater discharges, land runoff and combined sewer outflows, which contribute to low dissolved oxygen. The

freshwater discharge from the Hudson River contributes a monthly average discharge ranging from about 100 m^3/s in dry seasons to about 1800m^3/s in spring, while the combined monthly average discharges of the Raritan, Passaic and Hackensack rivers ranges from 10 to 100 m^3/s (Bagheri, 1999). The number of wastewater inputs include 26 major waste treatment plants, about 100 point sources of industrial and municipal origin and in excess of 700 combined storm drains and sewer outflows (O'Connor and Mueller, 1984). There are four major sewage sources; two with a combined mean discharge of 11 m^3/s are located near the mouth of the Passaic River and near the mouth of Kill Van Kull that opens to the part of the estuary. A third in the East River has a mean discharge of 42 m^3/s, and the fourth sewage source is Jamaica Bay with a mean discharge of 14 m^3/s.

The volume discharged into the system from Staten Island, New Jersey and the Raritan River is small compared to these sources. Conditions in the lower part of the estuary can be quite variable due to its shallowness and the speed with which it can change in response to factors such as tide, rain and wind. However, the net movement of water within the estuary is counter-clockwise. The following two factors govern the circulation patterns in the estuary (Oey, et al., 1985):

- The geometry of the estuary with open boundaries (Sandy Hook connection with the Atlantic Ocean and East River Strait connection with Long Island Sound)
- Surface wind stress which is considered part of the surface boundary conditions.

The partially mixed drowned river estuary is relatively shallow (< 8 m) (Oey et al., 1985). The estimated flushing time of the estuary, 16-21 days or 32 to 42 tidal cycles (Jeffries, 1962), tends to retain pollutants entering the system and delay dilution with receiving waters.

Many organisms continue to use the estuary for part or all of their lives. These organisms include commercially valuable shellfish and finfish and lower organisms such as polychaetes, phytoplankton and zooplankton that are essential to the estuarine food web. Many fish depend on the estuary as a nursery and critical stages of their life cycle occur in these waters, while others use it as a key migration route between fresh and seawater. At one time both shell- and fin-fish fisheries thrived in the estuary. Some, such as oyster, hard calm and soft calm shellfisheries collapsed or were reduced because of bacterial contamination. The commercial fin-fishery was relocated offshore due to legislation preventing fishing in the estuary. Today, outside of a few pound nets in the part of the estuary, most fin-fishing has been reduced to sport activity, although some clams are harvested for depuration or transfer to cleaner waters (MacKenzie, 1990). However the estuary is used for many recreational purposes including swimming, boating and sport fishing, which is now one of the biggest industries. Over the last century the quality of the estuary has degraded in part due to eutrophication, the process of nutrient enrichment through either natural or anthropogenic processes. Eutrophication disrupts the pre-existing natural balance of the system, resulting in phytoplankton blooms of both increased frequency and intensity in response to the over-enrichment. Noxious phytoplankton blooms are among the potential negative impacts, as are shifts to less desirable species of phytoplankton, diminished aesthetics (e.g. from brown tides) and changes in phytoplankton cell size. The latter can adversely affect the nutrition of organisms that have cell size-related food requirements (e.g. clams). Likewise, dense and accelerated phytoplankton blooms ultimately increase oxygen demand on the system leading to episodes of hypoxia. One indicator that the Hudson/Raritan Estuary is in an

advanced stage of eutrophication is the high concentration of chlorophyll found in Raritan Bay (Pearce, 1984). Phytoplankton increases are a definite manifestation of eutrophication or enrichment of New Jersey estuarine/coastal waters.

Phytoplankton populations in the Hudson/Raritan estuary, the Bight Apex and coastal waters of New Jersey are dominated by diatoms (> 20μm) such as Skeletonema costatum during the unstratified winter/spring months (Novermber-April) and by Nannochloris atomus (between 0.7-2.0 μm) dating the stratified summer/fall months (May-October). Diatoms typically dominate at all times in the offshore waters of the Bight (Bagheri, et al., 1999).

Dinoflagellate blooms off New Jersey are recurrent events during the summer. Since 1968, red tides have been associated with Olisthodiscus luteus (1976, 1978, 1979) and Prorocentrum micanas (1968, 1972, 1983). The bloom of Gyrodinium aureolum off the coast of southern New Jersey in 1984-85 was termed "green tide" because of its brilliant green color. Nannochloris atomus is another common species that causes green tides in New Jersey waters (DEP, 1986).

Brown tides are caused by the bloom of the Aureococcus anophageffereus. It had first appeared in Narragansett Bay, Rhode Island and Long Island's Peconic and Great South Bays as well as the New Jersey's Barnegat and South Bays. The brown tides occur in spring and summer months. They can kill shellfish and block sunlight to the underwater plants destroying the habitat of many marine resources. The brown tides have a major effect on shellfishing industry. In 1985, a brown tide in Peconic Bay reduced a $ 2 million scallop industry to a few thousand dollars. Research has shown that iron can stimulate growth of brown tides. Environmental factors such as a warmer climate,

increased salinity of water and lack of rainfall could contribute to the bloom formations, but the exact causes or cure are not known yet (NY SeaGrant, 1998).

To improve the quality of water and control the problem of excessive fertilization, regular monitoring of water quality is required. Currently there is no systematic management tool for operational monitoring and prediction of spreading of pollution for Hudson/Raritan Estuary. This research is aimed to utilize the data acquired by dedicated remote sensing flights in modeling of water quality parameters and thus better management of water resources.

CHAPTER 5

RESEARCH MATERIALS

5.1 Airborne Visible Infra Red/Imaging Spectrometer(AVIRIS) Data

Airborne Visible Infra Red Imaging Spectrometer (AVIRIS) is usually flown on the aircraft platform of a NASA ER-2 jet at approximately 20 km above sea level.

The AVIRIS instrument contains 224 different detectors, each with a wavelength sensitive range of approximately 10 nanometers (nm) (nominal width is 9.6 nm), allowing it to cover the entire range between 400 nm and 2500 nm. When the data from each detector is plotted on a graph, it yields a spectrum. Comparing the resulting spectrum with those of known substances reveals information about the composition of the area being viewed by the instrument. AVIRIS uses a scanning mirror to sweep back and forth ("whisk broom" fashion), producing 614 pixels for the 224 detectors each scan.

The AVIRIS is capable of measuring hydrologic optical properties at a level of detail unmatched by any existing satellite instrument. The instrument is composed of four spectrometers (A, B, C, and D). The A spectrometer records the data for the first 32 bands while the B, C and D spectrometers record 64 bands each. Because of band overlap between the four spectrometers, 210 discrete bands are available. The pixel size and swath width of the AVIRIS data depend on the altitude from which the data is collected. When collected by the ER-2 (20km above the ground), each pixel produced by the instrument covers an area approximately 20 meters square on the ground (with some overlap between pixels), thus yielding a ground swath about 11 kilometers wide. The ground data is recorded on board the instrument along with navigation and engineering data and the readings from the AVIRIS on-board calibrator (http://aviris.jpl.nasa.gov).

Figure 5.1 illustrates one means commonly employed to display AVIRIS data. In AVIRIS image, the data can be thought of as a "cube" of the dimensions lines × columns × bands.

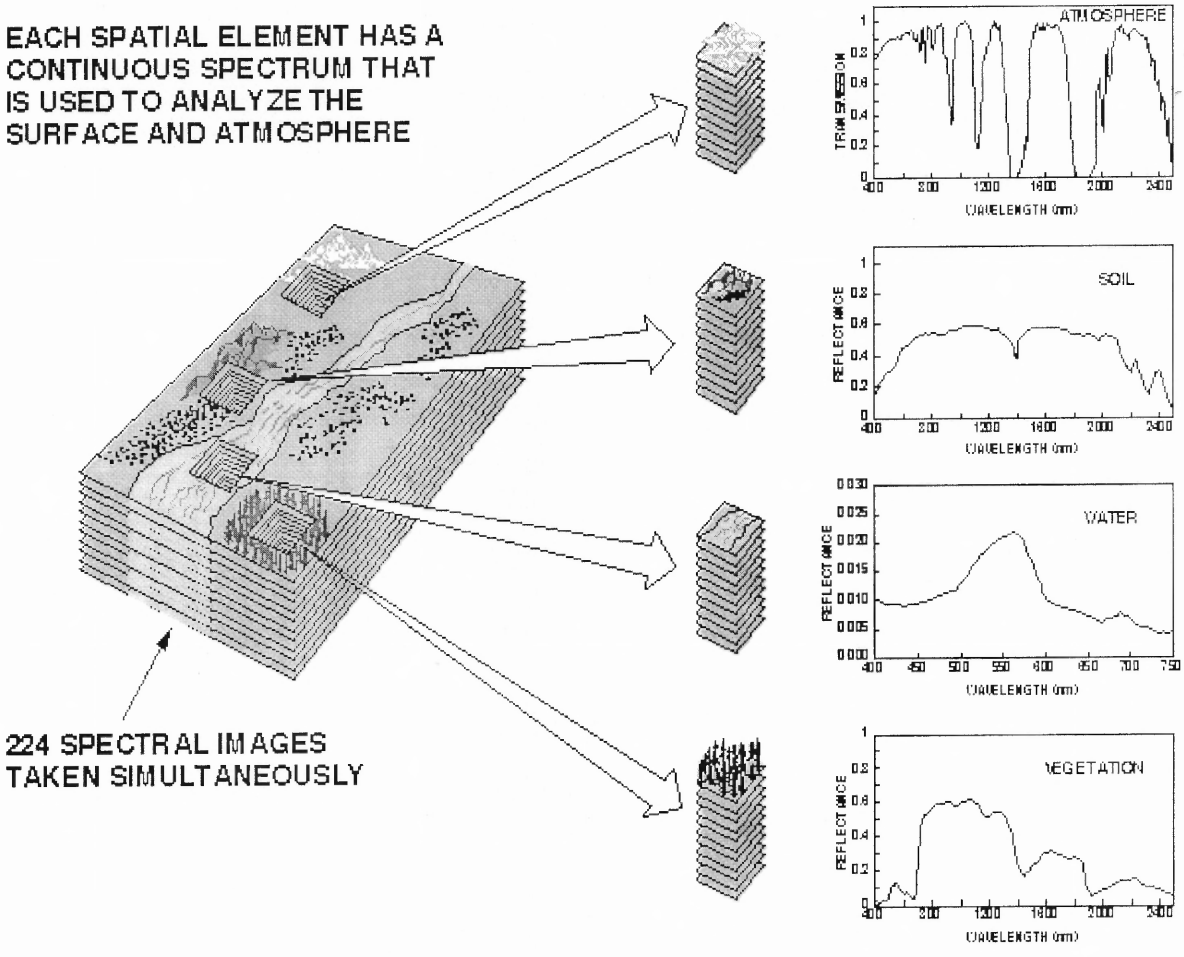

Figure 5.1 AVIRIS remote sensing concept
(http://aviris.jpl.nasa.gov /html)

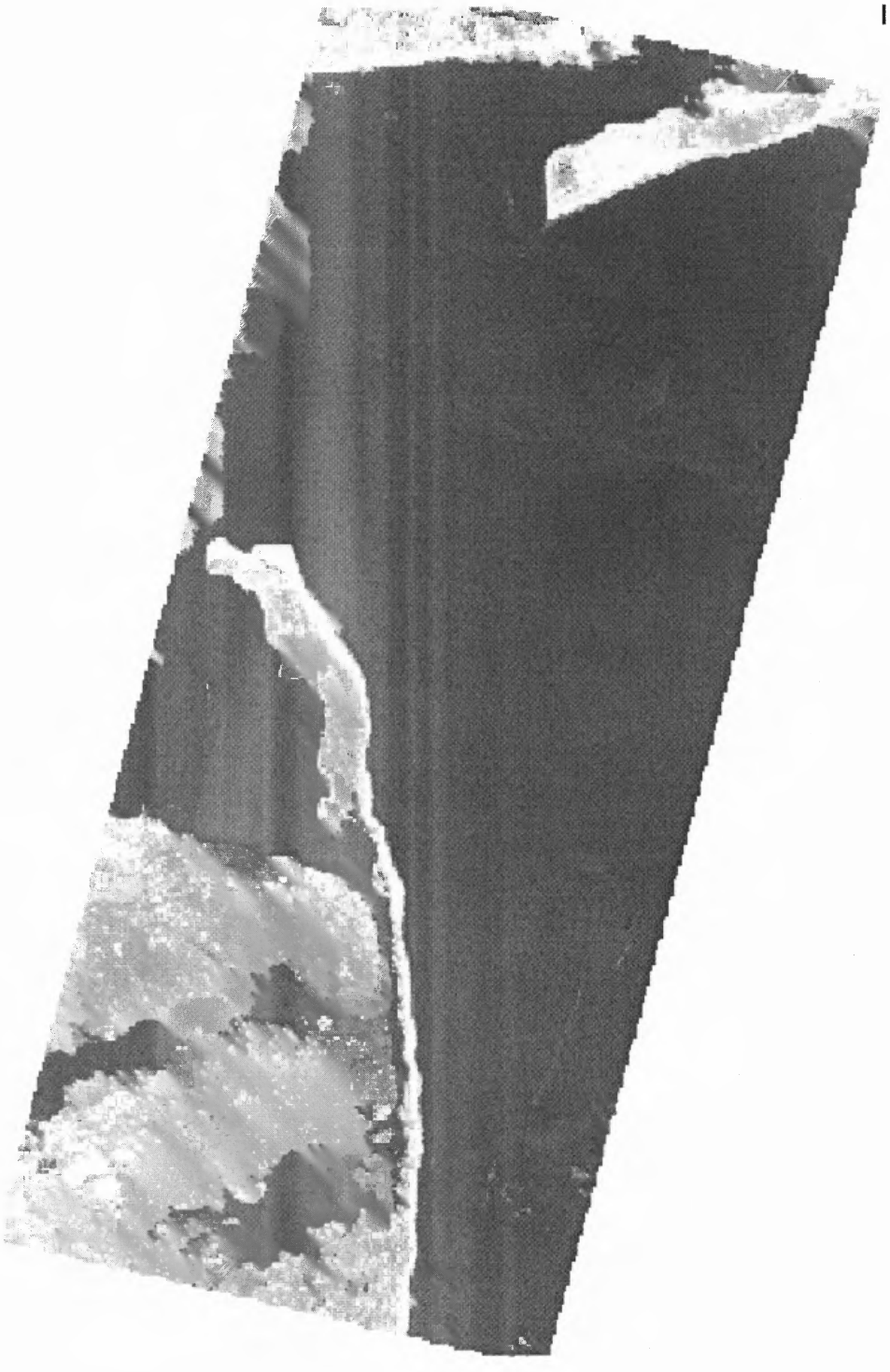

Figure 5.2 AVIRIS image acquired on 7/13/2001 over a transect of the study area

5.2 LIght Detecting And Ranging (LIDAR) Data

LIght Detecting And Ranging (LIDAR) uses the same principle as RADAR. The LIDAR instrument transmits light out to a target. The transmitted light interacts with and is changed by the target. Some of this light is reflected/scattered back to the instrument where it is stored. The change in the properties of the light enables some properties of the target to be determined.

The LIDAR data used in this research were acquired by NASA Airborne Oceangraphic Lidar (AOL3). The NASA AOL Fluorosensor is a laser fluorospectrometer which is carried onboard aircraft as small as twin engine planes. The Airborne Oceanographic Lidar Fluorosensor instrumentation acquires measurements of fluorescence from certain oceanic pigments. These include chlorophyll and phycoerythrin from marine phytoplankton and chromophoric dissolved organic matter (CDOM), from which a number of oceanographic surface water properties can be derived. The water-Raman backscatter is also acquired and is used to normalize the laser-induced fluorescence data for surface layer spatial differences in water attenuation properties. The AOL fluorosensor uses a pulse of laser light fired from the aircraft down into the ocean. This sensor transmits two laser wavelengths, one UV (355nm) and one green (532nm) to the ocean surface from the aircraft. These laser frequencies interact with the water molecules, causing a shift in the laser frequency. If biological organisms containing chlorophyll and/or phycoerythrin are present in the water, the 532nm laser light is absorbed, and reemitted as particular bands of fluorescence. A telescope onboard the aircraft collects the light from the plants, and electronic equipment converts the signal into numbers a computer can record. The AOL collects the laser-induced fluorescence

spectrum in a contiguous region covering the spectral band from 370 nm to 740 nm, for each laser pulse (http://aol.wff.nasa.gov).

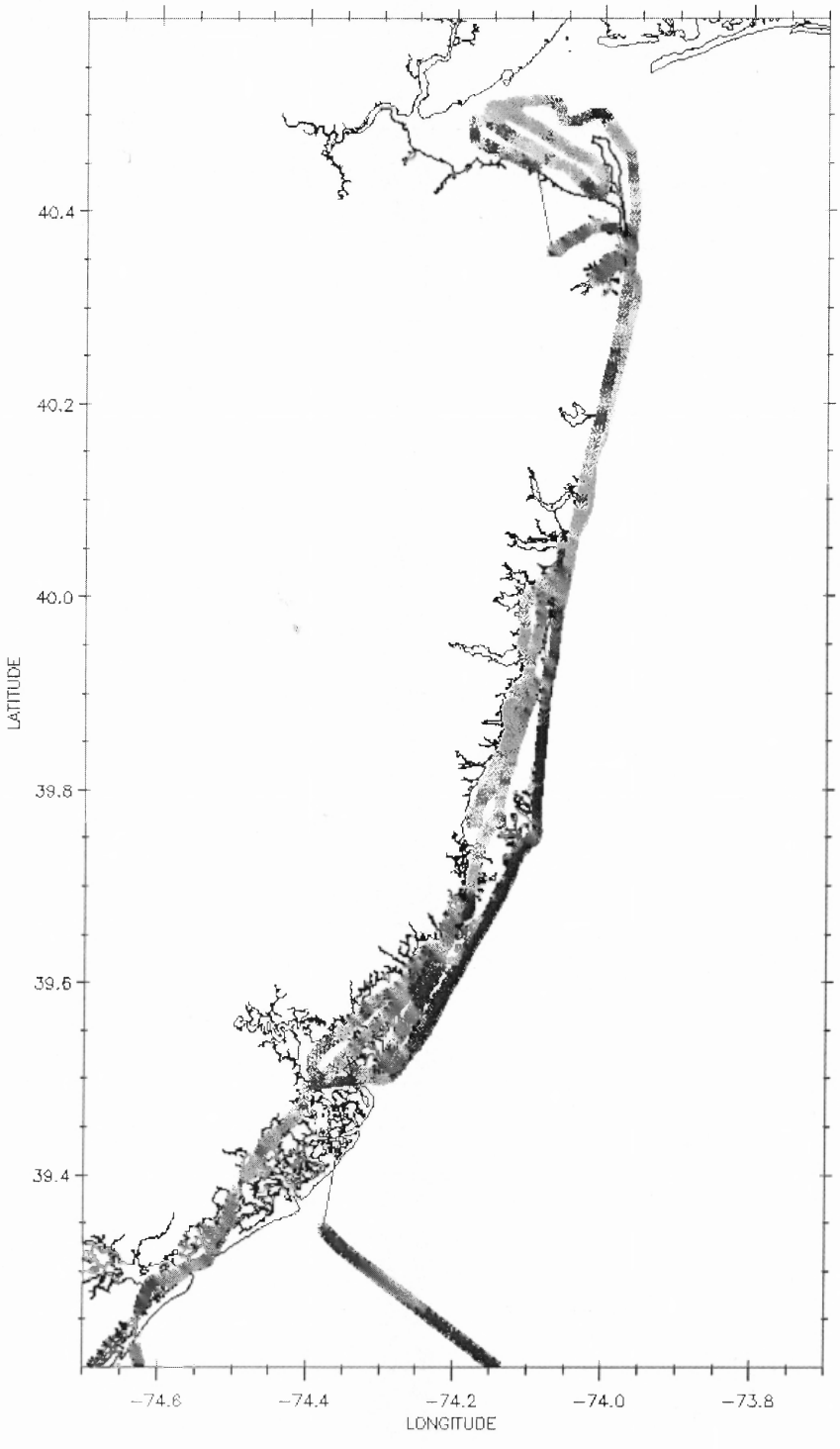

Figure 5.3 Map of the transects covered by AOL during 4/11/2002 data acquisition

5.3 Spectroradiometer (OL754) Data

The OL 754 Portable UV-Visible-NIR Spectroradiometers are a series of compact, portable, double monochromator based spectroradiometers capable of making highly accurate spectroradiometric measurements in the laboratory or in the field. Three optic heads are available for covering the wavelength range of 200 to 1600 nm. The OL 754's innovative design combines compact Visible-NIR (350-1100 nm) optimized double monochromators with a separate controller that houses all data acquisition and controls electronics. The system can be configured to make spectral measurements at wavelength resolutions from 1 nm to 10 nm for computation of normalized percentage reflectance curves. Fast and accurate spectroradiometric measurements can be made in the laboratory, or with the battery/dc power option, outside with total portability under demanding field conditions.

The instrument is designed with the largest possible port diameter to sphere size that is consistent with a good cosine response, hence maintaining high performance while minimizing self-shading effects. Measurements of upward and downward light fields will establish the relationship between inherent optical properties and the concentrations of water constituents within the water column. For the purpose of the research project supported by NSF (1998-2001), OL-754 data were collected in the study area during the course of project (1998-2001). The data measured on July 13, 2001 were used in model development for retrieval of water constituent concentrations.

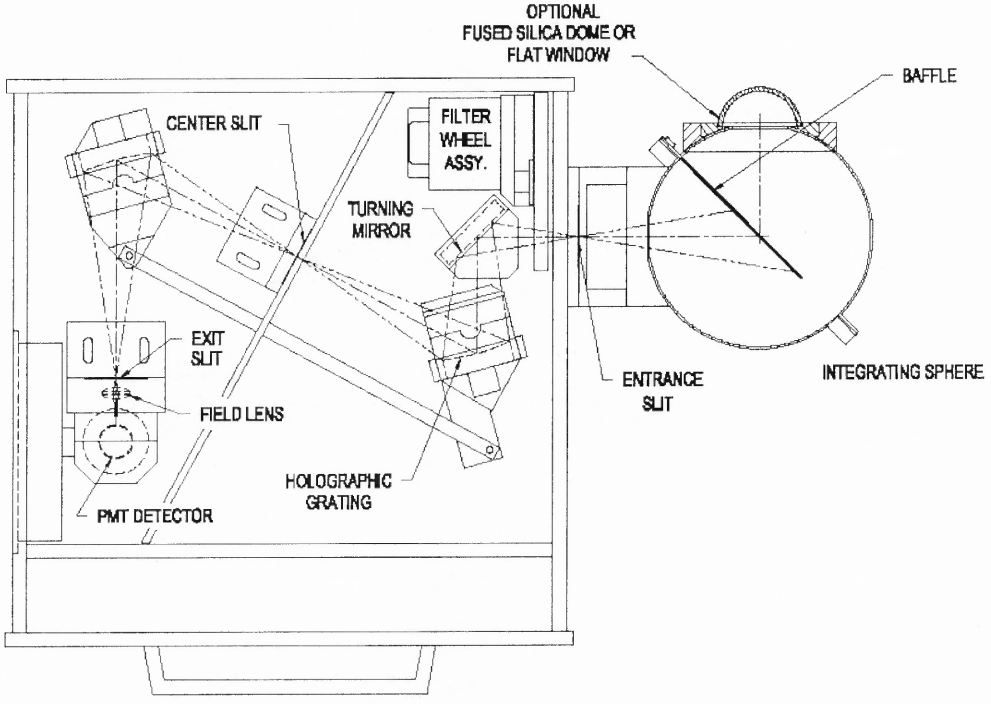

Figure 5.4 Configuration of the OL754-PMT Optics Head
(Optronic Laboratories, 1995)

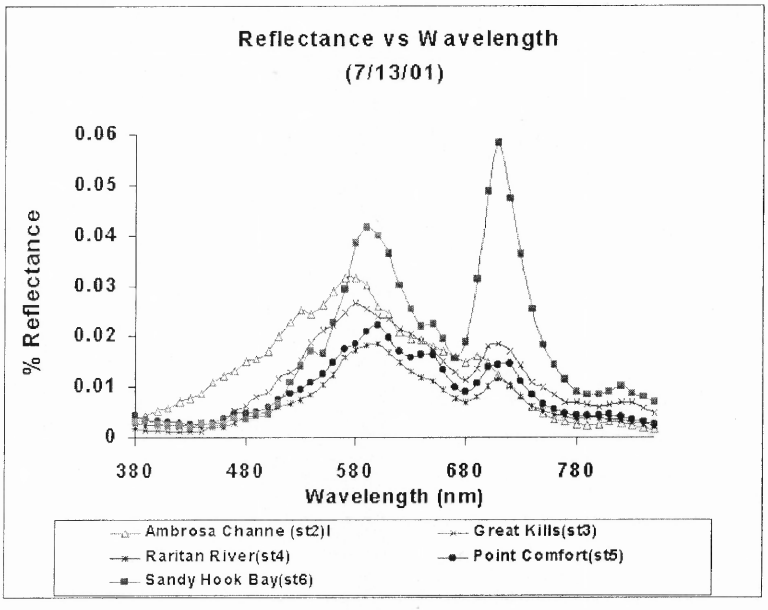

Figure 5.5 The reflectance spectra recorded by OL-754 at designated sampling stations

5.4 Shipboard Sampling Data

5.4.1 Optical Water Quality Concentration Measurements

Water samples were collected (0.2 to 0.5 m depth) from selected sample stations as marked in figure 4.1 for laboratory analysis. They were taken in 1-l bottles and placed in a cooler with melting ice before transport to the laboratory for analysis. Standard procedures as described by Rijkeboer et al. (1998) were used to determine the concentrations of total chlorophyll-a (TCHL) defined as the sum of CHL and phaeopigments (as indication of concentration of phytoplankton) and total suspended matter (TSM). The pigment concentration was determined according to the Dutch standard method NEN 6520 (1981). This method is based on the extraction of CHL pigments from the phytoplankton using hot ethanol (80%, at 75°C). The TCHL is then determined spectrophotometrically, using the extinction of the solvent at 665nm and 750nm. The phaeopigment concentration is determined similarly after acidification of the sample. All analyses were performed in duplicates. The TSM concentrations were determined according to the Dutch standard method NEN 6484 (1982). The samples were filtered over 0.45 mm Whatman GF/F filters with volumes ranging from 100 ml to 200 ml. The filters were dried at 80°C. Ignition loss was determined by ashing the filters with TSM at 550°C. The filters were flushed with 10 ml tap water to prevent overestimating the TSM concentration due to remaining salt left on the filter. Table 5.1 shows the concentration of WQP as sampled during 1999–2001, indicating that sampling did not coincide with any major phytoplankton bloom. Likewise, the TSM ranges were within

the expected values for the time of year when the measurements taken (Bagheri et al., 1999, 2000).

The samples were analyzed for their IOPs as well as the identification/ enumeration of the phytoplankton species. This was done to demonstrate the variety and composition of phytoplankton populations. The most abundant organisms identified were the Diatoms, Skeletonema sp. Also present in low counts were Flagellates, Eutreptia sp. and Prorocentrum minimum. The TCHL concentrations varied between 73mg m^{-3} and 6 mg m^{-3} indicating that the measurements did not coincide with any major outbreaks of phytoplankton blooms. Likewise, the TSM ranges (26-5 g m^{-3}) were within the expected values for the time of year when the measurements taken (Bagheri et al., 1999, 2000).

5.4.2 IOPs Measurements

The two main IOP are the spectral absorption and scattering. Absorption is mainly caused by organic particles and dissolved organic particles while scattering is mainly caused by inorganic particles. The spectral absorption causes a reduction in R(0-), and the spectral scattering causes an increase in R(0-). Spectral beam attenuation (c) and spectral absorption (a) were obtained using Ocean Optics-2000. The Ocean Optics-2000 is a modular spectrophotometric/spectroradiometric system relying on optical fibres and fore-optics to enable it to carry out a variety of optical measurements. (Note: use of Ocean Optics-2000 for measuring IOP is experimental and has not been referenced in the published literature.) From these measurements, the spectral scattering (b) was deduced via subtraction of spectral absorption from the spectral beam attenuation (b=c-a). The samples were filtered through a 0.45 mm Whatman GF/C glassfibre filter. Then the

coloured dissolved organic matter (CDOM) absorption was measured in a 10 cm cuvette against DI water. The CDOM absorption spectra were normalized at 440 nm, and the absorption at 440nm was taken as a measure of the concentration (Rijkeboer et al. 1998).

The seston (TSM) absorption spectra were measured using the filterpad method. After extraction of the ethanol-soluble pigments from the filter using approximately 5–10 ml hot (80°C) 80% ethanol, the absorption spectra of bleached seston were measured using the filterpad method. Phytoplankton absorption was calculated as the difference between seston absorption and bleached seston absorption. Scattering was calculated as the difference of the beam attenuation and the total absorption (seston + CDOM). TSM specific scattering and absorption were calculated by dividing the total scattering and total (seston) absorption by the simultaneous measurement of TSM concentrations. TCHL specific phytoplankton absorption was calculated by dividing the phytoplankton absorption with the TCHL concentration. These data as shown in table 5.1 and discussed below were used to simulate subsurface irradiance reflectance (or water leaving radiance) and to estimate the concentrations of various WQP (Bagheri et al., 1999, 2000).

Table 5.1 Sample Locations and Water Conditions As Recorded on Board R/V Walford and Blue Sea

Date	St	Location	Lat	Long	S.D.(m)	TCHL (mg m^{-3})	TSM (gm^{-3})
8/14/1999	1	Comptons/PewsCreek	40.45	74.08	1.3	15	6
	2	Keyport Harbor	40.47	74.19	0.8	32	26
	3	Traid Bridge	40.50	74.28	0.9	17	13
	4	Crookes Pt State Isl.	40.54	74.14	0.6	37	15
	5	Coney Isl. Pt.	40.57	74.02	1.8	6	11
	6	Sandy Hook Tip	40.49	74.02	0.9	22	12
	7	Shrewsbury River	40.38	73.98	0.5	48	21
5/15/2000	1	Buoy 2	40.42	74.01	1.25	31	8
	2	Atlantic Highlands	40.47	74.03	1.25	46	11
	3	Horseshoe Cove	40.59	74.03	1.37	22	7
7/13/2001	1	Tip of Sandy Hook	40.55	73.93	1.3	38	23
	2	Ambrosa Channel	40.54	74.02	0.8	17	8
	3	Great Kills	40.52	74.13	0.9	36	23
	4	Raritan River	40.49	74.24	0.6	32	21
	5	Point Comfort	40.46	74.14	1.8	73	5
	6	Sandy Hook Bay	40.42	74.03	0.9	38	8

CHAPTER 6

RESEARCH METHODS

Since no single method is yet available to derive concentrations from all optically active water quality parameters, two complementary inversion techniques are used for retrieval of constituent concentrations. This chapter covers the establishment of bio-optical model for the study area and "Inverse Modeling" followed by "Statistical Method" for validation.

6.1 Calibration of Bio-optical Model for Hudson/Raritan Estuary

To link the WQP and IOP the Gordon's 1975 optical water quality model, Equation 3.2 $R(0_-) = r \cdot (\frac{b_b}{a + b_b})$, was calibrated for measurements of optical water constituent concentrations and IOP in the Hudson/Raritan Estuarine waters (Bagheri et al., 2001).

To establish values for r and b_b for a specific location, knowledge of the volume scattering function is required. Vos et al. (1998) demonstrated that a practical solution for measurement of the volume scattering function is to estimate r by matching modeled R(0-) to measured R(0-) values. According to Kirk (1991), the factor r for a large number of water bodies measured varied between 0.34 and 0.39 depending on the solar zenith angle and atmospheric conditions. Dekker et al. (1997) reported that the r values ranged from 0.12 to 0.56 with an average of 0.29 for four inland water types in the Netherlands. These water types were: shallow eutrophic lakes, shallow mesotrophic lakes, deep lakes, and river and canals. Bagheri (1999, 2000, 2001, 2002) calibrated this optical water quality model (3.2) in related research for measurements of optical water constituent

concentrations and IOP. The IOP were calculated using Equation 3.3 $a = a_w + a^*_{TSM} \cdot TSM + a^*_{ph} \cdot CHL + a^*_{CDOM} \cdot CDOM_{440}$ and Equation 3.4 $b_b = 0.5 \cdot b_w + b^*_{bTSM} \cdot TSM$. Based on the field data obtained in the estuary and calculations made by fitting measured R(0-) spectra to measured IOP (see Figure 6.1), in the Hudson/Raritan Estuary the value for factor r was established and varied between 0.28–0.34.

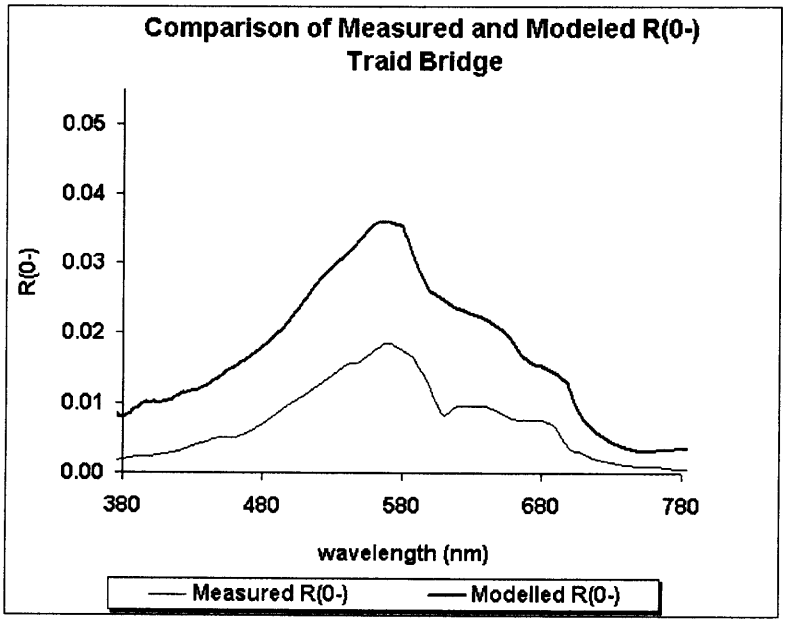

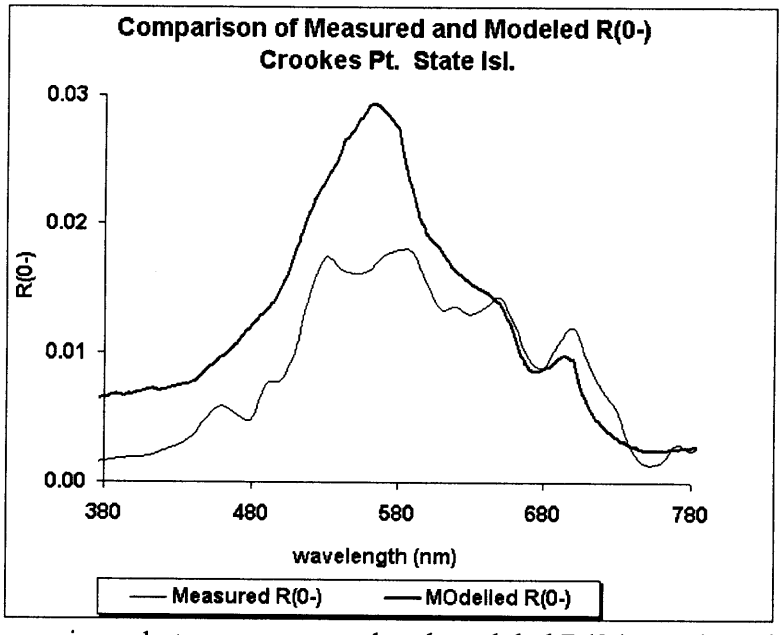

Figure 6.1 Comparisons between measured and modeled R(0-) at selected stations

6.2 Inverse Modeling

In principle, the Matrix Inversion Model (MIM) accounts for the mutual influence of the constituents. MIM provides a generic framework for interpreting spectral reflectance recorded with any band set and is thus very suitable for imaging spectrometry data (Hoogenboom et al., 1998). Two matrix inversion methods used for the retrieval of constituent concentrations from the subsurface irradiance reflectance are described as follows.

6.2.1 Matrix Inversion Model (Hoge, et al., 1996)

Hoge et al. developed a matrix inversion model based on Gordon's 1988 bio-optical model described in chapter 3. Gordon's 1988 model (Equation 3.5, $L_w(\lambda) = F_0 t(\theta_0)\cos(\theta_0) M \, R/Q$) can be solved in terms of total absorption coefficient a and total backscattering coefficient b_b: $a + b_b(1-1/X) = 0$, where X is given by the solution of Equation (3.6), $R/Q = (l_1 X + l_2 X^2)$. Next, define $v = (1-1/X)$ and separate the seawater absorption and seawater backscattering contributions from the total constituent absorption and total constituent backscattering,

$$a_t + b_{bt} v = -(a_w + b_{bw} v) \tag{6.1}$$

Substituting Equation (2.1) for the absorption of all constituents in (6.1) for wavelengths λ_i, where i=1, 2, 3, the equation describing the IOPs is:

$$a_{ph}(\lambda_i) + a_d(\lambda_i) + b_{bt}(\lambda_i) \cdot v(\lambda_i) = h(\lambda_i) \tag{6.2}$$

where, $h(\lambda_i)$ is defined as the right side of (6.1) that contains the column matrix, or vector, of hydrosphere constants (seawater absorption and backscattering) and oceanic

water-leaving radiances. Equation (6.2) contains three unknowns a_{ph}, a_d, and b_{bt} for each spectral radiance measurement. Additional equations are provided by IOP spectral models for these unknowns as follows:

$$b_{bt}(\lambda_i) = b_{bt}(\lambda_b)\left(\lambda_b / \lambda_i\right)^n \tag{6.3}$$

where n is total constitute backscattering coefficient.

The above equation is used to describe the total constituent backscattering coefficient $b_{bt}(\lambda_i)$ at any wavelength λ_i relative to the total constituent backscattering at a reference wavelength λ_b.

Furthermore,

$$a_d(\lambda_i) = a_d(\lambda_d)\exp[-S(\lambda_i - \lambda_d)] \tag{6.4}$$

is a good representation of the spectral absorption coefficient of CDOM at any wavelength λ_i relative to the CDOM absorption coefficient at an arbitrary reference wavelength λ_d. S is the spectral slope for CDOM and the reference wavelength λ_d does not need to coincide with the sensor observational bands (Bricaud et al., 1981; Hoge et al., 1993).

Finally, a single Gaussian is used to represent the phytoplankton absorption coefficient in the chosen spectral regions (Hoepffner and Sathyendranath, 1993). For more complex analytical studies, several Gaussians can be used to more accurately represent the phytoplankton absorption including chlorophylls (Hoge et al., 1996). Thus

$$a_{ph}(\lambda_i) = a_{ph}(\lambda_g)\exp[(\lambda_i - \lambda_d)^2 / -2g^2] \tag{6.5}$$

where g is a parameter that defines the spectral width of the Gaussian about the peak wavelength λ_g. The Gaussian peak does not need to be located precisely coincident with

the phytoplankton pigment absorption peak as long as the spectral width parameter g permits accurate representation of the relative specific absorption coefficient in all three sensor observational bands.

The substitution of (6.3), (6.4) and (6.5) into (6.2) yields:

$$a_{ph}(\lambda_g)\exp[(\lambda_i-\lambda_d)^2/-2g^2]+a_d(\lambda_d)\exp[-S(\lambda_i-\lambda_d)] \\ +v(\lambda_i)b_{bt}(\lambda_b)(\lambda_b/\lambda_i)^n=h(\lambda_i) \tag{6.6a}$$

Equation (6.6a) contains only three unknowns, $a_{ph}(\lambda_g), a_d(\lambda_d)$, and $b_{bt}(\lambda_b)$ at any wavelengths λ_i. Thus a consistent solution can be obtained using only three sensor wavelengths λ_1, λ_2, and λ_3. The inversion matrices are easily obtained by sequentially writing (6.6a) for λ_1, λ_2, and λ_3. Essentially, the three observational sensor wavelengths at λ_1, λ_2, and λ_3 enumerate or label the rows of the matrices, while the three constituents at their reference wavelengths $a_{ph}(\lambda_g), a_d(\lambda_d)$, and $b_{bt}(\lambda_b)$ label the columns of the explicit matrix arrangement of (6.6a) so that

$$\begin{bmatrix} e^{[(\lambda_1-\lambda_g)^2/-2g^2]} & e^{[-S(\lambda_1-\lambda_d)]} & (\lambda_b/\lambda_1)^n v(\lambda_1) \\ e^{[(\lambda_2-\lambda_g)^2/-2g^2]} & e^{[-S(\lambda_2-\lambda_d)]} & (\lambda_b/\lambda_2)^n v(\lambda_2) \\ e^{[(\lambda_3-\lambda_g)^2/-2g^2]} & e^{[-S(\lambda_3-\lambda_d)]} & (\lambda_b/\lambda_3)^n v(\lambda_3) \end{bmatrix} \cdot \begin{bmatrix} a_{ph}(\lambda_g) \\ a_d(\lambda_d) \\ b_{bt}(\lambda_b) \end{bmatrix} = \begin{bmatrix} h(\lambda_1) \\ h(\lambda_2) \\ h(\lambda_3) \end{bmatrix} \tag{6.6b}$$

The oceanic state vector of unknown IOPs at their reference wavelengths, $\mathbf{p}=\left[a_{ph}(\lambda_g),\ a_d(\lambda_d)\ \ b_{bt}(\lambda_b)\right]^T$, where T denotes the transpose, is the solution of a matrix equation of the form

$$D \cdot p = h \tag{6.7}$$

where **D** is the data and model matrix and **h** is the vector of seawater absorption and backscattering hydrospheric constants and radiance data. It is important to emphasize that

the D matrix must be inverted for every pixel or oceanic radiance/reflectance spectrum since it contains radiance data in addition to model parameters. Equation (6.7) is comparable to the well-known linear matrix equation $A \cdot x = b$ whose solutions have been extensively studied. The direct solution to (6.7) is represented by

$$p = D^{-1} \cdot h \tag{6.8}$$

D^{-1} denotes the inverse of the data and model matrix D.

According to Hoge, the above model has not yet been applied to any actual airborne and satellite-derived water-leaving radiance data for retrieval IOPs (Hoge et al., 1996). In this study, Hoge's model with minor modifications is applied to airborne AVIRIS reflectance data and laser-induced fluorescence data.

In Hoge's model (6.6b), n is the total constitute backscattering (TCB) coefficient which is hard to measure as explained in chapter 2. For nonabsorbing backscatterers such as coccoliths, Gordon et al. (1988) used a n >1. Lee et al. (1994) suggested that the exponent can vary from 0 to 2.4. Maffione et al.'s (1995) field measurements showed that the spectral backscattering exponent can vary from 2.0 to 4.1. Hoge et al. (1995) used a particulate backscattering model with n=1.5 during retrieval of the CDOM absorption coefficient.

However, Hoge's TCB coefficient is not appropriate for this research and there is a serious bias between the measured and retrieved absorptions (Figure 6.2). Thus, in this research, a modified n needs to be chosen for Hudson/Raritan Estuary water using the least square algorithm to get a better retrieval. Similarly, the CDOM spectral slopes - s, and phytoplankton Gaussian model spectral width - g, should be modified based on in situ measurements.

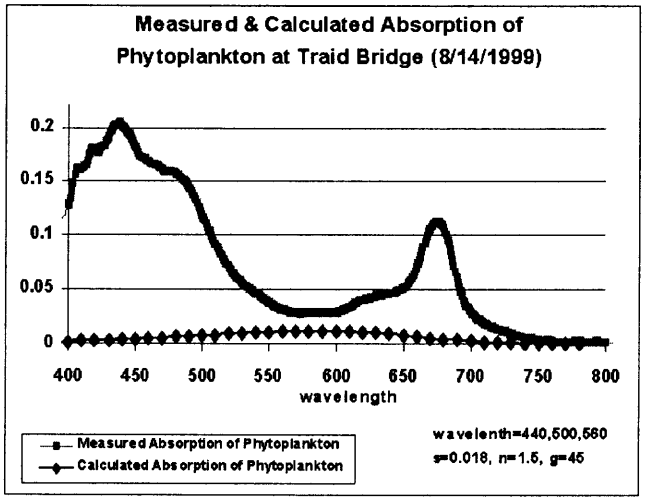

Figure 6.2 Measured and Retrieved Phytoplankton absorptions at Traid Bridge in 1999 using Hoge's model

It is clear that the matrix inversion can be extended to any number of constituents as long as accurate IOP models can be found to satisfactorily represent the spectral absorption and backscattering of each band (note: sufficient sensor bands are needed in the observational data to yield a solution). However, if the columns or rows of **D** in equation (6.7) are linear dependent, then columns (or rows) degeneracy occurs, the determinant vanishes (det **D** = 0), and **D** is singular. In order to avoid the singularity of **D**, in this research, **D** is replaced with a data and model matrix G, which includes not only three bands but all thirty-six bands of the spectra sensitive to optical water quality parameters covering the range of 400-750nm (Bidigare et al., 1988; Hoogenboom et al., 1998). Thus, (6.6b) becomes

$$\begin{bmatrix} e^{[(\lambda_1-\lambda_g)^2/-2g^2]} & e^{[-S(\lambda_1-\lambda_d)]} & (\lambda_b/\lambda_1)^n \nu(\lambda_1) \\ e^{[(\lambda_2-\lambda_g)^2/-2g^2]} & e^{[-S(\lambda_2-\lambda_d)]} & (\lambda_b/\lambda_2)^n \nu(\lambda_2) \\ \cdots & \cdots & \cdots \\ e^{[(\lambda_{36}-\lambda_g)^2/-2g^2]} & e^{[-S(\lambda_{36}-\lambda_d)]} & (\lambda_b/\lambda_{36})^n \nu(\lambda_{36}) \end{bmatrix} \cdot \begin{bmatrix} a_{ph}(\lambda_g) \\ a_d(\lambda_d) \\ b_{bt}(\lambda_b) \end{bmatrix} = \begin{bmatrix} h(\lambda_1) \\ h(\lambda_2) \\ \cdots \\ h(\lambda_{36}) \end{bmatrix} \tag{6.9}$$

and $G \cdot p = h$.

To solve the overdetermined matrix system (Equation 6.9), one commonly used measure of the misfit is the 2–norm of the residual. A model that minimizes the 2–norm of the residual is called a least–squares (LS) solution. In addition to linear least-squares, the singular value decomposition (SVD) method can be used to solve the above system. SVD method is an excellent analytical tool and allows a quantitative evaluation of singularities. However, the SVD solutions may become extremely unstable when one or more of the singular values is small. In order to make the solution more stable, the Tikhonov regularization technique can be used. The Tikhonov method effectively gives larger weight to larger singular values in the SVD solution and gives lower weight to small singular values. In this study, all the three methods were applied for validation (See Appendix B in reference to LS, SVD and Tikhonov methods). As shown in Figure 6.3, results from the three methods are very similar with the SVD method yielding a better output. Note that in the modified version of Hoge's linear matrix inversion model, the following values were assigned: $n = 1.8$, $s = 0.03$ and $g = 30$.

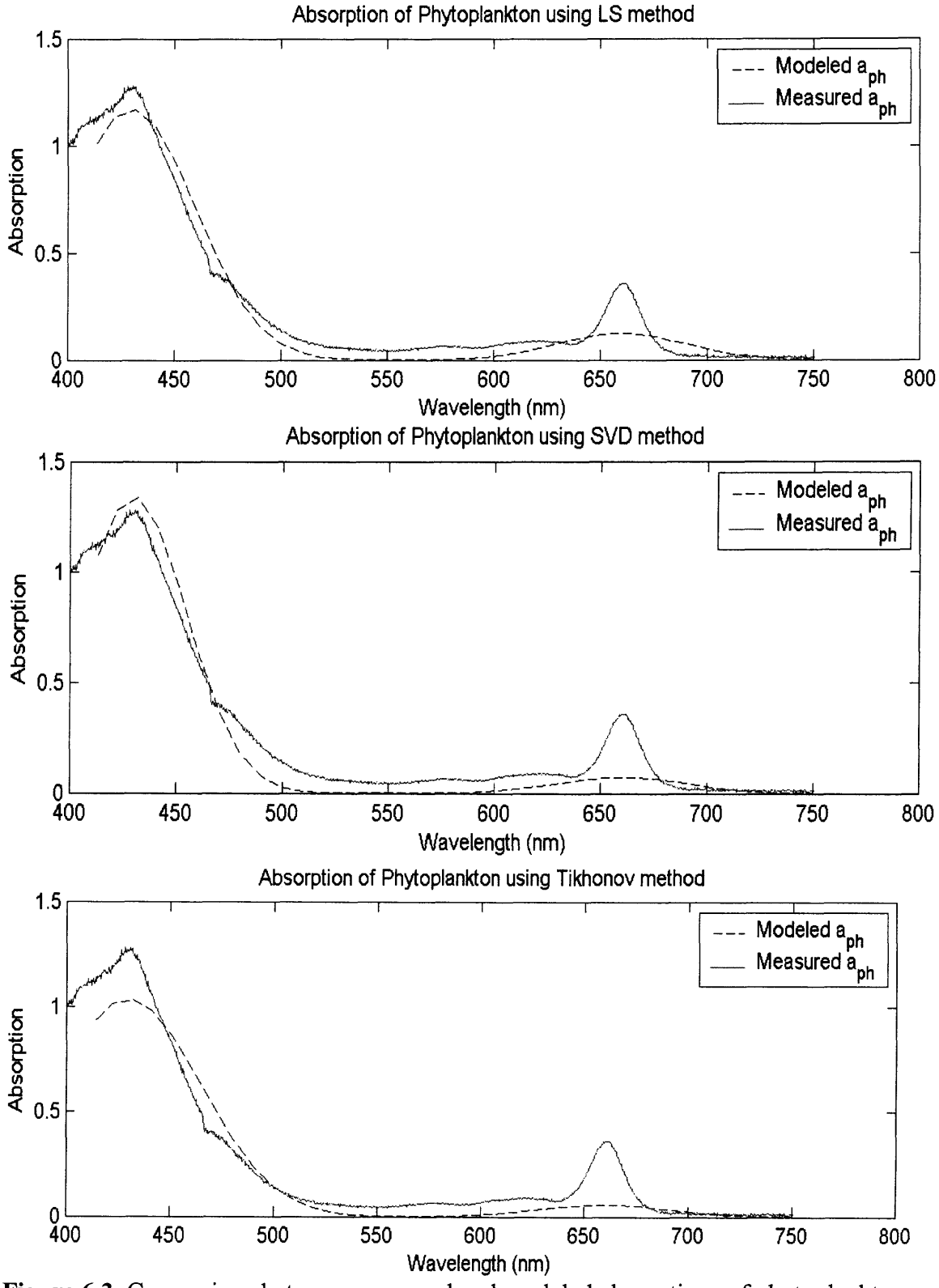

Figure 6.3 Comparison between measured and modeled absorptions of phytoplankton and CDOM using LS, SVD and Tikhonov methods

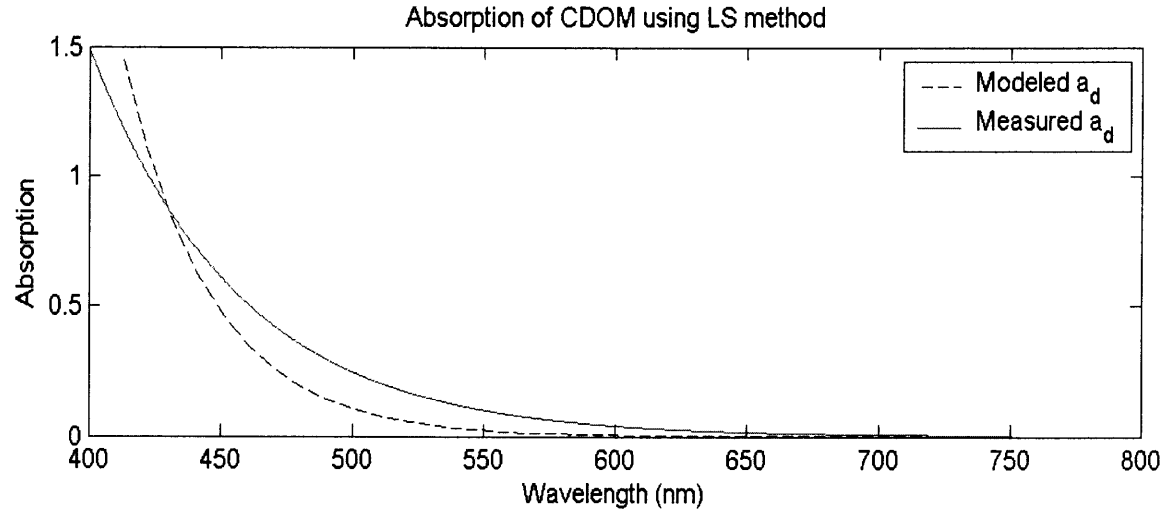

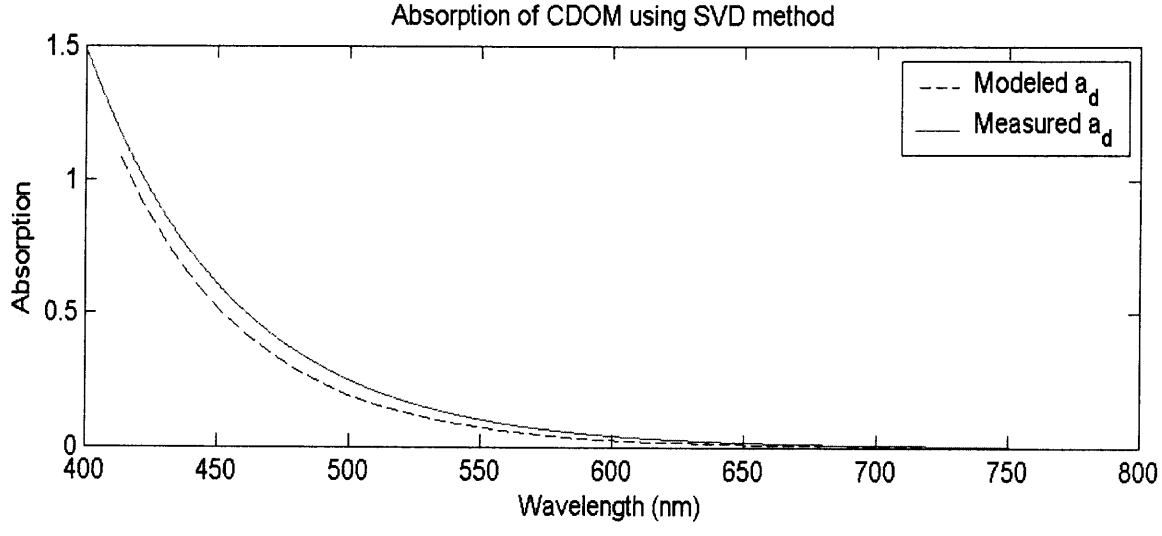

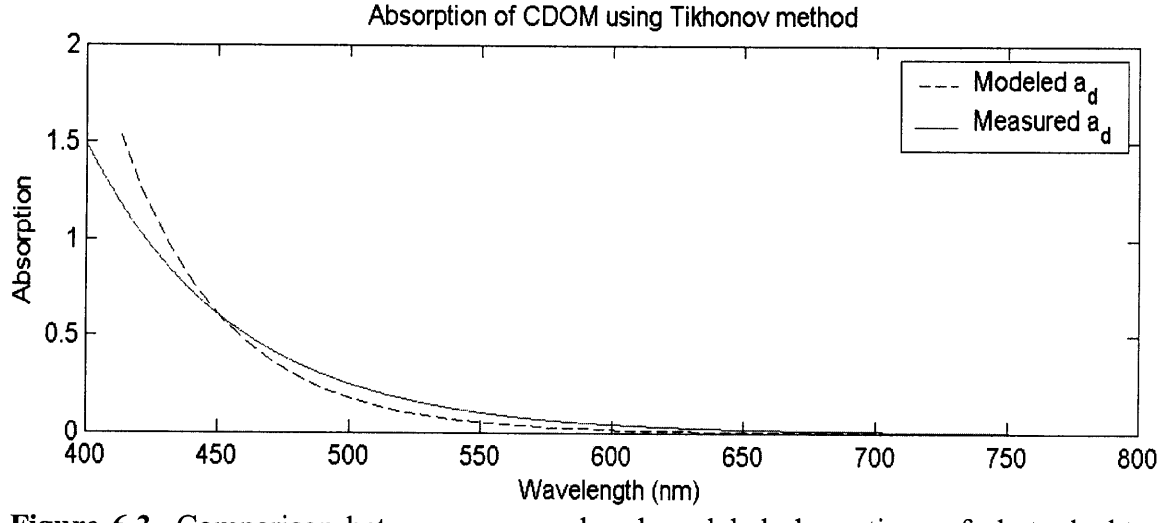

Figure 6.3 Comparison between measured and modeled absorptions of phytoplankton and CDOM using LS, SVD and Tikhonov methods (continued)

Using $a_i^* = \frac{a}{C_i}$, the concentrations of CHL_a and CDOM can be retrieved from their corresponding absorption values. Table 6.1 lists the calculated concentrations versus measured concentrations for selected stations sampled in July, 2001.

Hoge's model is also validated by applying the fluorescence-based algorithm to LIDAR data acquired on 4/5/2001 for retrieval of CHL_a concentration (figure 6.4).

As described in chapter 3, Poole et al. (1982) obtained a linear relationship between normalized laser-induced fluorescence and in situ CHL_a concentration: $C = k \cdot \frac{f}{r}$, where, C is the CHL_a concentration; k, the coefficient of the linear relationship between normalized laser-induced fluorescence; and CHL_a concentration and $\frac{f}{r}$, laser-induced fluorescence normalized by the 650nm water Raman signal. Table 6.1 lists the measured and modeled concentration values as computed by the above fluorescence-based algorithm and compared with the field samples.

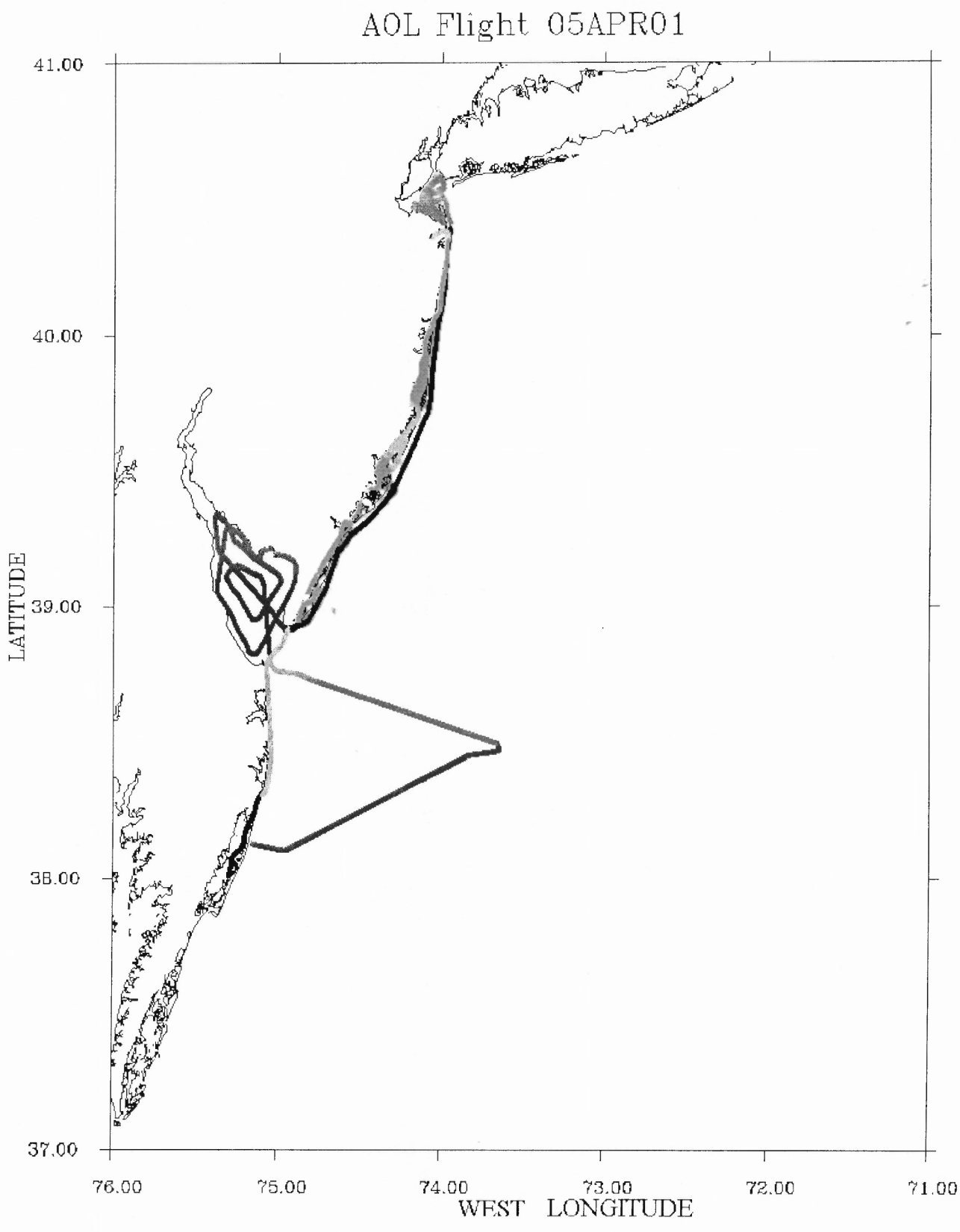

Figure 6.4 Map of the transects covered by AOL during 4/5/2001 data acquisition

6.2.2 Matrix Inversion Model (Hoogenboom et al., 1998)

Hoogenboom (et al. 1998) developed an inverse model based on Gordon's 1975 bio-optical model (Equation 3.2):

$$R(0-) = r \cdot (\frac{b_b}{a + b_b}) \tag{3.2}$$

where a = the total absorption coefficient

b_b = the total backscattering coefficient

r is a multiplication factor that depends on the apparent optical properties of the light field. For the Hudson/Raritan Estuary, Bagheri et al. (1999, 2000, 2001, 2002) calibrated the values for factor r which varied between 0.28–0.34 for the stations sampled within the estuary.

Hoogenboom substituted Equation 3.2, $R(0-) = r \cdot (\frac{b_b}{a + b_b})$, into Equation 3.3, $a = a_w + a^*_{TSM} \cdot TSM + a^*_{ph} \cdot CHL + a^*_{CDOM} \cdot CDOM_{440}$, and Equation 3.4, $b_b = 0.5 \cdot b_w + b^*_{bTSM} \cdot TSM$, by taking the correlation between TSM and CHL into account. Accordingly, the total TSM ($TSM_{tot} = TSM_{ph} + TSM_{ss}$) values include the part of the dry weight determined by the biomass of phytoplankton which is correlated to CHL concentration. The correlation coefficient can vary between 0.02 and 0.1 for freshwater algae (Gons et al. 1992). An average value of 0.07 (TSM_{ph}~0.07CHL) is used here based on Buiteveld (1990):

$$[a^*_{ph} + 0.07a^*_{TSM} + 0.07b^*_{b,TSM} X]CHL + [a^*_{TSM} + b^*_{b,TSM} X]TSM_{ss} = -a_w - a^*_{CDOM} CDOM_{440} - b_{bw} X \tag{6.10}$$

where,

$X = 1 - \frac{f}{R(0-)}$, and $TSM_{ss} = TSM_{tot} - TSM_{ph} = TSM_{tot} - 0.07 \cdot CHL$

Evaluating Equation (6.10) for every wavelength of interest yields a set of equations, conveniently put in one matrix equation:

$$Y = \begin{pmatrix} A_{m1} \\ A_{m2} \end{pmatrix} \begin{pmatrix} CHL \\ DW_{tr} \end{pmatrix} \tag{6.11}$$

where,

$$A_{m1} = a^*_{pigm}(\lambda_m) + 0.07a^*_{dw}(\lambda_m) + 0.07b^*_{bdw}(\lambda_m)(1 - \frac{f}{R(\lambda_m)})$$

$$A_{m2} = a^*_{dw}(\lambda_m) + b^*_{bdw}(\lambda_m)(1 - \frac{f}{R(\lambda_m)})$$

$$y_m = -a_w(\lambda_m) - a^*_g(\lambda_m)g_{440} - b_{dw}(\lambda_m)(1 - \frac{f}{R(\lambda_m)})$$

In this basic case of matrix inversion one can solve this system (6.11) for two concentrations from two spectral bands. In that case a two-by-two matrix has to be inverted analytically yielding the following expressions for the concentrations:

$$CHL = \frac{A_{22}y_1 - A_{12}y_2}{A_{11}A_{22} - A_{12}A_{21}} \text{ and} \tag{6.12}$$

$$TSM_{ss} = \frac{-A_{21}y_1 + A_{11}y_2}{A_{11}A_{22} - A_{12}A_{21}}$$

In Hoogenboom's model (6.11), two equations were created to solve two unknowns, CHL and TSM concentrations. Since relationship (6.10) holds for each band, as a result, any two bands can be theoretically selected and put into the matrix system (6.11). Hoogenboom applied reflectance data at 677nm and 705nm acquired by Casi over the Lake Braassem, the Netherlands. However, results from this model (6.11) using those two bands of AVIRIS over the study area are seriously biased with measured data. Thus,

the two bands selected for input should be based on the characteristics of the AVIRIS data.

It should be noted that Hoge's model (model #1) was based on Gordon's 1988 bio-optical model. It retrieves IOPs first, and uses the relationship between absorption and specific absorption ($a_i^* = \frac{a}{C_i}$) for retrieval of water constituent concentrations while the Hoogenboom's model (model #2) was based on Gordon's 1975 bio-optical model from which the retrieval of water constituent concentrations can directly be obtained. Comparing Hoge's model (6.6b) with Hoogenboom's model (6.11), the latter has few input parameters making it a less complicated model to use.

Table 6.1 lists the measured and modeled concentration values as computed by two MIM models cited before and compared with the field samples. There are reasonable matches between the measured and calculated concentrations using model #1 and #2.

Table 6.1 Retrieval of TCHL and TSM Concentrations

Stataions	Measured TCHL (mg m^{-3})	Modeled TCHL(#1) (mg m^{-3})	Modeled TCHL(#2) (mg m^{-3})	Modeled TCHL(#3) (mg m^{-3})	Measured TSM (g m^{-3})	Modeled TSM(#3) (g m^{-3})
Traid Bridge	**17**	15	24	9	**13**	19
Crookes Pt Staten Isl.	**37**	22	40	44	**16**	8
Coney Isl. Pt.	**15**	12	17	7	**6**	22
Sandy Hook Tip	**32**	17	39	12	**26**	19

Note:

Model 1------Hoge's model (AVIRIS data)
Model 2------Fluorescence-based algorithm (LIDAR data)
Model 3------Hoogenboom's model (AVIRIS data)

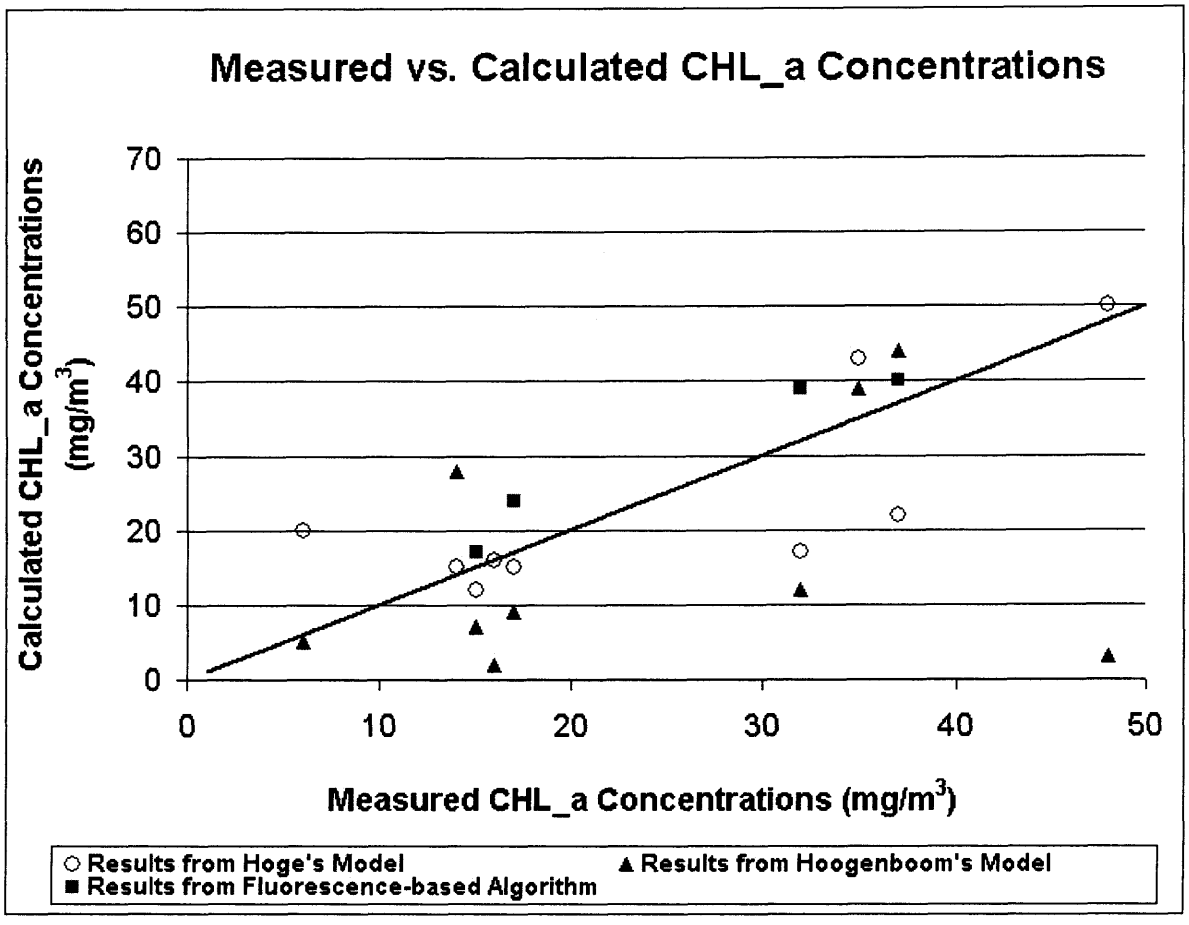

Figure 6.5 Comparison of the retrieved CHL_a concentrations using absorption-based and fluorescence-based algorithms

As shown in Table 6.1, the results from Hoge's model applied to LIDAR data are closer to measured values than those from AVIRIS data. It is worth mentioning that the AVIRIS uses the absorption-based principles, and LIDAR uses fluorescence-based principles. The fluorescence-based algorithm is not likely to be influenced by CDOM absorption since the CDOM absorption in the red part of the spectrum is negligible. Although the retrieved CHL_a concentrations from Hoogenboom's model are not as good as those from Hoge's model, the algorithm is applicable to data for retrieval of TSM concentrations. Table 6.1 lists the computed values of TSM as compared with measured values for selected stations within the study area using the two complementary models.

6.3 Statistical Method

Regression is a statistical technique used to determine the equation of the line or curve which minimizes the deviations between the observed data and the regression equation values (Blank, 1980). Regression analysis between *in-situ* and remotely-derived values are widely used to assess the accuracy of the MIM-generated water constituent concentrations (Hoge et al., 1996, 2001).

In this study, a regression analysis is performed on the AVIRIS data. This regression analysis is an *all-possible-regressions procedure*, which calls for considering all possible subsets of the pool of potential independent variables and detailed identification of a few "good" subsets according to some criterion. The independent variables are the reflectance data from different AVIRIS bands or band ratios at different sampling stations, while dependent variables are the concentrations of CHL_a, and TSM. The ultimate goal is to obtain comparable results when using the MIM on the same data.

Figure 6.6 presents the strategy for the building of the regression model. This strategy involves four phases:

1. Data collection and preparation
2. Reduction of independent variables (bands reflectance)
3. Model refinement and selection
4. Model validation

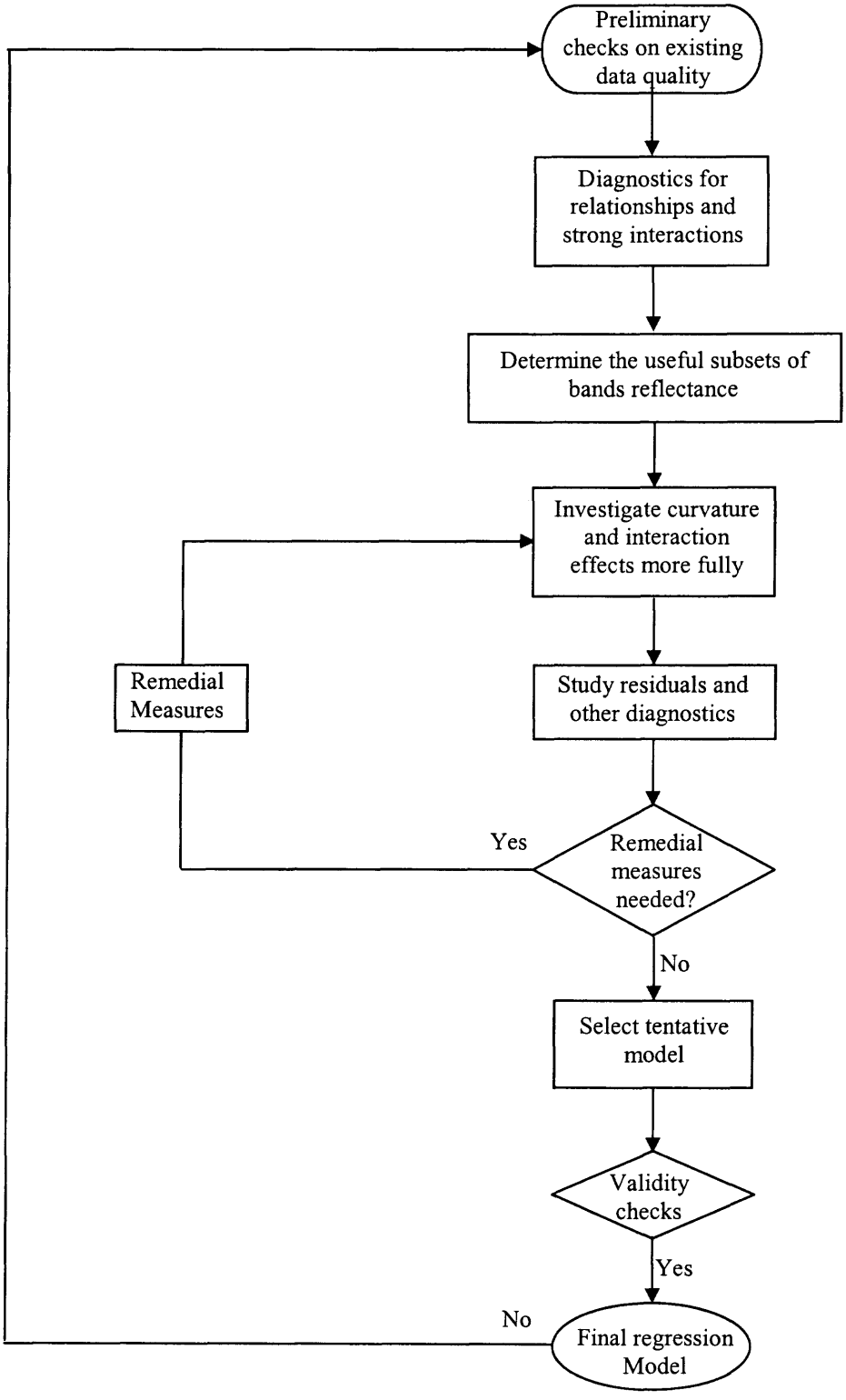

Figure 6.6 Strategy for Building the Regression Model

6.3.1 Data Refinement/Sample Extraction

The data collection requirements for building a regression model vary with the nature of the study. In general, there are four types of studies: Controlled Experiments, Controlled Experiments with Supplemental Variables, Confirmatory Observational Studies and Exploratory Observational Studies. This study is a controlled experiment in which the experimenter controls the levels of the independent variables (reflectance at different bands or band ratios) and assigns a treatment, consisting of a combination of levels of the independent variables, to each experimental unit and observes the response (water quality constituents concentrations). Since the ocean reflectance contains all the essential information concerning the quantitative properties of water constituents (Gordon, 1975), reflectance acquired by AVIRIS was used as the input data for the regression model. All the reflectance were derived from AVIRIS, and the concentrations of CHL and TSM were determined according to the Dutch standard norm (NEN 6520, 1981 and NEN 6484, 1982) respectively.

Once the data have been collected, edit checks should be performed and plots prepared to identify gross errors as well as extreme outlier. Difficulties with data errors are especially prevalent in large data sets and should be corrected or resolved before the model building begins.

6.3.2 Reduction of Independent Variables

The reduction of independent variables in the model-building phase is very important in this study. The purpose of independent variables reduction is to identify a small group of regression models that are "good" according to a specified criterion so that a detailed

examination can be made of these models, leading to the selection of the final regression model to be employed. AVIRIS can measure reflectance of 224 bands from which 41 bands were selected for this study, covering the rage of wavelengths from 380 to 780nm. (Note: those bands beyond 740nm will not be used to retrieve water quality concentrations due to the temperature-dependence of the absorption coefficient (Pegau and Zaneveld, 1993)). In addition to the selected 37 bands (380-740nm), researchers applied the band ratios in statistical regression models (Carder et al., 1991; Dekker and Hoogenboom, 1996; Althuis et al., 1996; Maritorena, 1998; O'Reilly et al., 1998; Liew et al., 2001;). In this research, ten band ratios are prepared and put into the pool of independent variables making the total of forty-seven independent variables in the pool. Many of those bands and band ratios are highly intercorrelated. Hence, the number of bands and band ratios should be reduced in the final model for the following reasons (Neter, et al., 1996):

a) A regression model with numerous independent variables may be difficult to apply;

b) Regression models with a limited number of independent variables are more easily understood;

c) The presence of many highly intercorrelated independent variables may substantially increase the sampling variation of the regression coefficients, detract from the model's descriptive abilities, increase the problem of roundoff errors, and not improve, or even worsen, the model's predictive ability.

In the following regression procedures, the selection of bands or band ratios is not restricted to the significance in absorption or scattering properties. It is based on the statistical criterions which are described in succeeding sections.

1. Scatter plot matrix and correlation matrix

Scatter plots of the response variable against each independent variable can aid in determining the nature and strength of the bivariate relationships between each of the independent variables and the response variable and identifying gaps in the data points as well as outlying data points. Scatter plots of each independent variable against each of the other independent variables are helpful for studying the bivariate relationships among the predictor variables and for finding gaps and detecting outliers. Figure 6.7 is a part of the scatter plots of reflectance for all the bands/band ratios and CHL_a concentrations.

A component to the scatter plot matrix is the correlation matrix. This matrix contains the coefficients of simple correlations between CHL_a concentration and each of the independent variables, as well as all of the coefficients of simple correlation among the independent variables. From scatter plots and the correlation matrix defined in Appendix A.1 and A.2, the intercorrelation between all the variables can be qualitatively and quantitatively found. All independent variables with correlation coefficients greater than 0.90 should be dropped from the pool of potential independent variables. As a result, Band7(440nm), Band8(450nm), Band10(470nm), Band12(490nm) to Band15(520nm), Band17(540nm), Band23(600nm), Band29(660nm) to Band31(680nm), Band34(710nm) to Band37(740nm) bands reflectance and 4 ratios: $\frac{R(0-)_{710}}{R(0-)_{680}}$, $\frac{R(0-)_{560}-R(0-)_{740}}{R(0-)_{510}-R(0-)_{740}}$, $\frac{R(0-)_{560}-R(0-)_{740}}{R(0-)_{520}-R(0-)_{740}}$ and $\frac{R(0-)_{490}}{R(0-)_{560}}$, totally 20 variables, are kept as the new pool of independent variables.

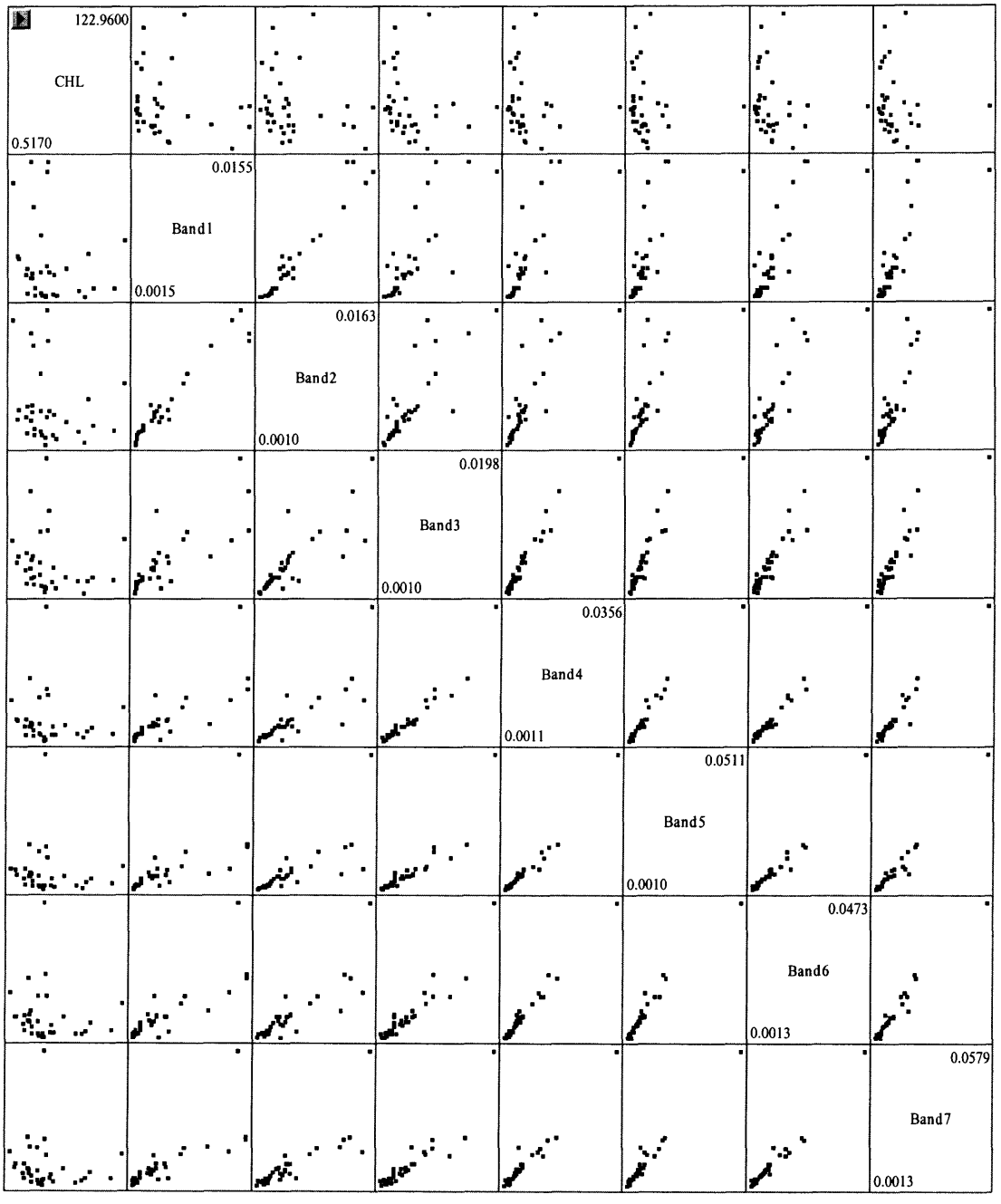

Figure 6.7 Part of scatter plots between CHL_a concentrations and reflectance at different bands

In the above figure, the response variable CHL_a concentration for any one scatter plot is the name found in its row, and the independent variable is the name found in its column. Thus, the scatter plot matrix in figure 6.7 shows in the first row the plots of

CHL (CHL_a concentrations) against ratio of Band1 (380nm) to Band37 (740nm). Alternatively, by viewing the second column, the plots of Band1 (380nm) against CHL_a concentrations and other bands reflectance can be studied.

2. R_p^2 or SSE_p Criterion

The R_p^2 criterion calls for the use of the coefficient of multiple determination R^2, defined in Appendix A.5, in order to identify several "good" subsets of independent variables — in other words, subsets for which R_p^2 is high. The number of parameters in the regression model is shown as a subscript of R^2. Thus R_p^2 indicates that there are p parameters, or p-1 independent variables, in the regression function on which R_p^2 is based.

The R_p^2 criterion is equivalent to using the errors sum of squares SSE_p (Appendix A.6) as the criterion (the number of parameters in the regression model is again shown as a subscript). With the SSE_p criterion, subsets for which SSE_p is small are considered "good".

The R_p^2 criterion is not intended to identify the subsets which maximize this criterion and SSE_p do not increase any more as additional X variables included in the model. Hence, R_p^2 will be a maximum when all p-1 potential independent variables are included in the regression model. The intent in using R_p^2 criterion is to find the point where adding more independent variables is not worthwhile because it leads to a very small increase in R_p^2 (Figure 6.8, Table 6.2).

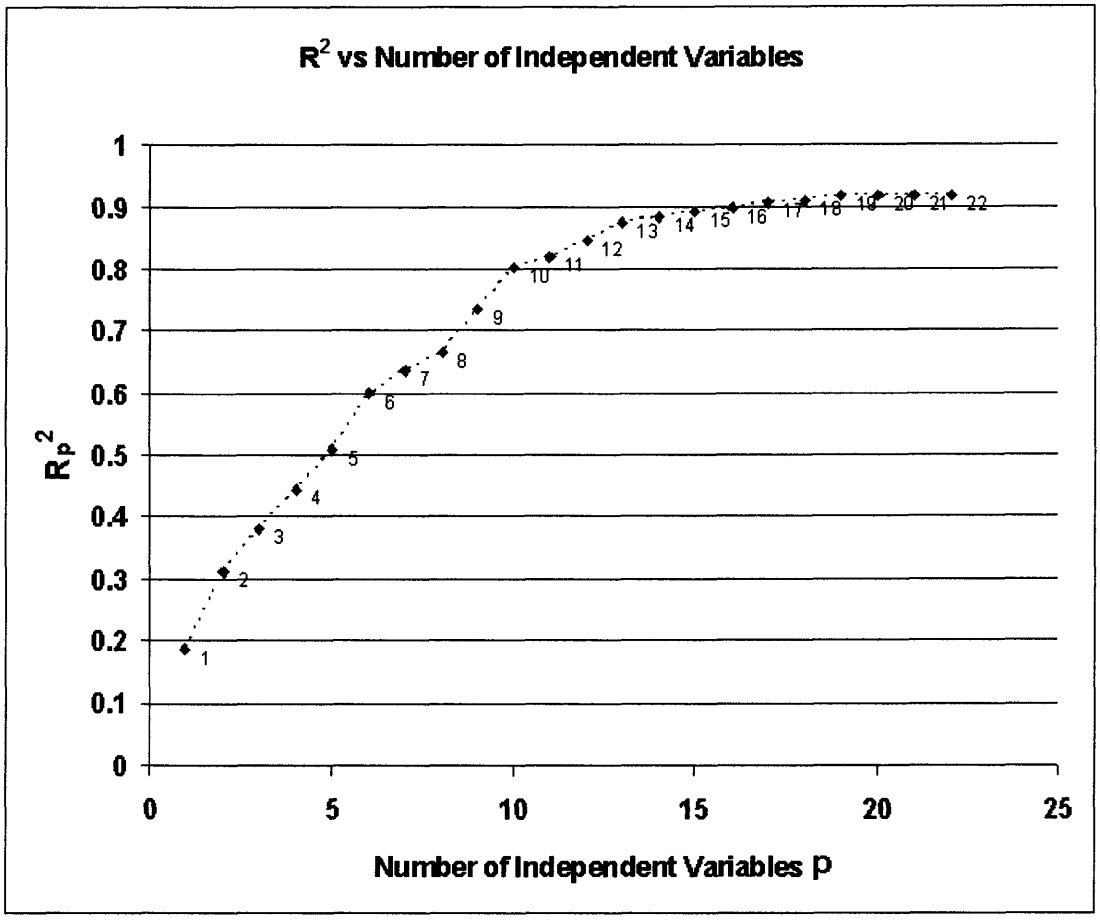

Figure 6.8 R_p^2 plot for reduction of independent variables

Figure 6.8 contains a plot of the R_p^2 values against p, the number of parameters in the regression model. The maximum R_p^2 value for the possible subsets each consisting of p-1 predictor variables, denoted by max (R_p^2), which appears at the top of the graph for each p. These points are connected by dashed lines to show the impact of adding additional independent variables. Figure 6.8 makes it clear that little increase in max(R_p^2) takes place after 13, 14 or 15 bands reflectance or band ratios are included in the model. Hence, a subset with 13 independent variables including band7, band9, band10, band15, band18, band23, band25, band28, band35, ratio1, ratio3, ratio6 and ratio9, a subset with 14 independent variables including band7, band9, band10, band15, band18, band23,

band27, band28, band35, ratio2, ratio3, ratio6, ratio7 and ratio9 and a subset with 15 independent variables including band7, band9, band10, band15, band18, band23, band27, band28, band35, band37, ratio2, ratio3, ratio6, ratio7 and ratio9 within the regression model appear to be reasonable according to the R_p^2 criterion.

3. R_a^2 or MSE_p Criterion

Since R_p^2 does not take account of the number of parameters in the regression model and since max (R_p^2) can never decrease as p increases, the adjusted coefficient of multiple determination R_a^2 (Appendix A.7) and MSE_p are used as another criterion. From Appendix A.7, it can be seen that R_a^2 increases if and only if MSE decreases. Hence, R_a^2 and MSE provide equivalent information.

MSE_p shows the number of parameters in the regression model as a subscript of the criterion. The smallest MSE_p for a given number of parameters in the model, min (MSE_p), can, indeed, increase as p increases. This occurs when the reduction in SSE becomes so small that it is not sufficient to offset the loss of an additional degree of freedom. The MSE_p criterion seeks to find a few subsets for which MSE_p is at the minimum or so close to the minimum that adding more independent variables is not worthwhile.

Figure 6.10 contains the MSE_p plot for this regression. The min (MSE_p) values are connected by dashed lines. The conclusion of the MSE_p plot in figure 6.10 is very similar to that of the R_p^2 plot in figure 6.8, and R_a^2 plot in figure 6.9. The subsets with 13, 14 and 15 independent variables have the maximum R_a^2 and minimum MSE values.

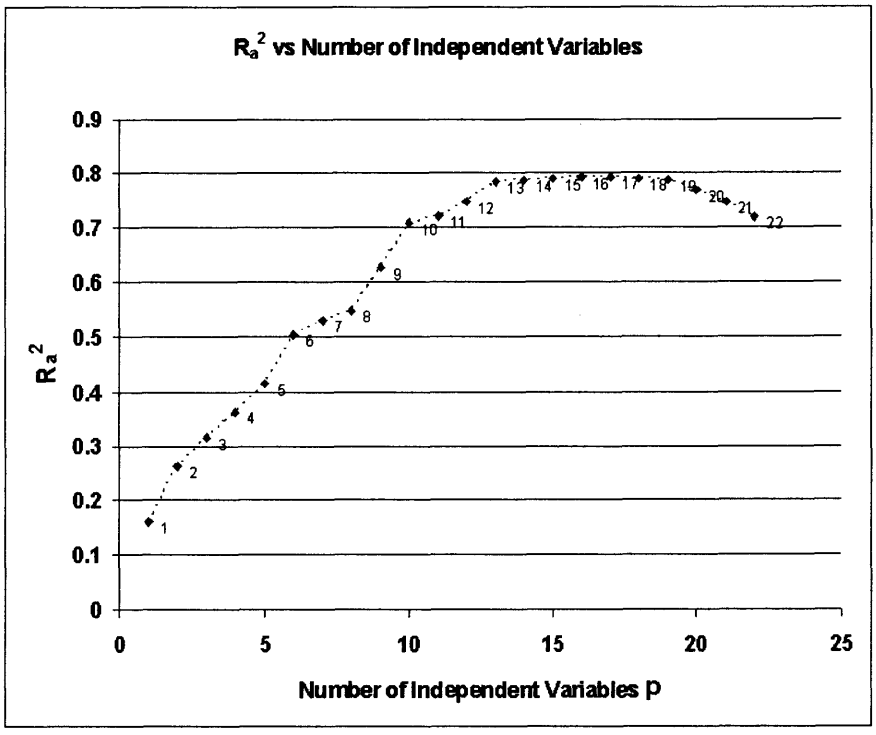

Figure 6.9 R_a^2 plot for reduction of independent variables

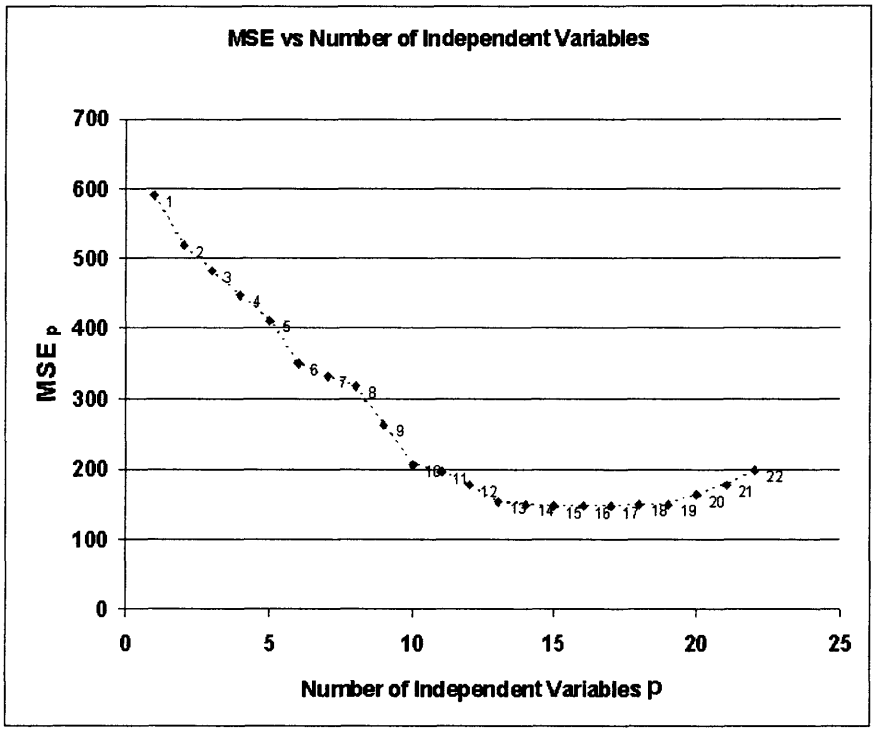

Figure 6.10 MSE_p plot of independent variables

Table 6.2 Part of R_p^2, MSE_p, C_p Values for All Possible Regression Models

Variables Number in Model	Adjusted R-Square	R-Square	C(p)	MSE
16	0.7925	0.8996	13.099	145.9656
17	0.7919	0.906	14.3863	146.3485
15	0.7911	0.8922	11.9158	146.9129
15	0.789	0.8911	12.0393	148.4359
17	0.7889	0.9047	14.5397	148.51
18	0.7885	0.9113	15.8057	148.796
19	0.7881	0.918	17.0657	149.0315
15	0.7876	0.8904	12.1178	149.4027
14	0.7876	0.8835	10.8765	149.4188
14	0.7869	0.8831	10.9183	149.9034
18	0.7869	0.9106	15.8788	149.9047
14	0.786	0.8827	10.97	150.5036
14	0.7857	0.8825	10.9885	150.719
17	0.7851	0.903	14.7258	151.1329
18	0.785	0.9098	15.9653	151.2185
14	0.7844	0.8817	11.0724	151.6919
17	0.7838	0.9024	14.7926	152.074
16	0.7835	0.8952	13.58	152.2913
...	...	...	...	...

In Table 6.2, the first several rows which stand for different combinations of independent variables have the maximum R_a^2 and minimum MSE values. Due to the R_a^2 and MSE criterions, the independent variables combination for the best regression model should be one of them.

4. C_p Criterion

In using the C_p (Appendix A.8) criterion, we seek to identify subsets of independent variables for which (1) the C_p value is small and (2) the C_p value is near p. Subsets with small C_p values have a small total mean squared error, and when the C_p is also near p, the bias of the regression model is small.

From Table 6.2, the first subset with 14 bands (Band7, Band8, Band10, Band17, Band23, Band29, Band31, Band36, Band37, Band39, ratio1, ratio4, ratio5 and ratio10) is the best one which satisfies C_p criterion very well.

6.3.3. Model Refinement and Selection

Once the all-possible-regressions procedure has identified a few "good" subsets from the pool of potential independent variables, a final choice of the model variables must be made. This choice, as indicated by the model-building strategy in Figure 6.5, is aided by residual analysis and other diagnostics for each of the competing models, and is finally confirmed by model validation.

a. Models resulted from all-possible-regression procedure

Inputting the above subset with 13 bands reflectance or ratios as independent variables, the regression model can be estimated by the least square method (Appendix A.4). The result is:

$$\begin{aligned} CHL = {} & 143.70 + 9615.15R(0-)_{440} - 16735R(0-)_{450} + 11589R(0-)_{470} - 2112.04R(0-)_{520} \\ & + 3901.46R(0-)_{550} - 5609.91R(0-)_{600} + 17431R(0-)_{620} - 26570R(0-)_{650} \\ & + 8036.82R(0-)_{720} - 16.53\frac{R(0-)_{710}}{R(0-)_{680}} - 11.87\frac{R(0-)_{560} - R(0-)_{740}}{R(0-)_{510} - R(0-)_{740}} \\ & + 10.67\frac{R(0-)_{560} - R(0-)_{740}}{R(0-)_{520} - R(0-)_{740}} - 224.03\frac{R(0-)_{490}}{R(0-)_{560}} \end{aligned} \tag{6.13}$$

Table 6.3 is ANOVA table for this regression model.

Table 6.3 ANOVA Table for Regression Model (6.13)

Analysis of Variance					
Source	DF	Sum of Squares	Mean Square	F Value	Pr > F
Model	13	19065	1466.50363	9.63	<.0001
Error	18	2741.46320	152.30351		
Corrected Total	31	21806			
Root MSE		12.34113	**R-Square**	**0.8743**	
Dependent Mean		38.17173	**Adj R-Sq**	**0.7835**	
Coeff Var		32.33055			

Result for the subset with fourteen independent variables is:

$$
\begin{aligned}
CHL = {} & 129.40 + 9317.07R(0-)_{440} - 16794R(0-)_{450} + 11762R(0-)_{470} - 2630.46R(0-)_{520} \\
& + 594.91R(0-)_{550} + 3599.18R(0-)_{600} - 5487.01R(0-)_{640} + 17117R(0-)_{650} \\
& - 25759R(0-)_{660} + 7679.41R(0-)_{720} - 19.53\frac{R(0-)_{710}}{R(0-)_{680}} \\
& - 10.96\frac{R(0-)_{560} - R(0-)_{740}}{R(0-)_{510} - R(0-)_{740}} + 10.48\frac{R(0-)_{560} - R(0-)_{740}}{R(0-)_{520} - R(0-)_{740}} - 185.36\frac{R(0-)_{490}}{R(0-)_{560}}
\end{aligned}
\tag{6.14}
$$

Table 6.4 ANOVA Table for Regression Model (6.14)

Analysis of Variance					
Source	DF	Sum of Squares	Mean Square	F Value	Pr > F
Model	14	19266	1376.13508	9.21	<.0001
Error	17	2540.11922	149.41878		
Corrected Total	31	21806			
Root MSE		12.22370	**R-Square**	**0.8835**	
Dependent Mean		38.17173	**Adj R-Sq**	**0.7876**	
Coeff Var		32.02290			

Result for the subset with 15 independent variables is:

$$CHL = 108.16 + 9805.36R(0-)_{440} - 16959R(0-)_{450} + 11774R(0-)_{470} - 2142.36R(0-)_{520} \quad (6.15)$$
$$+ 4290.61R(0-)_{550} - 5875.48R(0-)_{600} + 17865R(0-)_{620} - 30560R(0-)_{640}$$
$$+ 11069R(0-)_{650} - 25896R(0-)_{660} + 7645R(0-)_{720} - 11.53\frac{R(0-)_{710}}{R(0-)_{680}} +$$
$$-10.26\frac{R(0-)_{560} - R(0-)_{740}}{R(0-)_{510} - R(0-)_{740}} + 12.96\frac{R(0-)_{560} - R(0-)_{740}}{R(0-)_{520} - R(0-)_{740}} - 224.03\frac{R(0-)_{490}}{R(0-)_{560}}$$

Table 6.5 ANOVA Table for Regression Model (6.15)

Analysis of Variance					
Source	DF	Sum of Squares	Mean Square	F Value	Pr > F
Model	15	19455	1297.02698	8.83	<.0001
Error	16	2350.60559	146.91285		
Corrected Total	31	21806			
Root MSE		12.12076	**R-Square**	**0.8922**	
Dependent Mean		38.17173	**Adj R-Sq**	**0.7911**	
Coeff Var		31.75324			

Comparing the three ANOVA tables, it is clear that Table 6.3 is almost the same as Table 6.4 and Table 6.5 which means the regression using the subset of thirteen bands reflectance or ratios as independent variables produces the same statistical model as that subset of fourteen or fifteen independent variables.

b. Application of stepwise regression procedure

In those occasional cases when the pool of potential independent variables contains forty or more variables, some automatic search procedures were developed to minimize computational effort, as compared with the all-possible-regressions procedure. The stepwise regression procedure is the most widely used of the automatic search methods. Essentially, this search method develops a sequence of regression models, at each step adding or deleting an independent variable. The criterion for adding or deleting an independent variable can be stated equivalently in terms of error sum of squares

reduction, coefficient of partial correlation, t^* statistic, or F^* statistic (Appendix .A. 9, A.10)

The result for this regression model is:

$$\begin{aligned} CHL = {} & 203.43 + 15970R(0-)_{440} - 16360R(0-)_{450} + 12665R(0-)_{470} - 4189.76R(0-)_{540} \\ & + 2733.95R(0-)_{600} - 4425.11R(0-)_{640} - 3164.14R(0-)_{650} + +4292.67R(0-)_{660} \\ & + 18160R(0-)_{710} - 29882R(0-)_{730} + 8967.70R(0-)_{740} - 38.9\frac{R(0-)_{710}}{R(0-)_{680}} \\ & - 51.40\frac{R(0-)_{440} - R(0-)_{740}}{R(0-)_{510} - R(0-)_{740}} + 107.52\frac{R(0-)_{490} - R(0-)_{740}}{R(0-)_{510} - R(0-)_{740}} \\ & - 22.98\frac{R(0-)_{560} - R(0-)_{740}}{R(0-)_{510} - R(0-)_{740}} + 9.75\frac{R(0-)_{560} - R(0-)_{740}}{R(0-)_{520} - R(0-)_{740}} \\ & - 0.25\frac{R(0-)_{620} - R(0-)_{740}}{R(0-)_{520} - R(0-)_{740}} + 0.79\frac{R(0-)_{660} - R(0-)_{740}}{R(0-)_{520} - R(0-)_{740}} \\ & - 114.87\frac{R(0-)_{440}}{R(0-)_{550}} + 55.57\frac{R(0-)_{520}}{R(0-)_{550}} - 437.37\frac{R(0-)_{490}}{R(0-)_{560}} \end{aligned} \tag{6.16}$$

Table 6.6 ANOVA Table for Regression Model (6.16)

Analysis of Variance					
Source	DF	Sum of Squares	Mean Square	F Value	Pr > F
Model	21	20023	953.46193	5.35	0.0046
Error	10	1783.30993	178.33099		
Corrected Total	31	21806			
Root MSE		13.35406	**R-Square**	**0.9182**	
Dependent Mean		38.17173	**Adj R-Sq**	**0.7465**	
Coeff Var		34.98417			

Table 6.3, 6.4, 6.5 and 6.6 show the regression coefficients of the above three regressions are 0.8743, 0.8835, 0.8922 and 0.9182 respectively, and the adjusted regression coefficients are 0.7835, 0.7876, 0.7911 and 0.7465. Before the final regression model is determined, the multicollinearity of each model should be diagnosed.

c. Selecting model and identifying outlying observations

One formal widely used method of detecting the presence of multicollinearity is by means of variance inflation factors (VIF). VIF measures how much the variances of the estimated regression coefficients are inflated as compared to when the independent variables are not linearly related. The mean VIF value of all independent variables is often used as an indicator of the severity of multicollinearity. In this research, the mean value of VIF(Appendix A.11) for the above models (6.13), (6.14), (6.15) and (6.16) are 44.62, 43.58, 48.91 and 225.56 respectively, which indicates the best model is (6.14) with the subset of 14 bands reflectance or band ratios as independent variables.

d. Residual analysis

Whether a regression model is appropriate for the data being analyzed can be studied from a residual plot against the independent variables or, equivalently, from a residual plot against the fitted values. The plot of the residuals against the fitted values can also be used to find the outliers in the data set.

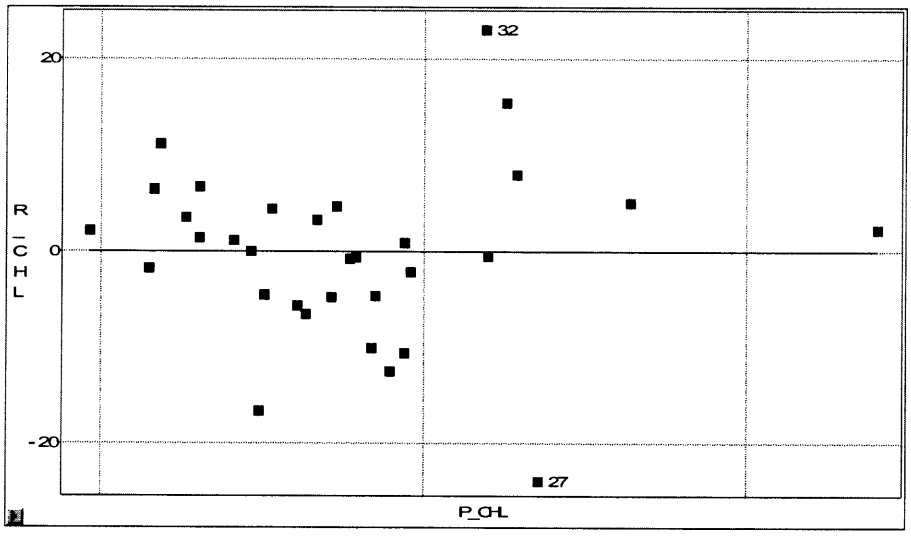

Figure 6.11 Residual plot against predicted CHL_a concentrations from model (6.14).

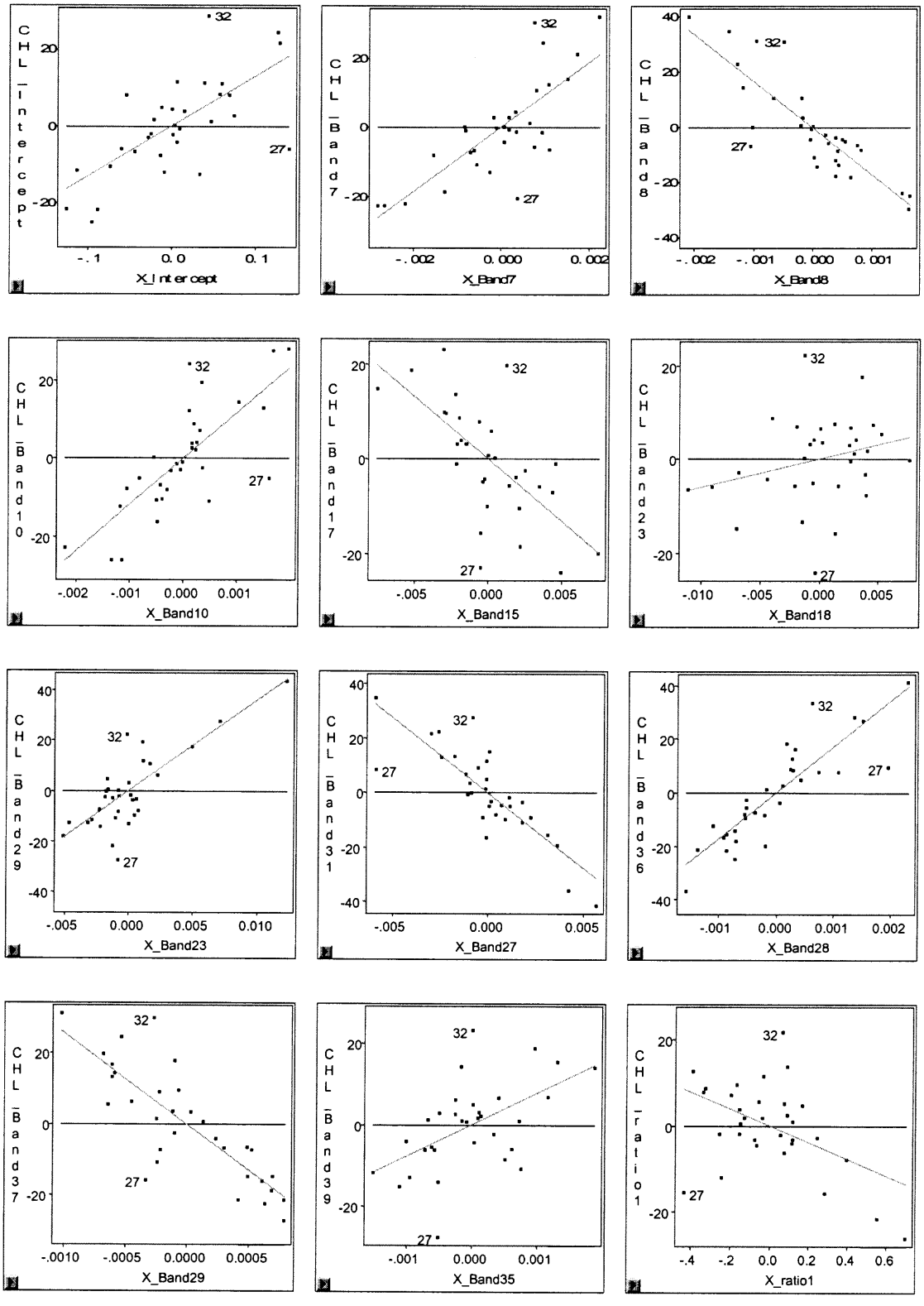

Figure 6.12 Partial leverage residual plots for model (6.14)

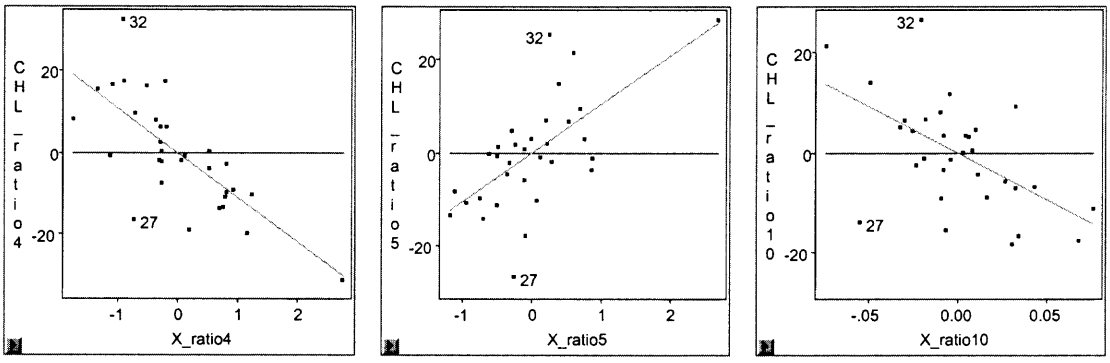

Figure 6.12 Partial leverage residual plots for model (6.3) (continued)

In Figure 6.11, P_CHL stands for the predicted CHL_a concentrations using model (6.14) and R_CHL stands for the residuals using the same model. Figure 6.11 shows the residuals distribute randomly instead of following some specific curve, which means the regression model is appropriate. Figure 6.12 are the partial leverage residual plots for intercept and each selected explanatory variable in model (6.14). Two reference lines are also displayed in the plots. One is the horizontal line, and the other is the fitted regression of CHL_a concentrations against that specific independent variable. The leverage plot shows the changes in the residuals for the model with and without the independent variable. For a given data point in the plot, its residual without the explanatory variable is the vertical distance between the point and the horizontal line; its residual with the explanatory variable is the vertical distance between the point and the fitted line. From Figure 6.11 and all plots in Figures 6.12, the observations #27 and #32 are clearly shown as outliers which should be ruled out from the model.

After the outliers are taken away, a new regression model resulting from the same regression procedure described above is:

$$CHL = 155.21 + 9204.55R(0-)_{440} - 17743R(0-)_{450} + 13683.1R(0-)_{470} - 2774.82R(0-)_{520} + 629.71R(0-)_{550} + 3532.52R(0-)_{600} - 6392.55R(0-)_{640} + 18976.4R(0-)_{650} - 26336R(0-)_{660} + 6741.41R(0-)_{720} - 27.09\frac{R(0-)_{710}}{R(0-)_{680}} - 11.07\frac{R(0-)_{560} - R(0-)_{740}}{R(0-)_{510} - R(0-)_{740}} + 9.66\frac{R(0-)_{560} - R(0-)_{740}}{R(0-)_{520} - R(0-)_{740}} - 224.68\frac{R(0-)_{490}}{R(0-)_{560}} \quad (6.17)$$

Table 6.7 ANOVA Table for The Regression (6.17)

Analysis of Variance					
Source	DF	Sum of Squares	Mean Square	F Value	Pr > F
Model	14	18431	1316.52906	15.88	<.0001
Error	15	1243.22005	82.88134		
Corrected Total	29	19675			
Root MSE		9.10392	**R-Square**	**0.9368**	
Dependent Mean		36.48119	**Adj R-Sq**	**0.8778**	
Coeff Var		24.95510			

Comparing R^2 and R_a^2 from Table 6.6 and 6.7, we find the regression model has been improved. The residual plots for the new model are figure 6.13, figure 6.14 as following:

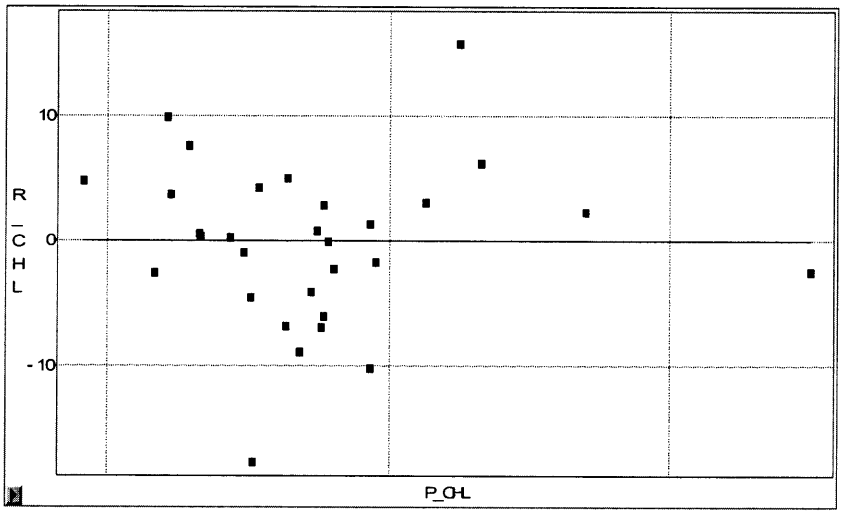

Figure 6.13 Residual plot against predicted CHL_a concentrations for model (6.17).

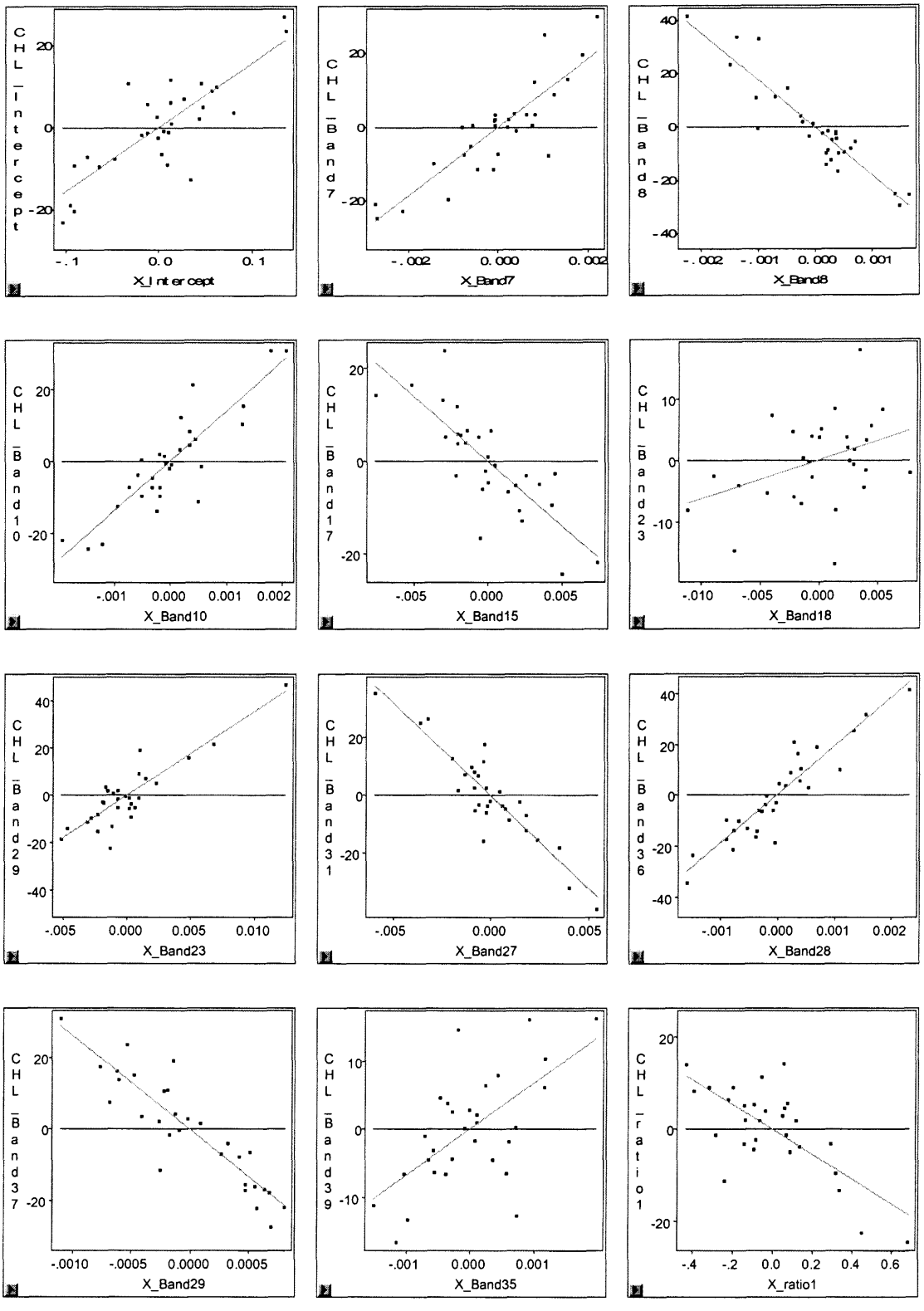

Figure 6.14 Partial leverage residual plots for model (6.17)

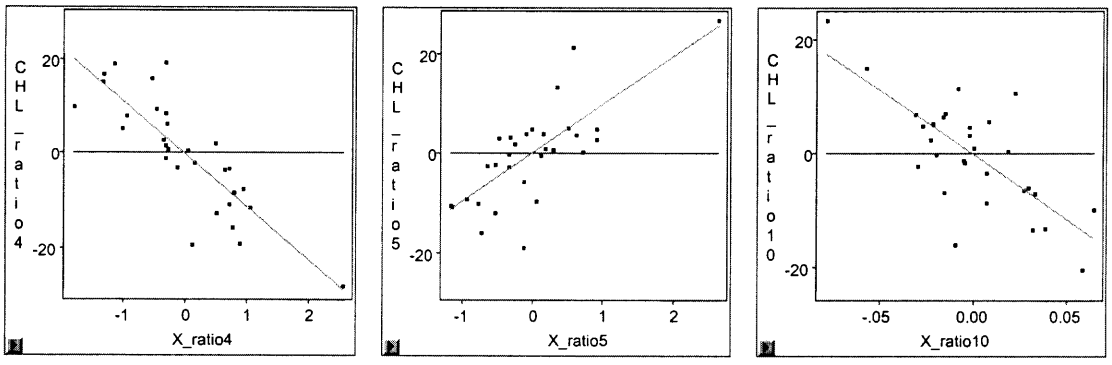

Figure 6.14 Partial leverage residual plots for model (6.17) (continued)

A normal quantile-quantile plot of residuals is illustrated by the following plot. See the Appendix A .12 for an explanation of the horizontal axis. The empirical quantiles are plotted against the quantiles of a standard normal distribution. If the residuals are from a normal distribution with mean 0, the points tend to fall along the reference line that has an intercept of 0 and a slope equal to the estimated standard deviation.

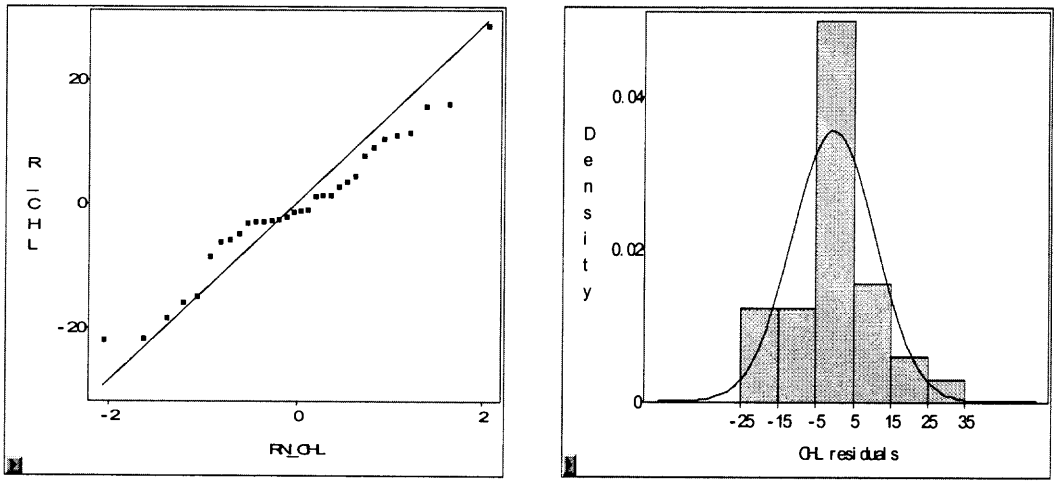

Figure 6.15 Residual normal QQ plot for model (6.17)

The coefficient of correlation between the ordered residuals and their expected values under normality is 0.966. This high value (the interpolated critical value for α=0.05 is 0.94 in Table "Critical Values for Coefficient of Correlation between Ordered Residuals and Expected Values under Normality when Distribution of Error Terms Is

Normal", Neter et al., 1996) helps to confirm the reasonableness of the conclusion that the error terms are fairly normally distributed, which again indicates the model (6.17) is appropriate.

6.3.4 Model Validation

The results of the comparison between CHL_a concentration measured in situ from water samples against the concentration deduced from regression model (6.5) are presented in Figure 6.16.

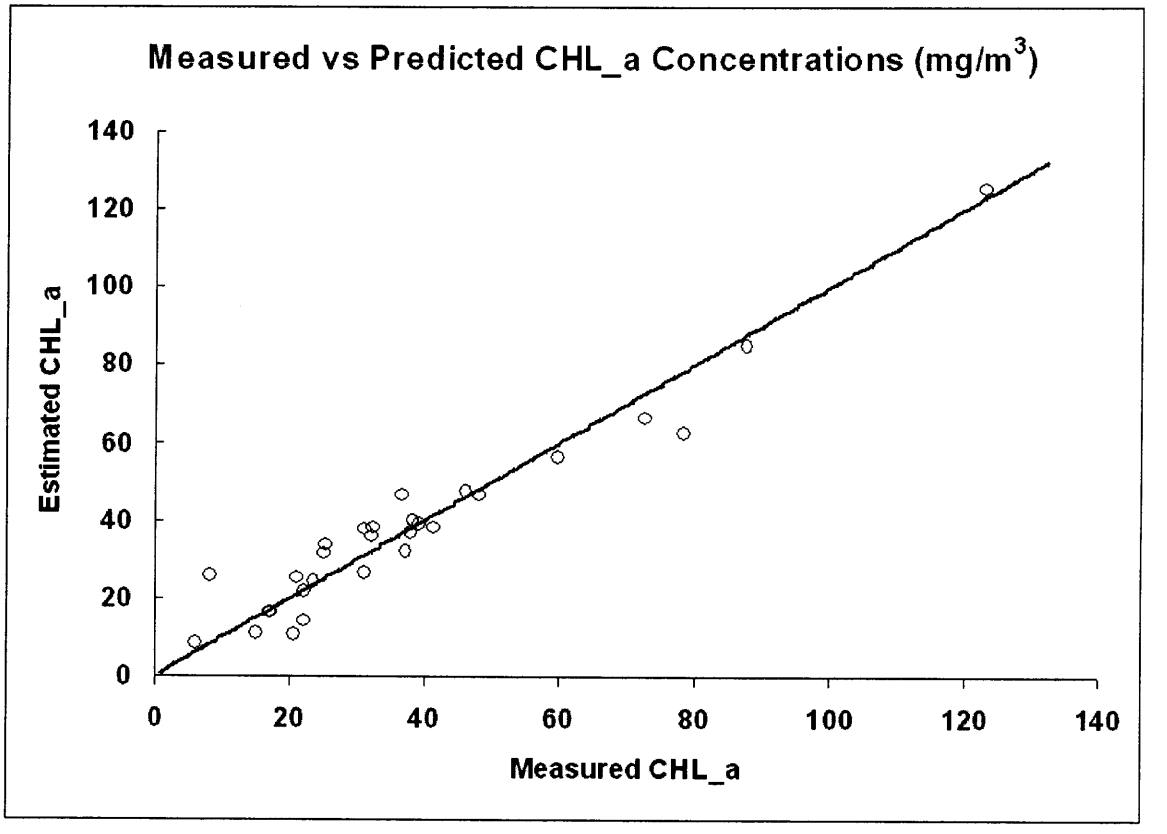

Figure 6.16 Comparison of CHL_a concentration derived from regression model (6.17) against water sample measurements

Similarly, the regression model for TSM concentration retrieval can be obtained as:

$$\begin{aligned} CHL = {} & 16.42 + 2128.32R(0-)_{440} - 4858.90R(0-)_{450} + 3181.29R(0-)_{460} \\ & - 1232.60R(0-)_{470} - 1238.84R(0-)_{540} + 2012.21R(0-)_{550} \\ & - 2118.58R(0-)_{600} + 1171.36R(0-)_{610} + 1336.61R(0-)_{620} \\ & - 810.5R(0-)_{630} - 912.86R(0-)_{640} + 1160.89R(0-)_{710} \\ & + 947.88R(0-)_{720} - 1361.80R(0-)_{730} + 5.85\frac{R(0-)_{490}}{R(0-)_{560}} \end{aligned} \tag{6.18}$$

Table 6.8 ANOVA Table for the regression (6.18)

Analysis of Variance					
Source	DF	Sum of Squares	Mean Square	F Value	Pr > F
Model	15	1024.97974	68.33198	17.50	<.0001
Error	16	62.46986	3.90437		
Corrected Total	31	1087.44960			
Root MSE		1.97595	**R-Square**		**0.9426**
Dependent Mean		14.78250	**Adj R-Sq**		**0.8887**
Coeff Var		13.36680			

Figure 6.17 is a comparison between TSM concentration measured in situ from water samples against concentration deduced from regression model (6.18).

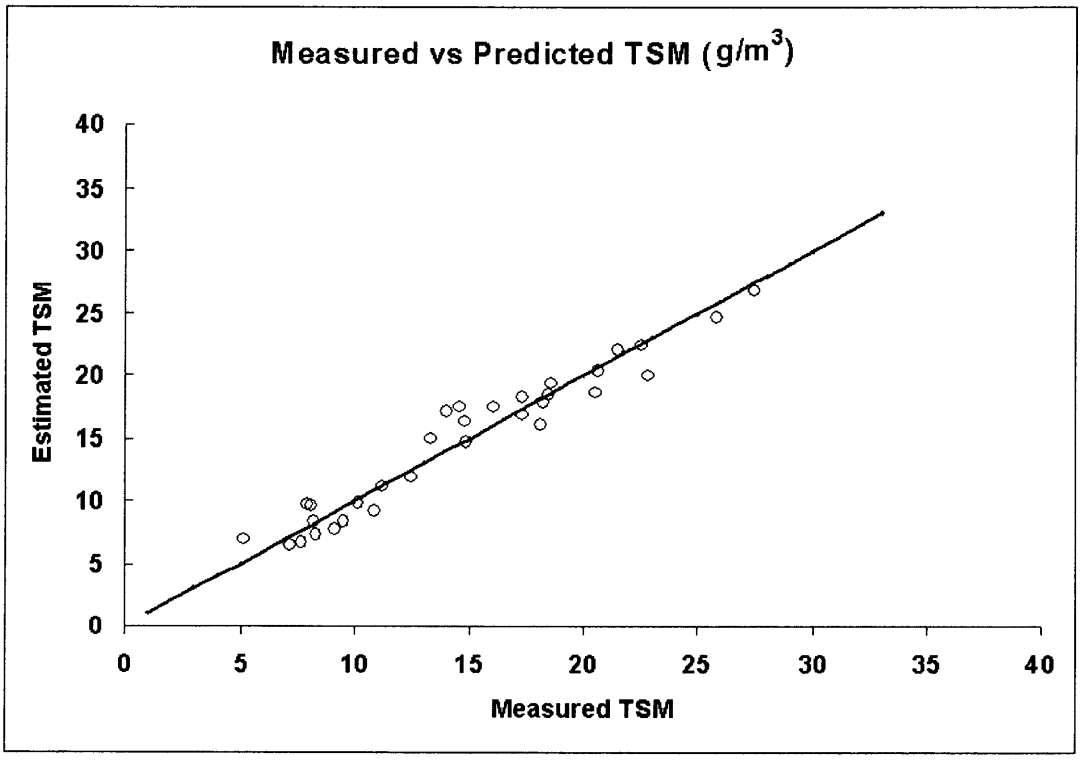

Figure 6.17 Comparison of TSM concentration derived from regression model (6.18) against water sample measurements.

The statistical models can be used to validate the MIM methods. The selection of independent variables are independent of the significance of the selected bands absorption/scattering, and it is based on the pure statistical correlation between band/band ratios and CHL/TSM concentrations.

CHAPTER 7

GIS APPLICATION

Geographic Information System (GIS) is a system that contains spatially referenced data that can be analyzed and converted to information for a specific set of purposes or applications. In the GIS system, we can collect, store and retrieve information based on its spatial location, identify locations within a targeted environment which meet specific criteria, analyze the related data spatially as an aid to making decisions about that environment and display the selected environment both graphically and numerically either before or after analysis.

In this research, the technology of the GIS is used to map the distribution of water constituent concentrations and to develop a database for assessing the water quality conditions of the study area. Varieties of geospatial data in both digital and analog forms were input for the GIS database development and spatial analyses were performed using a GIS software—ArcView. This database provides a baseline integrated GIS system which can be used by water resource managers and planners for better monitoring and management of water quality condition.

The GIS system of the study area represents a variety of qualities and characteristics reflecting the water quality conditions of the study area. All these qualities and characteristics are georeferenced and linked to the base map which was digitized from the navigational chart with the locations of the sample points cruised during data collections (1999-2001). The characteristic data integrated into GIS are: distributions of PH value, temperature, secchi depth, salinity, CHL_a, TSM and CDOM

concentrations (Figure 7.1). They are stored as theme layers in the GIS, with each layer linked to the same georeferencing system.

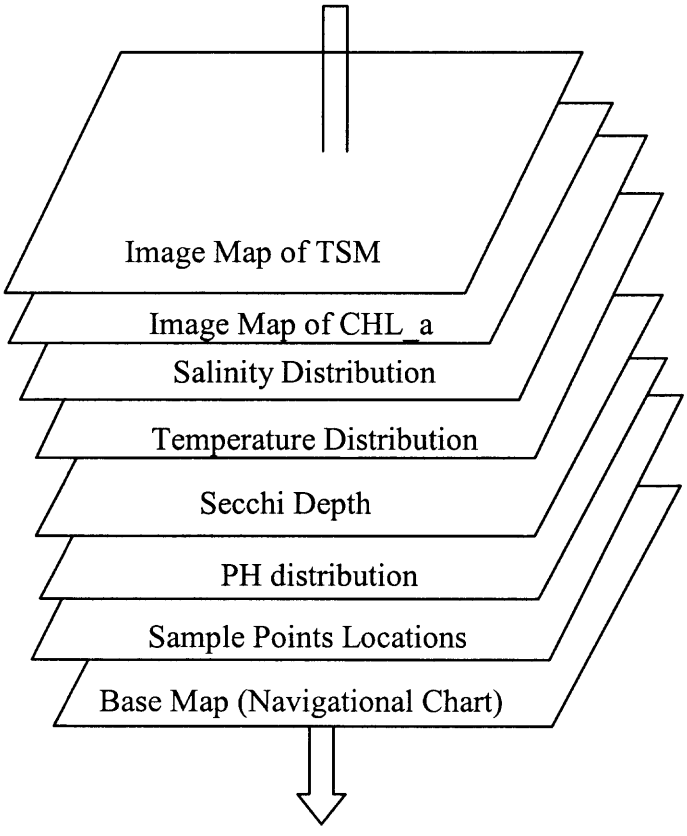

Figure 7.1 Organization of data stored as thematic layers in this GIS

In addition to the spatial characteristics, each thematic layer has a unique non-spatial component which is stored as an attribute. Table 7.1 lists the geographic characteristics of each layer in this GIS.

Table 7.1 Geographic Characteristics of Each Layer

Layer Names	Feature Class	Shape	Projection	Format	Attributes
Navigational Chart	Vector	PolyLline	Geographic	Shape file	PolyLine ID, Fnode, Tnode, Length,
Boundary of Study Area	Vector	PolyLine	Geographic	Shape file	PolyLine ID, Fnode, Tnode, Length,
Sample Points Locations	Vector	Points	Geographic	Shape file	Latitude, Longitude, Temperature, Salinity, Secchi Depth, TSM, CDOM, CHL_a Concentrations
PH Distribution	Raster	Grids	Geographic	Grid file	PH value
Salinity Distribution	Raster	Grids	Geographic	Grid file	Salinity value
Temperature Distribution	Raster	Grids	Geographic	Grid file	Temperature Value
Seechi Depth Distribution	Raster	Grids	Geographic	Grid file	Secchi Depths
Image Map of CHL_a	Raster	Pixels	Geographic	Image file	CHL_a Concentrations
Image Map of TSM	Raster	Pixels	Geographic	Image file	TSM Concentrations

The incorporated system is an analytical tool for locating water quality parameters throughout the study area quickly, improved performance for data retrieval, geographic analysis capabilities, and rapid generation of high quality map products. In addition, planners can now access metadata about each layer of information in this system along with high-resolution images. The following maps (Figures 7.2 – 7.7) were generated for the GIS database system of the study area.

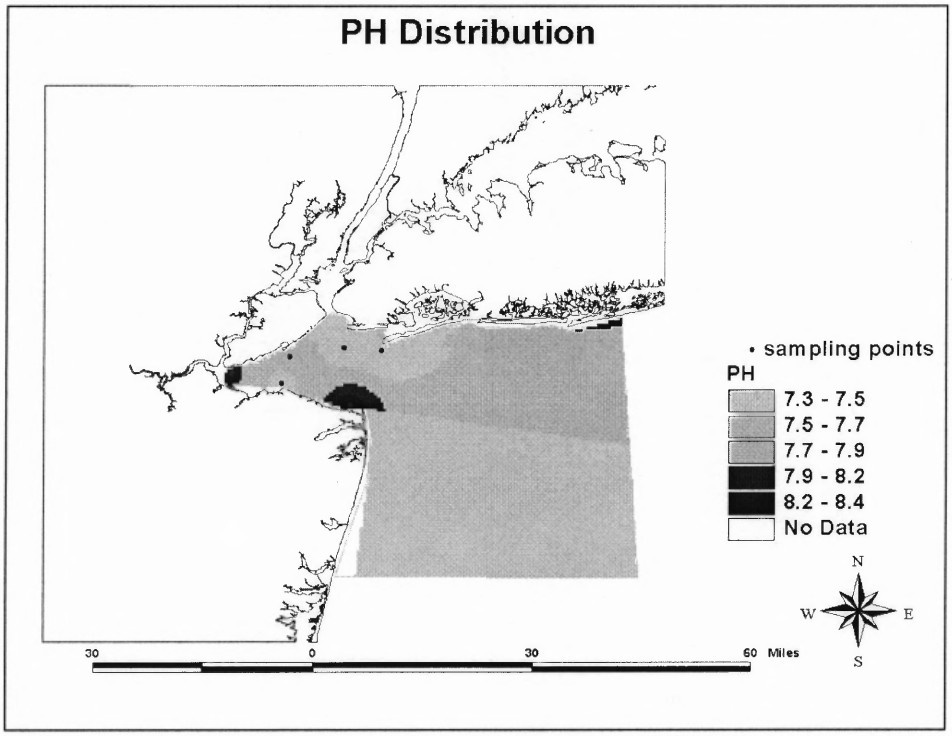

Figure 7.2 PH values distribution map of study area

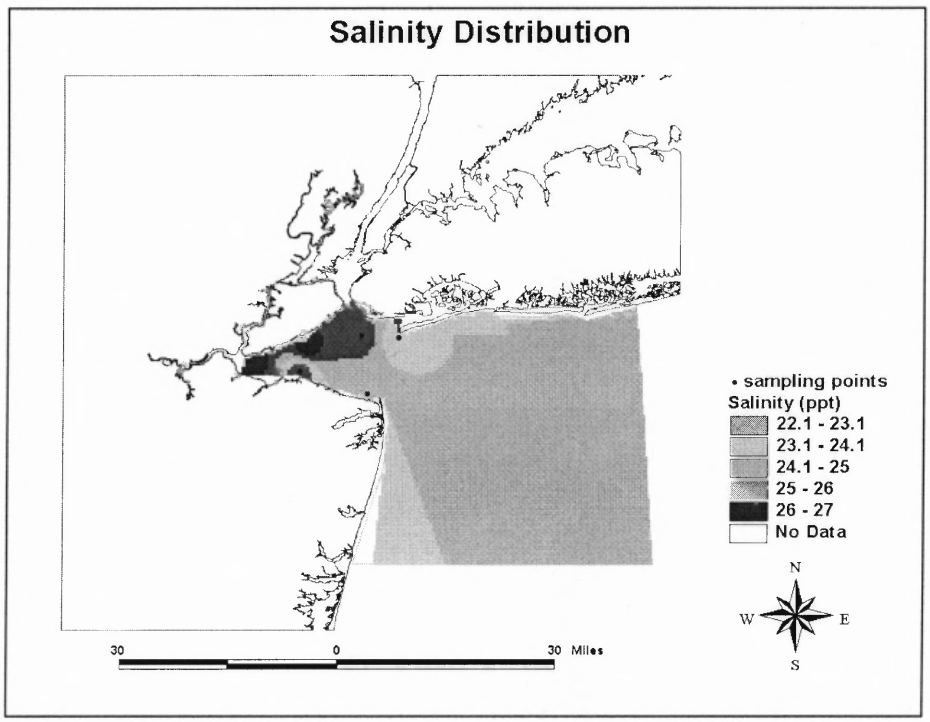

Figure 7.3 Salinity values distribution map of study area

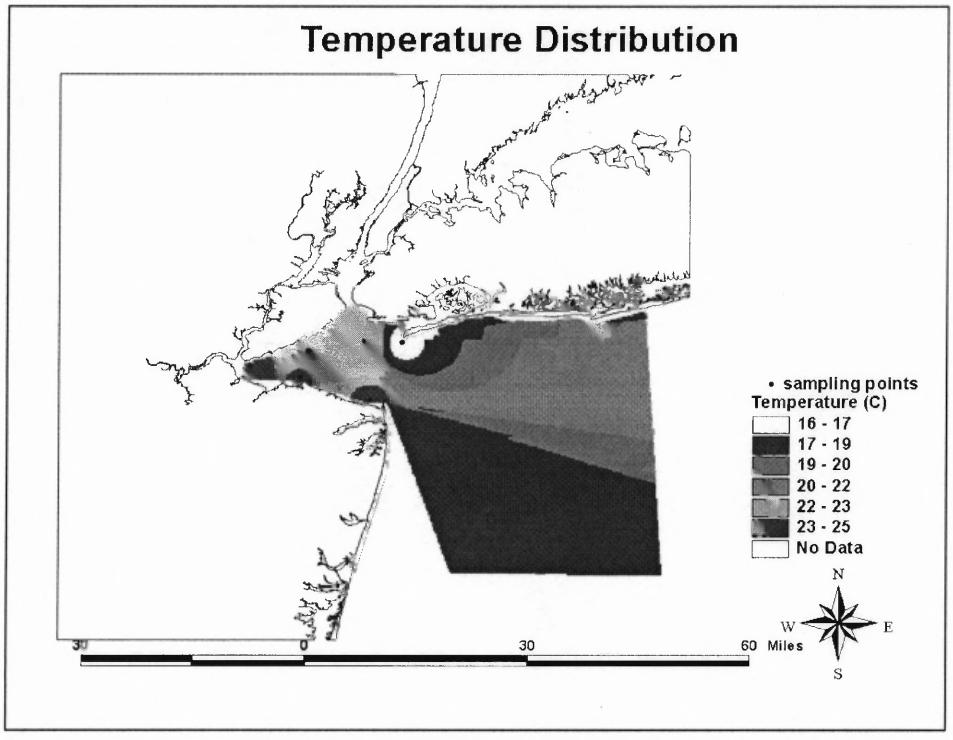

Figure 7.4 Temperature distribution map of study area

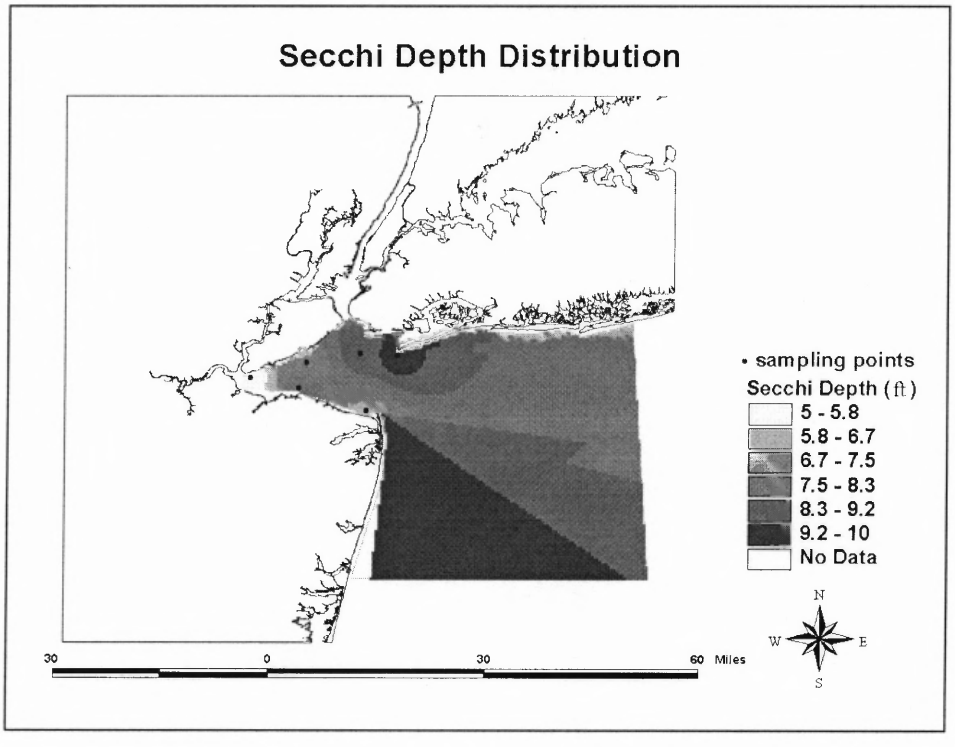

Figure 7.5 Secchi Depth distribution map of study area

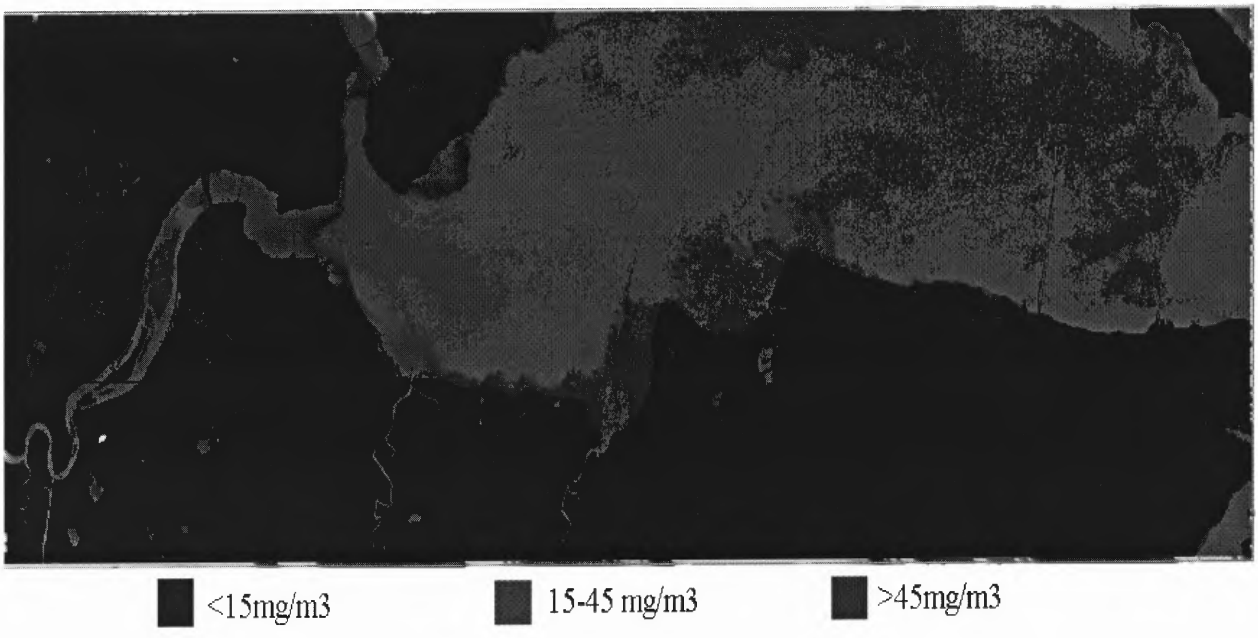

Figure 7.6 CHL_a Concentration Image of study area

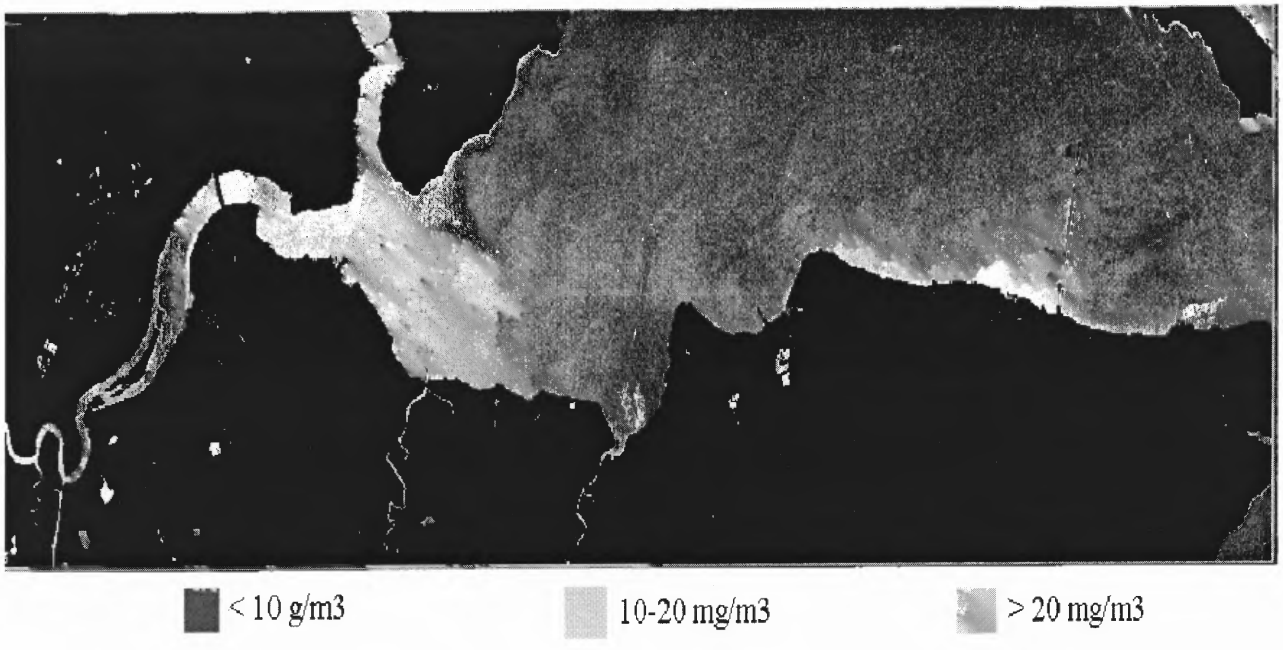

Figure 7.7 TSM Concentration Image of study area

CHAPTER 8

CONCLUSION AND FUTURE WORK

This research is aimed to provide quantitative data in support of the use of remote sensing and GIS technologies as a monitoring tool for better management of water quality conditions of Hudson/Raritan Estuary. The estuary is located south of the Verrazano Narrows and bordered by western Long Island, Staten Island and New Jersey.

There are three basic approaches to estimate optical water quality parameters from remotely sensed spectral data and based on the definitions given by Morel & Gordon (1980), can be outlined as follows: (1) an empirical method, in which statistical relationships between the upward radiance at the sea surface and the quantity of interest are taken into account; (2) a semi-empirical method, in which the spectral characteristics of the parameters of interest are known and some modeling of the physics is introduced; and (3) an analytical method, in which radiative transfer models are used to extract the inherent optical properties (IOP). In this research, an analytical method-- the modified matrix inversion models developed by Hoge et al. (1996) and Hoogenboom et al. (1998), were used as the principal models to retrieve concentrations of water quality parameters. The remotely sensed data used here consist of NASA/AVIRIS and NASA/AOL data acquired over the Hudson/Raritan Estuary in 2001 which were calibrated with in-situ measurements.

In order to apply inverse modeling to the study area which is characterized as case II water, it is necessary to calibrate an appropriate bio-optical model linking the water constituents to the inherent optical properties(IOPs) and to link the inherent optical properties to the subsurface irradiance reflectance. In this research, the Gordon's 1975

bio-optical model which was calibrated for Hudson/Raritan Estuary was used (Bagheri et al., 1999-2002). The establishment of the IOPs of the estuary and the validation of bio-optical variables are critical factors to use remote sensing as a monitoring and management tool. The modifications of different parameters used in inverse modeling are listed below:

- Adjustment of spectral slope for the a_d model---***s***
- Adjustment of total constituents backscatter spectral model exponent---***n***
- Adjustment of phytoplankton Gaussian spectral width for the a_{ph} model---***g***

Note: the model was extended to an overdetermined system and the results are shown in Table 6.1.

In addition to the inverse modeling, regression analysis was used to assess the accuracy of Matrix Inversion Method (MIM) which resulted in estimation for concentrations of water quality parameters and validation of the results based on in situ measurements.

In conclusion, the approaches used in this research are based on the capabilities of AVIRIS and LIDAR data which can potentially provide a better understanding of how sunlight interacts with estuarine/inland water, especially when complemented with in situ measurements for analysis of water quality parameters and eutrophication processes. The AVIRIS hyperspectral data provide us with an opportunity to apply such algorithms using a wide range of spectral reflectances offered by the sensor characterizing estuarine environment. The methodology described above provides a reference baseline of remote sensing and in situ measurements that will have significance for future work on underwater light field and remote sensing methodology development for the

Hudson/Raritan Estuary. Currently there is no systematic management tool for monitoring and prediction of pollution that is applicable to the Hudson/Raritan Estuary. Remote sensing can provide greater economy in such application than using conventional methods. The products of remote sensing data derived from AVIRIS/LIDAR analysis in forms of thematic maps representing the spatial/temporal distributions of water quality parameters are important input into a GIS for better management of the water resources of the study site.

Because of World Wide Web(WWW) becoming a primary means of disseminating information, utility of such a GIS system in the future will be more promising. Over the last decade GIS has grown at such a rapid rate that Web-GIS technology has appeared and GIS visualization tools for interacting with spatial data are available. Interactive mapping is growing as a mechanism for users to investigate data and perform spatial visualization analysis. This technology uses the Internet client-server scenario where the user (client) submits commands, the web server processes the commands, and the results will be passed to the client in the form of an updated map in a Web browser window (Halls J.N., 2003). In a Web-based GIS application, it would be possible for users to navigate existing spatial objects (points, lines and polygons) or other information related to spatial objects on the Web browser with ease (Park D. J., 2001). In such approach, the application of Web-GIS will facilitate the communication among different interest groups like water resources managers, environment planners and citizens.

The configuration of the Web-based GIS is depicted on Figure 8.1. The realization of this Web-based GIS as future work will be achieved with the application of

the software – ArcIMS developed by ESRI (Environmental Systems Research Institute). With ArcIMS, the dynamic maps and data via the web can be delivered, easy-to-use, task-focused applications that use geographic content can be created, and custom applications using industry-standard web-based environments can be developed, sharing data with others to accomplish tasks and implement GIS portals.

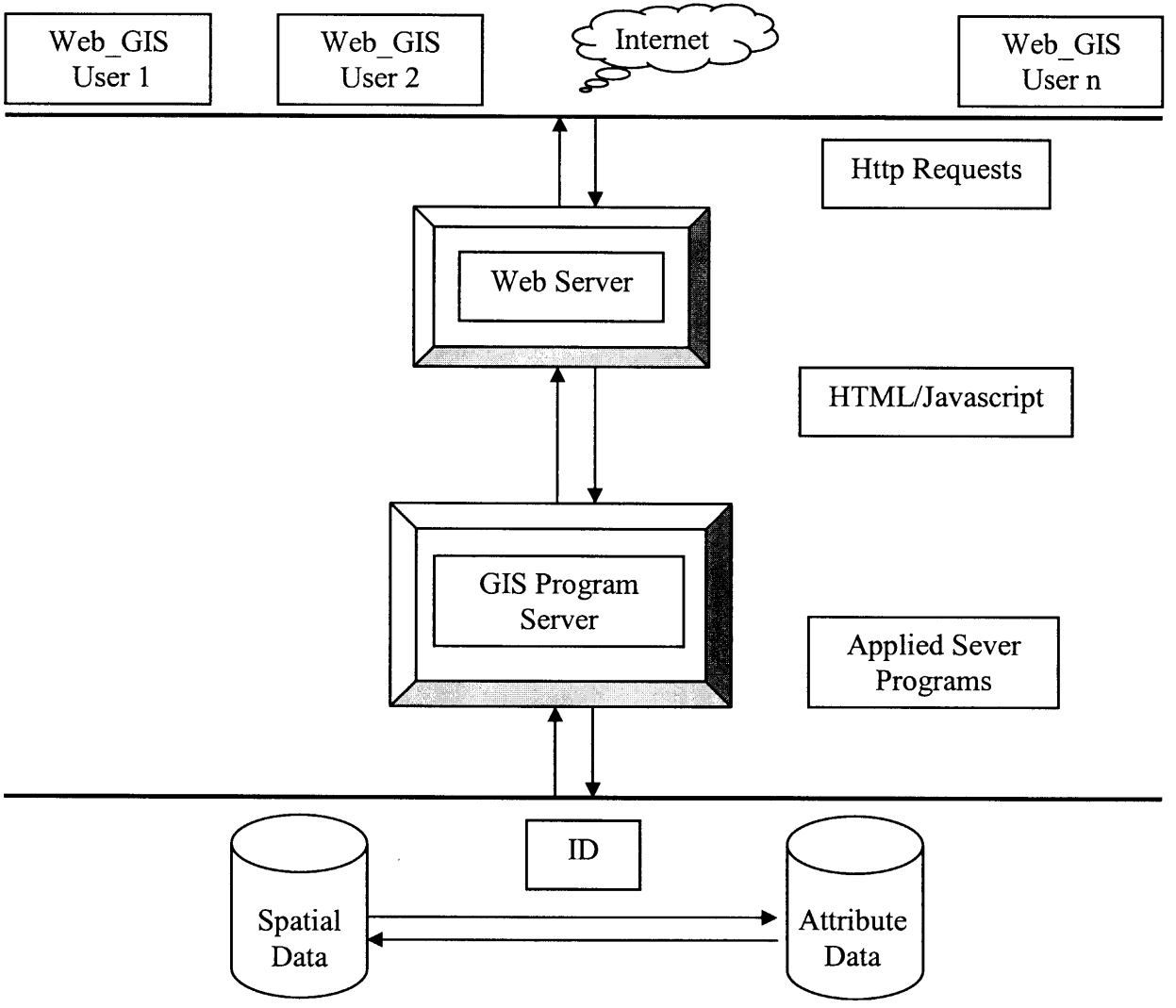

Figure 8.1 The framework of Web-based GIS

APPENDIX A

STATISTICS FORMULA USED IN THIS RESEARCH

The correlation matrix has its elements as the coefficients of simple correlation between all pairs of X variables. This matrix is defined as follows:

$$\underset{(p-1)\times(p-1)}{r_{xx}} = \begin{bmatrix} 1 & r_{12} & \cdots & r_{1,p-1} \\ r_{21} & 1 & \cdots & r_{2,p-1} \\ \vdots & \vdots & \ddots & \vdots \\ r_{p-1,1} & r_{p-1,2} & \cdots & 1 \end{bmatrix} \tag{A.1}$$

Here, r_{12} again denotes the coefficient of the simple correlation between X_1 and X_2, and so on. Note the main diagonal of 1s because the coefficient of simple correlation between a variable and itself is 1. The correlation matrix r_{xx} is symmetric, $r_{ij}=r_{ji}$.

$$r_{xy} = r_{xy} = \frac{n\sum_{i,j=1}^{n} x_i y_j - \sum_{i=1}^{n} x_i \sum_{j=1}^{n} y_j}{\sqrt{[n\sum_{i=1}^{n} x_i^{\,2} - (\sum_{i=1}^{n} x_i)^2]\cdot[n\sum_{i=1}^{n} y_i^{\,2} - (\sum_{i=1}^{n} y_i)^2]}} \tag{A.2}$$

In regression analysis, matrix algebra is widely used. To express the general linear regression model:

$$Y_i = b_0 + b_1 x_{i,1} + b_2 x_{i,2} + \cdots + b_{p-1} x_{i,p-1} + e_i \tag{A.3}$$

in matrix terms, we need to define the following matrice:

$$\underset{n\times 1}{Y} = \begin{bmatrix} Y_1 \\ Y_2 \\ \vdots \\ Y_n \end{bmatrix} \qquad \underset{n\times p}{X} = \begin{bmatrix} 1 & X_{11} & X_{12} & \cdots & X_{1,p-1} \\ 1 & X_{21} & X_{22} & \cdots & X_{2,p-1} \\ \vdots & \vdots & \vdots & & \vdots \\ 1 & X_{n1} & X_{n2} & \cdots & X_{n,p-1} \end{bmatrix} \qquad \underset{p\times 1}{b} = \begin{bmatrix} b_0 \\ b_1 \\ \vdots \\ b_{p-1} \end{bmatrix} \qquad \underset{n\times 1}{e} = \begin{bmatrix} e_1 \\ e_2 \\ \vdots \\ e_n \end{bmatrix}$$

The least squares normal equations for the general linear regression model (A.3) are $X'X \cdot b = X'Y$, therefore,

$$\underset{p\times 1}{b} = (\underset{p\times p}{X'X})^{-1}(\underset{p\times 1}{X'Y}) \tag{A.4}$$

$e = Y - X \cdot b$ and defined $H = X(X'X)^{-1}X'$, thus, $e = (I - H)Y$

Hence, some frequently used items in regressions can be defined as follows:

$SSE = e'e = Y'(I - HY)$, $SSR = e'e = Y'[(H - (\frac{1}{n})J)]Y$ and $SSTO = Y'Y - (\frac{1}{n})Y'JY$, where J is an n×n matrix of 1s.

Then, the coefficient of multiple determination, denoted by R^2, is defined as follows:

$$R^2 = \frac{SSR}{SSTO} = 1 - \frac{SSE}{SSTO} \tag{A.5}$$

$$SSE = SSTO \cdot (1 - R^2) \tag{A.6}$$

$$R_a{}^2 = 1 - \frac{\frac{SSE}{n-p}}{\frac{SSTO}{n-1}} = 1 - (\frac{n-1}{n-p})\frac{SSE}{SSTO} = 1 - \frac{MSE}{\frac{SSTO}{n-1}} \tag{A.7}$$

$$C_p = \frac{SSE_p}{MSE(X_1, \cdots, X_{p-1})} - (n - 2p) \tag{A.8}$$

In the stepwise regression routine, the F* statistic for testing whether or not the slope is zero is obtained:

$$F^* = \frac{MSR(X_K)}{MSE(X_K)} \text{ or} \tag{A.9}$$

$$F^* = \frac{MSR(X_K \mid X_i, \cdots, X_j)}{MSE(X_i, \cdots X_j, X_K)}$$

The independent variable with the largest F* value is the candidate for first addition. If this F* value exceeds a predetermined level, the independent variable is added. $X_i, \cdots, X_j$ are the independent variables which are already in the model, and X_K is the candidate variable. $MSR(X_K \mid X_i, \cdots, X_j)$ measures the additional contribution to the mean of the regression sum square when X_K is included, given that $X_i, \cdots, X_j$ are already in the model.

$$MSR(X_K \mid X_i, \cdots, X_j) = MSR(X_K, X_i, \cdots, X_j) - MSR(X_i, \cdots, X_j) \tag{A.10}$$

To study the multicollinearity, variance inflation factors (VIF) are defined as:

$$(VIF)_K = \frac{1}{1 - R_K^2}, \; K = 1,2,\cdots, p-1 \tag{A.11}$$

Where R_K^2 is the coefficient of multiple determination when X_K is regressed on the *p-2* other independent variables in the model.

The *normal quantile* of the *i*th ordered residual is computed as

$$(\Phi)^{-1}\left(\frac{i - 0.375}{n + 0.25}\right) \tag{A.12}$$

where Φ^{-1} is the inverse standard cumulative normal distribution. If the residuals are normally distributed, the points on the residual normal quantile- quantile plot should lie approximately on a straight line with the residual mean as the intercept and the residual standard deviation as the slope. In SAS output, the normal quantiles of the residuals are stored in variables named **RN_*yname*** for each response variable, where ***yname*** is the response variable name.

APPENDIX B

SOLUTIONS TO INVERSE PROBLEMS IN THIS RESEARCH

Consider a discrete linear inverse problem. We begin with a data vector, **d**, of m observations, and a vector **m** of n model parameters that we wish to determine. We assume that there are more observations than model parameters, and thus more linear equations than unknowns. As we have seen, the inverse problem can be written as a linear system of equations:

$$G \cdot m = d \tag{B.1}$$

For a full rank system with more equations than unknowns, it is frequently the case that no solution m satisfies all of the equations in (B.1) exactly. This happens because the dimension of the range of **G** is smaller than m and a noisy data vector can easily lie outside of the range of **G**. A useful approximate solution may still be found by finding a particular model m that minimizes some measure of the misfit between the actual data and $G \cdot m$. The residual is given by

$$r = d - G \cdot m \tag{B.2}$$

One commonly used measure of the misfit is the 2–norm of the residual. A model that minimizes the 2–norm of the residual is called a least–squares solution. The least–squares or 2–norm solution is of special interest both because it is very amenable to analysis and geometric intuition, and because it turns out to be statistically the most likely solution if data errors are normally distributed. The 2–norm solution for m is,

$$m_{L2} = (G^T G)^{-1} G^T \cdot d \tag{B.3}$$

It can be shown that if **G** is of full rank then $(G^TG)^{-1}$ always exists.

In addition to linear least-squares, the singular value decomposition (SVD) method can be used to solve the above system (B.1).

In SVD, G can be factored into

$$\mathbf{G} = \mathbf{USV}^T \tag{B.4}$$

Where, U is an m by m orthogonal matrix with columns that are unit basis vectors spanning the data space, R^m, V is an n by n orthogonal matrix with columns that are basis vectors spanning the model space, R^n, and S is an m by n diagonal matrix. The singular values along the diagonal of S are generally arranged in decreasing size, s1≥ s2≥ s3…≥0.

If only the first p singular values are nonzero, we can partition S as $S = \begin{bmatrix} S_p & 0 \\ 0 & 0 \end{bmatrix}$

and G can be compacted into

$$\begin{aligned} G &= USV^T \\ &= \begin{bmatrix} U_{.,1}, & U_{.,2}, & \cdots & U_{.,m} \end{bmatrix} \cdot \begin{bmatrix} S_p & 0 \\ 0 & 0 \end{bmatrix} \cdot \begin{bmatrix} V_{.,1}, & V_{.,2}, & \cdots & V_{.,n} \end{bmatrix}^T \\ &= \begin{bmatrix} U_p, & U_0 \end{bmatrix} \cdot \begin{bmatrix} S_p & 0 \\ 0 & 0 \end{bmatrix} \cdot \begin{bmatrix} V_p, & V_0 \end{bmatrix}^T \\ &= U_p S_p V_p^T \end{aligned}$$

where U_p denotes the first p columns of U, V_p denotes the first p columns of V.

Therefore, the following solution can be obtained:

$$m_+ = V_p S_p^{-1} U_p^T d \tag{B.5}$$

However, the SVD solution (B.5) can become extremely unstable when one or more of the singular values, s_i, is small. In order to make the solution more stable, the

Tikhonov regularization technique can be used. Tikhonov regularization effectively gives larger weight to larger singular values in the SVD solution and gives lower weight to small singular values.

For a general linear least–squares problem there may be infinitely many least–squares solutions. If we consider that the data contain noise, and that there is no point in fitting such noise exactly, it becomes evident that there can be many solutions which can adequately fit the data in the sense that $\|G \cdot m - d\|_2$ is small enough. Under the discrepancy principle, we consider all solutions with $\|G \cdot m - d\|_2 \leq \delta$ and select from these solutions the one that minimizes the norm of m. That can be expressed as follows:

$$\min \|G \cdot m - d\|^2_2 + \alpha \|m\|^2_2 \tag{B.6}$$

where α is the Lagrange multipliers.

Note that as $\|G \cdot m - d\|_2$ increases, the set of feasible models expands, and the minimum value of $\|m\|_2$ decreases. We can thus trace out a curve of minimum values of $\|m\|_2$ versus $\|G \cdot m - d\|_2$. When plotted on a log–log scale, the curve of optimal values of $\|m\|_2$ and $\|G \cdot m - d\|_2$ often takes on an L shape. For this reason, the curve is called an L– curve. In addition to the discrepancy principle, the criterion for picking the value of α is the L–curve criterion in which the value of α that gives the solution closest to the corner of the L–curve is selected (see Figure B.1).

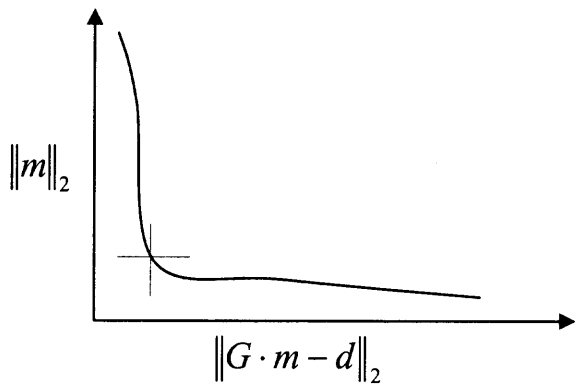

Figure B.1 Figure of L-curve for Tikhonov method.

Then, the solution of (B.6) is

$$m = \sum_{i=1}^{k} \frac{s_i^2}{s_i^2 + \alpha^2} \frac{(U_{.,i})^T \cdot d}{s_i} V_{.,i} \tag{B.7}$$

where k=min(m, n) so that all singular values are included, no matter how small they might be, an s_i is the i-th diagonal element in matrix S_p (B.5).

REFERENCES

1. Aas E. (1987). Two-stream Irradiance Model for Deep Waters. App. Opt., 26, 2095-2101.

2. Alfoldi, T. T. and Munday,J. C. (1978). Water Quality Analysis by Digital Chromaticity Mapping of LANDSAT Data, Canadian Journal of Remote Sensing, 4, 108-126.

3. Almanza, E., and Melack, J. M. (1985). Chlorophyll Differences in Mono Lake (California) Observable on LANSAT Imagery, Hydrobiology, 122, 13-17.

4. Aranuvachapun, S., and Walling, D. E. (1988). Landsat-MSS radiance as a measure of suspended sediment in the Lower Yellow River (Hwang Ho), Remote Sensing of Environment, 25, 145-165.

5. Austin, R. W., (1979). Coastal zone color scanner radiometry, Ocean OpticsVI, Proc. Sot. Photo Opt. Instrum. Eng., 208, 170-177.

6. AVIRIS, World Wide Web: http://aviris.jpl.nasa.gov/html/aviris.overview.html, 2004.

7. Bagheri, S., C. Zetlin and Opyrchal, H. (1995). Development of Library Spectra of Optical Water Quality Parameters in Nearshore Waters, 3rd Thematic Conference on Remote Sensing for Marine and Coastal Environments, VII, 25-30.

8. Bagheri, S., Zetlin, C. Smith, B. Dios, R. and Pan, Z. (1997). Optical Signature Utilization of Remote Sensing of Nearshore Waters, 4th International Conference on Remote Sensing for Marine and Coastal Environments, VII, 52-59.

9. Bagheri, S. and Zetlin, C. (1999). Remote Sensing As a Tool For Monitoring New Jersey Coastal Water Quality, Geological Association of New Jersey Annual Proceedings, 16, 99-112.

10. Bagheri S., Zetlin, C. and Dios, R. (1999). Estimation of Optical Properties of Nearshore Waters, Int'l Jour. Remote Sensing, 20, 3393-3397.

11. Bagheri S., Dekker, A. (1999). Nearshore Water Quality Assessment Using Bio-Optical Modeling and Retrieval Techniques, Proceedings of the 8th NASA/AVIRIS Geoscience Workshop, 2/8-2/12.

12. Bagheri S, Rijkeboer, M., Pasterkamp, R., and Dekker A.G. (2000). Comparison of the field spectroradiometers in preparation for optical modeling. 9th Aviris Workshop, JPL, Pasadena CA.

13. Bagheri, S., Tamnes, K and Li, W. (2001), Application of Radiative Transfer Theory to Atmospheric Correction of AVIRIS Data, 10th JPL AVIRS Workshop. Pasadena, CA.

14. Bagheri, S., Reijkober, M. and Gons, H., (2002). Inherent and Apparent Optical Measurements in the Hudson/Raritan Estuary. Aquatic Ecology 36:559-562.

15. Bagheri, S., K. Stamnes, Li, W., Yu, T. and Jiang, S. (2002). Validation of Water Quality Parameters Retrieved From Inverse Modeling. Proceedings of the 11th NASA/AVIRIS Geoscience Workshop, 3/5-3/8.

16. Baith K., Lindsay, R., Fu,G. and McClain, C. R. (2000). SeaDAS: data analysis system for ocean color satellite sensors. Eos. 82, 202.

17. Blank, L. (1980). Statistical Procedures for Engineering, Management, and Science. McGraw-Hill, Inc. New York, 649.

18. Bristow M., Nielson D., Bundy D., and Furtek R. (1981). Use of water Raman emission to correct airborne laser fluorosensor data for effects of water optical attenuation. Applied Optics, 20, 2889-2906.

19. Buiteveld, H. (1990) "A Model for Calculating Secchi Depth and Extinction" (in Dtuch), Report 90.058. Rijkswarestaat. RIZA 23.

20. Bukata R. P., Harris, G. P. and Bruton, J. E. (1974) The Detection of Suspended Solids and Chlorophyll-a Utilizing Digital MSS ERTS-1 Data", 2nd Canadian Symp. Remote Sensing, Guelph, Ontario, 552-564.

21. Bukata RP, Jerome J. H., Konratyev Kya and Pozdnyakov D.V. (1995). Optical properties and remote sensing of inland and coastal waters. CRC Press: Boca Raton.

22. Burenkov, V. I., Vasilkov, A. P., and Stephantsev, L. A. (1985). Retrieval of spectral inherent optical properties of seawater from the spectral reflectance. Oceanology, 25, 49-54.

23. Carder, K.L., Hawes, S. K., Baker, K. A., Smith, R. C., Steward, R. G. and Mitchell, B. G. (1991). Reflectance model for quantifying chlorophyll *a* in the presence of productivity degradation products. J. Geophys. Res., 96, 20, 559-20, 611

24. Carder, K. L., Reinersman, P. and Chen, R. F. (1993). AVIRIS Data Application in Coastal Oceanic Environments, Remote Sensing Environ., 44, 205-216.

25. Carder, K. L., Chen, F. R., Lee, Z., Hawes, K. and Cannizzaro, J. P. (2003). 'Case 2 chlorophyll a, MODIS Algorithm Theoretical Basis Doc. 19 (College of Marine Science, University of South Florida, St. Petersburg, Fl., 2003).

26. Chekalyuk, A. M., Hoge, F. E., Wright, C. W. , Swift, R. N. and Youngel, J. K. (2000). Airborne test of laser pump-and-probe technique for assessment of phytoplankton photochemical characteristics. Photosynthesis Research, 66, 45-56.

27. Clark D. K., (1981). Phytoplankton Algorithms for the Nimbus-7 CZCS, In: J. F. R. Gower (Editor), Oceanography from Space, Plenum Press, New York, 227-228.

28. Clark, D. K., (1999). Bio-optical algorithms, Case 1 waters. MODIS Algorithm Theoretical Basis Doc. 18 (National Oceanic and Atmospheric Administration, National Environmental Satellite Service, Washington, D.C., 1999).

29. Dekker, A. G. (1993) Detection of optical water quality parameters for eutrophic waters by high resolution remote sensing. PhD Thesis, Vrije Universiteit, Amsterdam, 222.ISBN: 90-9006-234-3.

30. Dekker, A. G., and Hoogenboom, H. J. (1996). Predictive Modeling of AVIRIS Performance over Inland Waters, JPL Airborne Earth Science Workshop Proceedings. Edited by R. O. Green, Pasadena, California, Mar. 4-8.

31. Dekker, A. G. and Donze, M. (1994) Imaging spectrometry as a research tool for inland water resources analysis. Edited by J. Hill, Dordrecht, The Netherlands: Kluwer AP.

32. Dekker, A. G., Hoogenboom, H. J., Volten, H. R., Schreurs, J. F., De Haan, and Hovenier, J. W. (1997). Angular Scattering Functions of Algae and Silt: an Analysis of Backscattering to Scatter Fraction. SPIE Conference Ocean Optics XIII. Halifax, Nova Scotia, Canada:, Oct. 22-25 .

33. Dekker, A. G., Hoogenboom, H. J. (1996). Operational Tools for Remote Sensing of Water Quality: A Prototype Toolkit. BCRS, Delft, The Netherlands, 66, BCRS report. 96-18.

34. Dekker. A.G., Peters, S.W., Vos, R., and Rijkeboer, M., (2001). Remote Sensing for Inland Water Quality Detection and Monitoring: State-of-the art Application in Friesland Water in A. Van Dijk and M.G. Bos (eds.). GIS and Remote Sensing Techniques in Land and Water-management, Kluwer Academic Publishers, The Netherlands. 17-38.

35. Dirks, R. W. J., and Spitzer, D. (1987). On the Radiative Transfer in the Sea, including Fluorescence and Stratification Effects. Limnol. Oceanogr., 32, 942-953.

36. Doerffer, R. (1989). Imaging Spectroscopy for Detection of Chlorophyll and Suspended Matter. Imaging Spectroscopy: Fundamentals and Prospective Applications. Dordrecht. Kluwer Academic Publishers. 215-258.

37. Doerffer, R., and Fisher, J. (1994). Concentrations of chlorophyll, suspended matter, and gelbstoff in case II waters derived from satellite coastal zone color scanner data with inverse modelling methods. J. Geophys. Res., 99, 7,457-7,4660.

38. ENVI User Manual, Research Systems, Inc. Boulder, CO 80301, 2002.

39. European Association of Remote Sensing Laboratories (EARSEL), "10th EARSEL Symposium in Toulouse, France", (1991). 150.

40. Exton, R. J., Houghton, W.M., Esaias W., Harriss, R. C., Farmer, F. H. and White, H. H. (1983). Laboratory Analysis of Techniques for Remote Sensing of Estuarine Parameters Using Laser Excitation. Appl. Opt., 22, 54.

41. Garver, S. A. and Siegel, D. A., (1997). Inherent optical property inversion of ocean color spectra and its biogeochemical interpretation: 1. Time series from the Sargasso Sea. J. Geophys. Res., Vol. 102, 18,607-18,625.

42. Gastil, M., and Melack, J., (1998). Improved Atmospheric Correction for AVIRIS Spectra from the Inland Waters, Proceedings of the 7th NASA/AVIRIS Geoscience Workshop, 1/12-1/16.

43. Gitelson, A., Garbuzov, G. P., Szilagyi, F., Mittenzwey, K. H., Karnjeli, A., and Kaiser, A., (1993). Quantitative Remote Sensing Methods for Real-Time Monitoring of Inland Waters Quality. Int. J. Remote Sensing. Vol. 14, No. 7. 1269-1295.

44. Gohin, F., Druon, J. N. and Lampert, L., (2002). A five-channel chlorophyll concentration algorithm to SeaWiFS in coastal waters. International Journal of Remote Sensing, Vol.23 no. 8, pp.1639-1661.

45. Gons, H. J., (1999), Optical teledetection of chlorophyll a in turbid inland waters. Env. Sci. Tech, Vol. 33, No.7, p.1127-1132.

46. Gons, H. J., Burger-Wiersma, T., Otten, J. H. and Rijkeboer, M., (1992). Coupling of Phytoplankton and Detritus in a Shallow Eutrophic Lake (Lake Loosdrecht, The Netherlands), hydrobiologia, Vol.233, pp51-59.

47. Gons, H. J., (1999). M. Reijkober., and Bagheri, S., "Teledetection of Chlorophyll-a in Estuarine and Coastal Waters.Envirn.Sci. & Technology. Vol. 34, No 24,5189-5192.

48. Gordon H. R., Brown, O. B. and Jacobs, M. M., (1975). Computed relationships between Inherent and apparent optical properties of a flat homogeneous ocean. Appl. Optics, 14: 417—427

49. Gordon, H. R., (1979). Diffuse Reflectance of the Ocean: The theory of its augmentation by chlorophyll_a fluorescence at 685nm. Appl. Opt. Vol. 18, pp. 1161-1166.

50. Gordon, H. R., Clark, D. K., Mueller, J. L. and Havis, W. A., (1980). Phytoplankton Pigments from the Nimbus-7 Coastal Zone Color Scanner: Comparisons With Surface Measurements, Science, 210, 63-66.

51. Gordon, H. R. and Morel, A., (1983). Remote assessment of ocean color for interpretation of satellite visible imagery, A Review, in lecture notes on coastal and estuarine studies. Springer Verlag, New York. pp144.

52. Gordon, H. R., Brown, O. B., Evans, R. H., Brown, J. W., Smith, R. C., Baker, K. S., and Clark, D. K., (1988). A semianalytic radiance model of ocean color, J. Geophys. Res., 93, 10,909-10,924.

53. Gower, J. F. R., and Borstad, G. A., (1981). Use of the in-vivo Fluoresecence Line at 685 nm for Remote Sensing Surveys of Surface Chlorophyll-a, In Oceanography from Space, edited by J.F.R. Gower (NY: Plenum), 329-338, 1981.

54. Gower, J. F. R., (1994). Red tide monitoring using AVHRR/HRPT imagery from a local receiver. Remote Sensing Environment, Vol. 48, 309-318.

55. Gower, J. F., Doerffer, R. R. and Borstad, G. A., (1999). "Interpretation of the 685 peak in water-leaving radiance spectra in terms of fluorescence, absorption and scattering, and its observation by MERIS", Int. J. Remote Sensing **20**: 1771-1786.

56. Green, R. O. and Conel, J. E., (1995). Movement of Water Vapor in the Atmosphere Measured by an Imaging Spectrometer at Rogers Dry Lake", CA., Proc. Fifth Annual Airborne Earth Science Workshop, JPL Public 95-1.

57. Green, R. O., and Gao, Bo-Cai, (1993). A Proposed Update to the Solar Irradiance Spectrum Used in LOWTRAN and MODTRAN, Proc. Fourth Annual Airborne GeoScience Workshop, JPL Public 93-26.

58. Green, R. O., (1991). Retrieval of Reflectance From AVIRIS-Measured Radiance Using a Radiative Transfer Code, Proc. Third AVIRIS Workshop, JPL Publication 91-28, pp. 200-210.

59. Green, R. O., (1996). Summaries of the 6th Annual JPL Airborne Earth Science Workshop. Vol. 1, JPL AVIRIS Workshop. Pasadena, CA.

60. Green, R. O., Carrere, V., Conel, J., (1989). Measurement of Atmospheric Water Vapor Using the Airborne Visible/Infrared Imaging Spectrometer, Image Processing 1989, Sparks, Nevada, 23 May, ASPRS, pp. 31-44.

61. Gross, L., Frouin, R., Dupouy, C. C., Andre, J. M., and Thiria, S., (2004). Reducing variability that is due to secondary pigments in the retrieval of chlorophyll *a* concentration from marine reflectance: a case study in the western equatorial Pacific Ocean. Applied Optics, Vol. 43, no. 20, pp. 4041-4054.

62. Habbane, M., Dubois, J. M., El-Sabh, M. I., Larouche, P., (1998). Empirical algorithm using SeaWiFS hyperspectral bands: a simple test. International Journal of Remote Sensing, Vol. 19, no. 11, pp. 2161-2169.

63. Hakvoort, J. H. M., H. De Haan, R. W. L., Jordans, R. J., Vos, Peters,S. W. M. and Rijkeboer, (2000). Towards airborne remote sensing of water quality in the Netherlands: validation and error analysis. Second EARSEL Workshop on Imaging Spectroscopy.

64. Hamilton, M. K., Davis, C. O., Rhea, W. J., Pilorz, S. H. and Carder, K. L., (1993). Estimating Chlorophyll Content and Bathymetry of Lake Tahoe Using AVIRIS Data, Remote Sens. Environ. V. 44 pp.217-230.

65. Hires, R. and Mellor, G. (1987). Numerical Model Studies of Circulation in the Hudson/Raritan Estuary. In: Hudson/Raritan Issues, Resources, Status and Management. NOAA Estaury-of-the-month seminar series No. 9. pp. 27-43.

66. Hoge F. E. and Swift R. N., (1981). Airborne simultaneous spectroscopic detection of laser-induced water Raman backscatter and fluorescence from chlorophyll_a and other naturally occurring pigments. Applied Optics, Vol. 20. pp.3197-3205.

67. Hoge F. E. and Swift R. N., (1981). Application of the NASA Airborne Oceanographic LIDAR to the mapping of chlorophyll and other organic pigments in Chesapeake Bay Plume Study Superflux 1980, NASA Conference Publication 2218 (U.S. GPO, Washington, D. C.) pp. 349.

68. Hoge F. E. and Swift R. N., (1983). Airborne Dual Laser Excitation and Mapping of Phytoplankton Photopigments in a Gulf Stream Warm Core Ring.. Applied Optics, Vol. 22. pp2272.

69. Hoge, F. E., Berry, E. R. and Swift, R. N., (1986). Active-Passive airborne ocean color measurement. 1:Instrumentation. Appl. Opt. Vol.25, no.1, pp39-47.

70. Hoge, F. E., Swift, R. N. and Yungle,J. K., (1986). Active-Passive, Airborne Ocean Color Measurement. 2:Applications. Appl.Opt. Vol. 25, no. 1, pp.48-57.

71. Hoge, F. E. and Lyon ,P. E., (1996). Satellite retrieval of inherent optical properties by linear matrix inversion of oceanic radiance models: An analysis of model and radiance measurement errors, J. Geophys. Res. 101, 16,631-16,648.

72. Hoge, F. E., Wright, C. W., Lyon, P. E., Swift, R. N. and Yungel, J. K., (2001). Inherent optical properties imagery of the western North Atlantic Ocean: Horizontal spatial variability of the upper mixed layer, J._Geophys. Res. 106, 31129-31140.

73. Hoge, F. E. and Lyon, P. E., (1999). Spectral Parameters of Inherent Optical Property Models: Method for Satellite Retrieval by Matrix Inversion of an Oceanic Radiance Model, Appl. Opt. 38, 1657-1662.

74. Hollinger, A. B., Gray, L. H., Gower, J. F. R., Edel, H., (1987): The Fluorescence Line Imager: An Imaging Spectrometer for Land and Ocean Remote Sensing. Proc. SPIE 834.

75. Hoogenboom, H. J., Dekker, A. G. and Haan, J. F., (1998). Retrieval of Chlorophyll and Suspended Matter from Imaging Spectrometry Data by Matrix Inversion. Canadian Journal of Remote Sensing, Vol. 24, No. 2. June, 1998. 144-152

76. IOCCG, (1999). Status and Plans for Satellite Ocean Color Missions: Considerations for Complementary Missions. Report Number 2. Dartmouth, Canada. 42p.

77. Jeffries H. P., (1962). Environmental Characteristics of Raritan Bay, Limnol. Oceanogr., 7, 21-31.

78. Jensen, J. R., B. Kjerfve, E. W. Ramsey, K. E. Magill, C. Medeiros, and J. Sneed, (1989). Remote Sensing and numerical modeling of suspended sediment in Laguna de Terminos, Campeche, Mexico. Remote Sensing of Environment, Vol. 28, pp. 33-44.

79. Jiang, S., 2003 Radiative transfer in the coupled atmosphere-sea ice-ocean system with application in remote sensing, Ph. D. Thesis, Stevens Institute of Technology.

80. Kahru, M. and Mitchell, B. G., (1999). Empirical chlorophyll algorithm and preliminary SeaWiFS validation for the California Current. International Journal of Remote Sensing, Vol. 20, no. 17, pp. 3423-3429.

81. Kattawar, G. W., and Vastano, J. C., (1982). Exact 1_D Solution to the Problem of Chlorophyll Fluorescence from the Ocean. Appl. Opt. Vol. 21, pp. 2489-2492.

82. Keiner L. E. and Brown, C. W., (1999). Estimating oceanic chlorophyll concentrations with neural networks. International Journal of Remote Sensing, Vol. 20, no. 1, pp.189-194.

83. Khorram, S. and Cheshire, H. M., (1983). Use of LANDSAT MSS (Multispectral Scanner) digital data in water quality mapping of the Neuse River estuary, NC. North Carolina State University/Water Resource Res. Inst.; Raleigh, NC. pp. 41.

84. Khorram, S., Catts, G. P., Cloern, J. E. and Knight, A. W. (1986). Modeling of Estuarine Chlorophyll-a from an Airborne Scanner, Proc. of IGARSS'86 Symp. pp. 1387-1396.

85. Kirk, J. T. O., (1984), Dependence of relationship between inherent and apparent optical properties of water on solar altitude. Limnol. Oceanogr. 29: 350—356

86. Kirk, J. T. O., (1991). Volume scattering function, average cosines, and the underwater light field. Limnol. Oceangr. 36(3): 455—467

87. Kirk, J. T. O., (1994). Light and photosynthesis in aquatic ecosystems. University Press, Cambridge, UK. 401

88. Kirk, J. T. O., (1975, 1976a). A Theoretical Analysis of the Contribution of Algal Cells to the attenuation of Light Within Natural Waters. 1. General Treatment of Suspensions of Living Cells. 2. Spherical Cells; New Phytol., 75: pp. 11-20; 21-36. 3. Cylliondrical and Spheroidal Cells. New Phytol., 77: pp. 341-358.

89. Kirk, J. T. O., (1976b). Yellow Substance (Gelbstoff) and its Contribution to the Attenuation of Photosynthetically Active Radiation in Some Inland and Coastal South-eastern Australian Waters. Aust. J. Mar. Freshwater Res. 27: 61-71.

90. Kirk, J. T. O., (1980). Spectral Absorption Properties of Natural Waters: Contribution of the Soluble and Particulate Fractions to Light Absorption in some Inland Waters of South Eastern Australia, Aust. J. Mar. Freshwater Res., 31:p 287-296.

91. Kirk, J. T. O., (1981a). Monte Carlo Study of the Nature of the Underwater Light Field in, and the Relationships Between Optical Properties of, Turbid Yellow Waters, Aust. J. Mar. Fresh water Res., 32:p 517-532.

92. Kirk, J. T. O., (1981b). Estimation of the Scattering Coefficient of Natural Waters Using Underwater Irradiance Measurements, Aust. J. Mar. Freshwater Res., 32:p533-539.

93. Kirk, J. T. O. (1993). Characteristics of the Light Field in Highly Turbid Waters: a Monte Carlo study. Limnol. Oceanogr., V. 29, pp. 350-356.

94. Kishino, M., Sugihara, S., and . Okami, N., (1984a). Influence of Fluorescence of Chlorophyll_a on Underwater upward Irradiance Spectrum. La Mer, Vol. 22, pp. 224-232.

95. Kishino, M., Sugihara, S., and . Okami, N., (1984b). Estimation of Quantum Yield of Chlorophyll_a Fluorescence from the upward Irradiance Spectrum in the Sea. La Mer, Vol. 22, pp. 233-240.

96. Kozasa, E., (1984). Distribution of Chlorophyll in the East China Sea Characteristics Measured with A Satellite LANDSAT 3 in May 1982, Bull. Seikai Reg. Fish. Res. Lab./Seisuiken Kenpo.; no. 61, pp. 223-233.

97. Krijgsman, J., (1994). Optical Remote Sensing of Surface Water, Ph. D. Thesis, Delf University Press, The Netherlands, 19-8 p.

98. Lee, Z. P., Carder, K. L., Hawes, S. K., . Steward, R. G., Peacock, T.G., and Davis, C. O., (1994). Model for the interpretation of hyperspectral remote-sensing reflectance, Appl. Opt., 33, 5721-5732.

99. Liew, S.C., Chia, A.S. and Kwoh, L.K., (2001). Evaluating The Validity of SeaWIFS Chlorophyll Algorithm for Coastal Waters, 22nd Asian Conference on Remote Sensing, 5-9 Novermer, 2001, Singapore.

100. Lyon, J. G., Bedford, K. W., Chieh-Cheng, J., Yen, D. H. and Mark, D. J., (1988). Determinations of suspended sediment concentration from Multiple day Landsat and AVIRIS data, Remote Sensing of Environment, Vol. 25, pp. 107-115.

101. MacKenzie, C. L. Jr., (1990). History of the Fisheries of Raritan Bay, New York and New Jersey. Mar. Fish. Rev. 52(4): 1-45.

102. Maffione, R. A., Dana, D. R. and Voss, J. M., (1995). Spectral dependence of optical backscattering in the ocean, paper presented at the Optical Society of America Annual Meeting, Opt. Soc. Of Am., Portland, Oreg., Sept. 10-15.

103. Mitchell, R., Yungel, J. and Hoge, F., (1999). Airborne Oceanographic Lidar. World Wide Web: Lidar, http://aol.wff.nasa.gov.

104. Morel, A. and Prieur, L., (1977). Analysis of variations in ocean color. Limnol. Oceanogr. Vol. 22, pp. 709-722

105. Morel, A., and Gordon, H. R., (1980). Report of the working group on ocean color, Boundary Layer Meteorol., 18, pp 343-355.

106. Munday, J. C., and Zubkoff, P. L., (1981). Remote Sensing of Dinoflagellate Blooms in a Turbid Estuary, Photogram. Engr. and Remote Sensing, Vol. 47, pp. 523-532.

107. NEN 6520, (1981). Water: Spectrophotometric determination of chlorophyll a content, Nederlands Normalisatie instituut, Delft, The Netherlands (in Dutch).

108. NEN 6484, (1982). Water: Determination of the content of not dissolved material and its ignition residue. Nederlands Normalisatie instituut, Delft, The Netherlands (in Dutch)

109. Neville, R. A., and Gower, J. F. R., (1977). Passive Remote Sensing of Phytoplankton via Chlorophyll_a Fluorescence. J. Geophys. Res. Vol. 82, pp. 3487-3493.

110. Ocean Optics, Inc., User's Manual, (1994). Dunedin, Florida.

111. O'Connor, D. J.. and Muller, J., (1984). A Water Quality Analysis of New York Harbor Complex, J. Environ. Eng., Vol. 110, pp 1027-1047.

112. Oey, L. Y., Mellor, G. L. and Hires, R. I., (1985). A three-dimensional simulation of the Hudson/Raritan Estuary. Part I and II. Journal of Geophysical Oceanography, 15(12): 1676--1720.

113. Optronic Laboratories Inc., User's Manual, (1995). Orlando, Florida.

114. O'Reilly, J. E., Maritorena, S., Michell, B. G., Siegel, D. A., Carder, K. L., Garver, S. A., Kahru, M. and McClain, C., (1998). Ocean color chlorophyll algorithms for SeaWiFS. Journal of Geophysical Research, Vol. 103, 24,937-24,953

115. O'Reilly, J. E., (2000). Ocean Color Chlorophyll a Algorithms for SeaWiFS, OC2, and OC4: Version 4. In Stanford B.Hooker and E.R. Firestone, Ed., SeaWiFS Post-launch Technical Report Series. NASA Tech. Memo. 206892, Vol. 11.

116. Pasterkamp, R., Peters, S. W. M., Rijkeboer, M., and Dekker, A. G., (1999). RESTWES: Retrieval of Total Suspended Matter Concentrations from SPOT Images, W-99/33, IVM/VU, Amsterdam, The Netherlands, 45p.

117. Pearce, J., (1984). Concluding Remarks. In: Raritan Bay Its Multiple Uses and Abuses. Proceeding of the Walford Memorial Convocation. A. Pacheco, editor. Sandy Hook Laboratory Technical Series Report No. 30, pp 91-94.

118. Pearce, J., (1988). Changing patterns of Biological Responses to Pollution in the New York Bight In: Hudson/Raritan Estuary Issues, Resources, Status and Management. NOAA Estuary-of-the-month seminar, No. 9. pp. 1-26.

119. Peters, S. W. M., (2001). Analytical inversion methods for water quality parameter determination from remotely observed spectra. Institute for Environmental Studies, Vrije Universiteit, Netherlands.

120. Petzold, T. L., (1972). Volume Scattering Functions for Selected Ocean Waters, University of California, San Diego, Scripps Ist. Oceanogr. Visibility Lab., Ref. 72-78.

121. Poole, L. R. and Esaias, W. E., (1982). Water Raman Normalization of Airborne Laser Fluorosensor Measurements: a Computer Model Study. Appl. Opt. Vol. 21. pp. 3756.

122. Preisendorfer, R. W., (1976). Hydrologic Optics: Vol. I-IV, U. S. Department of Commerce.

123. Preisendorfer, R. W. and Mobley, C. D., (1988). Theory of Fluorescence Irradiance Fields in Natural Waters. J. Geophys. Res., Vol. 93, pp. 10,831-10,855.

124. Rijkeboer, M, Dekker, A. G. and Hoogenboom, H. J., (1998). Reflectance spectra with associated water quality parameters measured in Dutch waters (Speclib-TK-database). Institute for Environmental Studies, E98/12, The Netherlands.

125. Ritchie, J. C., Copper, C. M. and Schiebe, F. R., (1990). The relationship of MSS and TM data with suspended sediments, chlorophyll, and temperature in Moon Lake, Mississippi, Remote Sensing of Environment, Vol. 33, pp. 137-148.

126. Roesler, C. S., and Perry, M. J., (1995). In situ phytoplankton absorption, fluorescence emission, and particulate backscattering spectra determined from reflectance. Journal of Geophysical Research, Vol. 102, 13,279-13,294.

127. Schiebe, F. R., Harrington, J. A. and Ritchie, J. C., (1992). Remote Sensing of suspended sediments: the Lake Chicot, Arkansas project. International Journal of Remote Sensing, Vol. 13, pp. 1478-1509.

128. Stavn, R. H., Weidemann, A. D, (1989). Shape Factors, Two-flow Models, and the Problem of Irradiance Inversion in Estimating Optical Parameters. Limnol. Oceanogr. Vol. 34. No. 8, 1426-1441.

129. Stumpf, R. P. and J. R. Pennock, (1989). Calibration of a general optical equation for remote sensing of suspended sediments in a moderately turbid estuary. Journal, Geophysical Research – Oceans, Vol. 94, 14363-14371.

130. Stumpf, R. P. and Pennock, J. R., (1991). Remote estimation of the diffuse attenuation coefficient in a moderately turbid estuary. Remote Sensing of Environment, Vol. 38, 183-191.

131. Stumpf, R. P., Gelfenbaum, G. and Pennock, J. R., (1993). Wind and tidal forcing of a buoyant plume, Mobile Bay, Albama. Continental Shelf Research, Vol. 13, 1281-1301.

132. Sugihara, S., Kishino, M. and Okami, N., (1985). Estimation of water quality parameters from irradiance reflectance using optical models. J. Oceanog. Soc. Japan, Vol. 41, 399-406.

133. Topliss, B. J., (1985). Optical Measurements in the Sargasso Sea: Solar Stimulated Chlorophyll Fluorescence. Oceanol. Acta., Vol. 8, pp. 263-270.

134. Topliss, B. J and Plattt, T., (1986). Passive Fluorescence and Photosynthesis in the Ocean: Implications for Remote Sensing, Deep Sea Res. I, 33:849-864.

135. Van der Woerd, H., Hakvoort, J. H. M., Hoogenboom, H. J., Omtzigt, N., Pasterkamp, R., Peters, S. W. M., Ruddick, K. G., De Valk, C., and Vos, R. J., (2000). Towards an Operational Monitoring System for Turbid Waters. O-00/16, IVM/VU, Amsterdam, 62p.

136. Vasilkov, A. P. (1997). A retrieval of coastal water constituent concentrations by least-square inversion of a radiance model. Proceedings of the 4th International Conference on Remote Sensing for Marine and Coastal Environments, Orlando, Florida, 17-19 March 1997, Vol. II, 107-116.

137. Vos, R. J., Dekker, A. G., Peters, S. W. M., Rossum, G. V. and Hooijkaas, L. C., (1998). RESTWAQ2, part II. Comparison of remote sensing data , model results and in-situ data for the Southern Frisian Lakes. Rep.num. NRSP-2 98-08b, Netherlands Remote sensing Board (BCRS); Programme Bureau; Rijkswaterstaat Survey Department.

138. Walker, N. D., Fargion, G. S., Rouse, L. J. and Biggs, D. C., (1994). The great flood of summer 1993: Mississippi river discharge studied. Eos, Trans. American Geophys. Union, Vol. 75, 409,414-409,415.

139. Walker, N. D., (1996). Satellite assessment of Mississippi River plume variability: causes and predictability. Remote Sensing of Environment, Vol. 58, 21-35.

140. Weidemann, A. D., Stavn, R. H., Zanefeld, J. R., and Wilcox, M. R. (1995). Error in predicting hydrosol backscattering from remotely sensed reflectance, J. Geophys. Res,, Vol. 100, 13,163-13,177.

141. Whitlock, C. H., Poole, L. R., Usry, J. W., Houghton, W. M., and Witte, W. G., (1981). Comparison of reflectance with backscatter and absorption parameters for turbid waters. Appl. Optics

142. Wright, W. C., Hoge, F. E., Swift ,R. N., Yungel, J. K. and Schirtzinger, C. R., (2001). Next-generation NASA airborne oceanographic lidar system, Applied Optics, Vol. 40, no. 3, pp. 336-342.